Seismic data analysis of an onshore-offshore transition zone at Ramså Basin, Norway – a modelling study

Master Thesis in Earth Science

Kingsley Chibuzo Ofoedu

Department of Earth Science

University of Bergen

October 2022

Abstract

Onshore-offshore transition zones (TZ) are the most challenging environments to acquire seismic data. Such areas may encompass land and shallow sea up to about one hundred meters in depth which is too shallow for conventional seismic acquisition method using towed streamers. Due to the complex nature of the environment associated with numerous obstacles, data acquisition often requires workarounds at the expense of data quality, which translates into datasets that may be difficult to process. Some TZ areas have been explored by means of seismic methods for whole crustal studies and many other reasons. The Ramså Basin in northern Norway is one of such areas where TZ-seismic data were acquired in addition to other geophysical datasets for geological and geotechnical investigations. However, the data were difficult to understand and process using conventional methods, necessitating the use of seismic modelling for better understanding of the data in this present study. To perform seismic modelling, interpreted seismic horizons from adjacent onshore and offshore segments of the area are used to constrain the subsurface structure. Elastic properties populated in the initial set of models are based on available well and seismic data, and the final model is based on a P-wave velocity derived via traveltime tomography, including densities from well data. Synthetic datasets derived by finite-difference modelling are used to validate the models, and ray tracing modelling is used to generate various wave modes for analysing the TZ-seismic data.

The simulated traveltime curves demonstrate that constructive and destructive interference occurred as a result of tuning effect, and interaction of many wave types overlapping each other. Consequently, the shape of the wavelets and amplitudes in the TZ-seismic data are distorted. Additionally, strong seabed multiples are identified which inhibit the detectability of comparatively low energy primary reflections. Results from seismic acquisition experiments designed to investigate potential survey geometries for optimum imaging of the target (top Basement) along the TZ indicate that reflection coverage may be improved with receivers placed as close as possible to the TZ, including the continental slope. By placing the receivers that way, only few near-offset shots from the sea may be required to image the target along the TZ. Furthermore, the receivers on the continental slope (ocean bottom seismometers) will allow for mode-converted S-waves to be recorded in addition to P-waves.

Acknowledgements

This thesis is written in partial fulfilment of the requirements for a Master of Science degree in Earth Science at the Department of Earth Science, University of Bergen. I would like to express my gratitude to everyone who contributed in one way or another to make this thesis possible. First of all, I owe a debt of gratitude to my main supervisor, Prof. Isabelle Lecomte for invaluable guidance, constructive feedbacks and encouragement. I would like to thank my first co-supervisor, Prof. Tor Arne Johansen for invaluable feedbacks and discussions. Special thanks to my second co-supervisor, Dr. Bent Ole Ruud for introducing me to finite-difference and traveltime tomography software, for patiently answering my numerous questions, and for invaluable feedbacks and discussions. I would also like to thank the Geological Survey of Norway (NGU) and, more specifically, Marco Brönner for providing interpreted horizons used in this thesis, and for invaluable feedbacks and contributions.

I would like to thank NORSAR Innovation AS (2-D Ray Modelling), Petroleum Geo-Services (Nucleus+) and Schlumberger (Petrel) for granting academic licences of their respective softwares. I also wish to thank Prof. Jun Korenaga at Yale University for the free and open-source software used for traveltime tomography (tomo2D). Thanks also to the Center for Wave Phenomena (Colorado School of Mines) and the current principal investigator of the seismic unix project (John Stockwell) for the open-source seismic utility package (SU). The mapping authority (Kartverket) is thanked for the depth elevation model and depth bathymetry model used to constrain the subsurface model in this study.

A big thanks to Øyvind Natvik at the IT department for setting up occasional remote access to my workstation, and for resolving several software related issues. I would also like to thank the management and staff at the department of Earth science for well-thought-out strategies followed during the Covid-19 pandemic, and for ensuring access to workstations on-campus and remotely when necessary.

Finally, I would like to thank my family for their supportive role during the past two years.

Contents

List of figures

List of tables

Nomenclature

BCU – Base Cretaceous Unconformity

CRG – Common Receiver Gathers

CSG – Common Shot Gathers

DBM – Digital Bathymetric Model

DEM – Digital Elevation Model

FD – Finite Difference

GL – Ground Level

MSL – Mean Sea Level

NAZ – Narrow Azimuth

NCS – Norwegian Continental Shelf

NMO – Normal Moveout

NSS – Norsar Software Suite

OBC – Ocean Bottom Cable

OBN – Ocean Bottom Node

OBS – Ocean Bottom Seismometer

PML – Perfectly Matched Layer

PRM – Paraxial Ray Method

PSDM – Pre-Stack Depth Migration

RMS – Root Mean Square

RT – Ray Tracing

TWT – Two-Way Traveltime

TZ – Transition Zone

VSP – Vertical Seismic Profile

WAZ – Wide Azimuth

Chapter 1: Introduction

1.1 Overview and rationale

In many areas around the world where seismic data have been acquired for either oil exploration or other subsurface studies, onshore – offshore transition zone (TZ) seismic data (Stucchi et al., 2003; Aouad et al., 2012; Wyman and Ahmad, 2013; Liu et al., 2015; Roberts and FitzPatrick, 2015, Ruiz et al., 2017) are often the missing link between the vast amount of onshore and offshore seismic data records. To date, only a few studies are published about TZ-seismic on the Norwegian Continental Shelf (NCS) (e.g., Mjelde et al., 1993; Abdelmalak et al., 2015; Brönner et al., 2017; Shulgin et al., 2018; Raum et al., 2002). The lack of interest in TZ-seismic is due to the challenging nature of the environment which ranges from shallow water near the coast to the coastline and further onto wet unconsolidated land. The environmental setting varies from place to place but they are generally dynamic and complex in nature. The area can include land, fresh and saltwater marsh, and swamp, near shoreline, surf and tidal zones, lagoons, shallow offshore coral reefs, and deeper waters up to approximately one hundred meters in depth (Hauer and James, 2009).

In relatively few places where TZs have been explored by means of seismic method, the most common objective is often related to bridging the gap between onshore – offshore seismic data for better understanding of the geotectonic interplay between basins and adjoining regions. Some TZ areas have been explored for oil and gas purposes (e.g., Wyman and Ahmad, 2013; Roberts and FitzPatrick, 2015) and in recent times, some TZ locations have been found to be attractive sites for location of wind farms due to their proximity to offshore wind resource and relatively shallow water depth (e.g., Kim et al., 2013; Higgins and Foley,2014).

Seismic surveying is the most common and useful geophysical method for subsurface imaging. However, seismic exploration in TZ areas is often very challenging because of the water depth which is too shallow for conventional method of acquiring offshore seismic data using towed streamers. Seismic acquisition equipment and survey geometry are often adapted to the environment, and exclusion zones are taken into consideration when designing the survey. This is often necessary due to the presence of loose coastal marshes, rapidly varying bathymetry, inaccessible roads or paths, structural barriers, human / economic activities, and ecological factors. The consequence of these challenges is a compromise in data quality, thereby making data processing demanding.

The Ramså Basin is an example of an onshore – offshore TZ located in the north-eastern coast of Andøya, in northern Norway. It is the only location on mainland Norway where outcrops of Mesozoic sedimentary rocks are found (Dalland, 1975; Midbøe, 2011). The area has a long exploration history which began towards the end of the nineteenth century (see chapter Chapter 2:), and it is still being explored today. In 2012 and 2014, TZ-seismic datasets were acquired from the area in addition to other geophysical datasets (aeromagnetic, gravity, land and marine seismic) as part of a large-scale expedition by the Geological Survey of Norway (NGU) in collaboration with University of Bergen (Brönner et al., 2017). This geoscientific expedition sought to perform an integrated study and joint data interpretation to investigate the deeply weathered basement, and secondly to formulate a conceptual deformational model of the Ramså Basin for better understanding of the geology of the surrounding region.

TZ-seismic is a valuable part of the geophysical datasets that can contribute significantly to achieving the goals set out for the Ramså Basin survey. However, because of the constraints imposed by the complexity of the TZ area (see chapter Chapter 3:), data acquisition was affected by numerous obstacles which resulted to a complex set of TZ data difficult to understand and process using conventional processing workflows. In cases like this, seismic modelling can play a role in understanding the TZ data. It is a very useful tool for testing or validating interpretations or geological models inferred from seismic data (Lecomte et al., 2015). It can also be used for evaluation and design of seismic surveys (Carcione et al., 2002) and to analyze and understand complex seismic datasets (e.g., Mjelde et al., 1993; Liu et al., 2015).

By generating synthetic output from the modelling and comparing them to the real (observed) data, the seismic response of the real data can possibly be made less ambiguous. Furthermore, important information can be extracted from the modelling results which may prove useful for designing other acquisition survey geometries.

1.2 Aims and objectives

The aim of this thesis is to analyze one of the existing TZ-seismic section acquired from Ramså Basin. The focus is to use seismic modelling to better understand the real data and their limits and then propose new acquisition strategies for optimum imaging of the subsurface target along the TZ.

The objectives of the study are as follows:

1. Build a 2-D subsurface two-way time (TWT) model of the onshore – offshore TZ transect using available interpreted TWT horizons, velocities derived from well and seismic data, and densities calculated from well cores.
2. Convert the TWT model to depth.
3. Perform 2-D elastic FD modelling using similar TZ survey geometry applied in the field.
4. Generate synthetic seismograms for comparison with the real data.
5. Alter elastic properties in the model and repeat step 2 to 4 until an acceptable match between the synthetic and TZ data is achieved.
6. Perform seismic traveltime tomography to improve velocity model.
7. Use RT modelling to simulate traveltimes for different wave modes and generate traveltimes.
8. Analyze the real data using the RT-based traveltimes.

The objectives of the second part of the study are as follows:

1. Use RT modelling to simulate reflected waves from the target horizon (top Basement in this case) using various survey geometries.
2. Select the most suitable survey geometry that optimally illuminates the target.

1.3 Approach

In order to use seismic modelling for real data analysis, a reasonably accurate geological model of the subsurface area in which the data were acquired is essential. One way to determine the accuracy of a subsurface model is by computing synthetic seismograms based on the model by means of forward modelling for comparison with the real data. If a match is not established, the subsurface model is iteratively altered until the computed synthetic seismograms derived from a given model fits with the real data within a reasonable degree (Krebes, 2004; Sayers and Chopra, 2009; Alaei, 2012). The model will then be considered an approximate representation of the subsurface geology. In the present study, available data were used to construct an initial subsurface model of the TZ area. To validate the model, FD-based full wavefield synthetic seismograms were computed for visual comparison with the

real TZ-seismic data. The elastic properties of the model were then iteratively modified, and the FD modelling process repeated until a model is obtained from which the FD-based synthetic data are relatively comparable to the real data. The final model is based on a P-wave velocity derived via seismic traveltime tomography.

Using the final model, traveltimes for specific wave modes were computed from RT modelling. By studying the FD-based snapshots and comparing the modelled traveltimes with the traveltimes observed in the real data, possible locations of seismic events associated with a given wave mode can be identified in the real data. The RT and FD modelling methods used in this study are described in chapter Chapter 4:.

Chapter 2: Ramså Basin

2.1 Location

The Ramså Basin is located at the north-eastern coast of Andøya, which is the northernmost island within the Lofoten-Vesterålen archipelago in northern Norway. It is a downthrown faulted block with an area spanning about 10 km^2 (Midboe, 2011; Brönner et al., 2017). It is the only location on mainland Norway where outcrops of Mesozoic sedimentary rocks are found (Dalland, 1975; Sturt et al., 1979). Mesozoic sediments are of great importance because they constitute the hydrocarbon bearing source rocks on the NCS. Ramså Basin has generated a lot of interest over the years and has remained a center of attraction for studying Mesozoic sediments on land (see Exploration history). Figure 2.1 represents the map of Norway showing the location of Andøya (left) and the map of Andøya showing the location of Ramså Basin to the north-east (right). The basin lies in the western margin of Andfjorden (Andfjorden Graben).

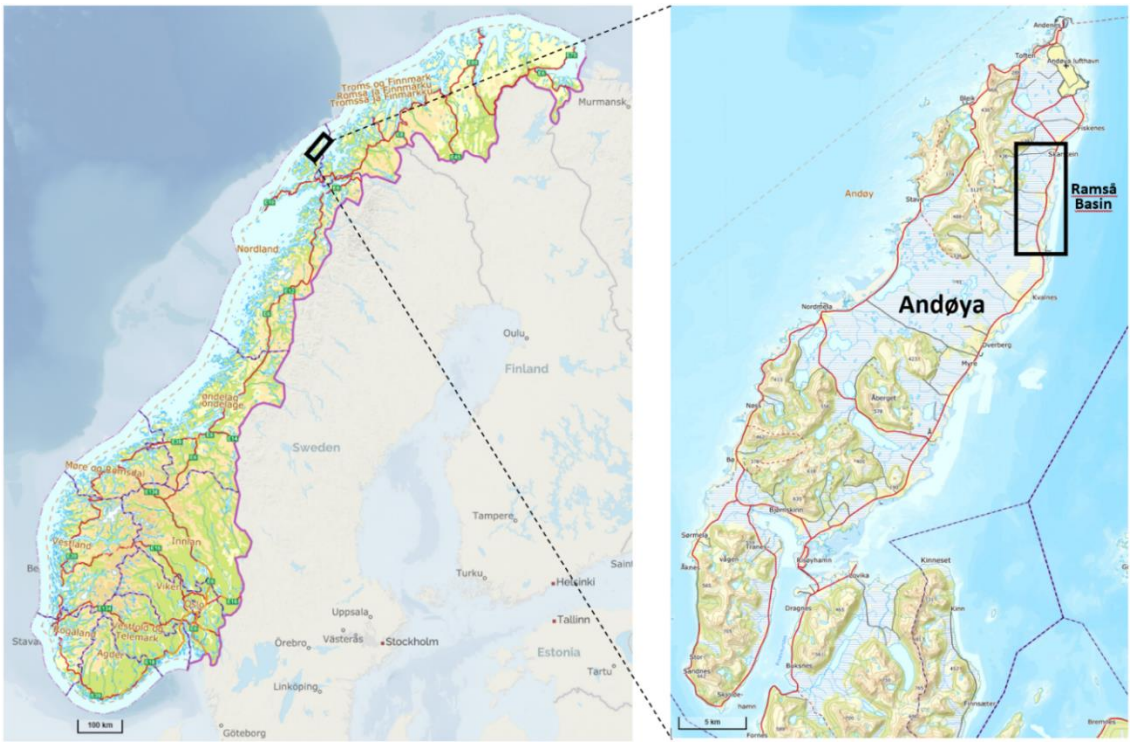

Figure 2.1: Geographical map of Norway showing the location of Andøya and Ramså Basin. Modified from norgeskart.no

2.2 Exploration history

Historically, the area started witnessing a lot of interest after coal was discovered in a farm located within the Ramså field in 1867 (Midbøe, 2011; Peterson et al., 2013). The occurrence of these coal deposits was first documented by Tellef Dahll in 1891 (Midbøe, 2011). In an effort to delimit the coal deposit, five exploration wells were drilled from 1869 to 1873 (Helland, 1897). About a decade later, more wells were drilled from which core samples were extracted for further studies, most notably by Friis, 1903 and Vogt, 1905 whom contributed to the basic understanding of the subsurface stratigraphy and structural framework of the Ramså Basin (Midbøe, 2011). The coal deposits were exploited at various times, however large-scale production never took place because the coal deposits were not available in commercial quantities.

Apart from outcrop observations and geological examinations of well cores and rock samples obtained from near-surface excavations, refraction seismic surveys were also performed at Andøya between 1969 and 1971. The objective of the survey was to determine the structure of the Jurassic – Cretaceous sediments based on seismic velocities, and correlate them with the velocity structure of sediments deposited on the continental shelf off the coast of northern Norway. (Dalland et al., 1973; Dalland, 1975).

Soon after it became known that Mesozoic sediments are the hydrocarbon bearing source rocks on the Norwegian Continental Shelf (NCS), Norminol Oil Company, a locally based company, drilled four more wells in the area between 1972 and 1974 for oil and gas exploration (Peterson et al., 2013). The locations of the wells are shown in Figure 2.2. There is no record of hydrocarbon discovery in the area.

Apart from the known hydrocarbon generating qualities of the Mesozoic rocks on the NCS, weathered basement rocks upon which these Mesozoic sediments are overlain have in recent times also generated a lot of interest. Discoveries on the Utsira High (Edvard Grieg and Johan Sverdrup fields), indicate that fractured basement rocks which were altered due to subaerial weathering acts as hydrocarbon-bearing reservoir rocks and possible migration paths for commercial hydrocarbon deposits on the NCS (Riber et al., 2015). This discovery is of great economic importance but questions the integrity of the basement rocks for construction projects like subsea tunnels through them, especially where the extent of deep weathering is unknown (Brönner et al., 2017).

For these reasons, Ramså Basin has continued to remain a strategic location where various geological and geophysical explorations are undertaken, one of the most recent being in 2012 and 2014 by the Geological Survey of Norway (NGU) in collaboration with University of Bergen (Brönner et al., 2017). In this latest campaign, seismic (land, marine, and TZ); aeromagnetic; and gravimetric datasets were acquired. Four new wells were also drilled from which the following measurements were logged: velocity, resistivity, temperature, electric conductivity, total natural gamma radiation, gamma spectroscopy, magnetic susceptibility, induced polarization, self-potential and acoustic televiewer (Brönner et al., 2017).

2.3 Geology

The sedimentary rocks in the Ramså field were deposited in the Mesozoic era between Middle Jurassic to Early Cretaceous period. These rocks overlay basement rocks which are typically granodiorite, gabbro, and granite (Dalland,1975; Midbøe, 2011; Baranwal et al., 2020). The sedimentary rocks are dominated by sandstone with different amount and varieties of clay and shale content. Figure 2.2 is a simplified geological map of Ramså Basin.

The area is a partially faulted downthrown block in which Middle Jurassic to Early Cretaceous sediments of up to 900 m thick are deposited (Zwaan et al., 1998). Outcrop of weathered basement of about 32 m in thickness is observed in the southern part of the basin (Sturt et al., 1979). It is believed that the weathering zone, and thin remains of Palaeozoic sediments which were hitherto very thick, underlay the Middle Jurassic sediments (Dalland, 1981).

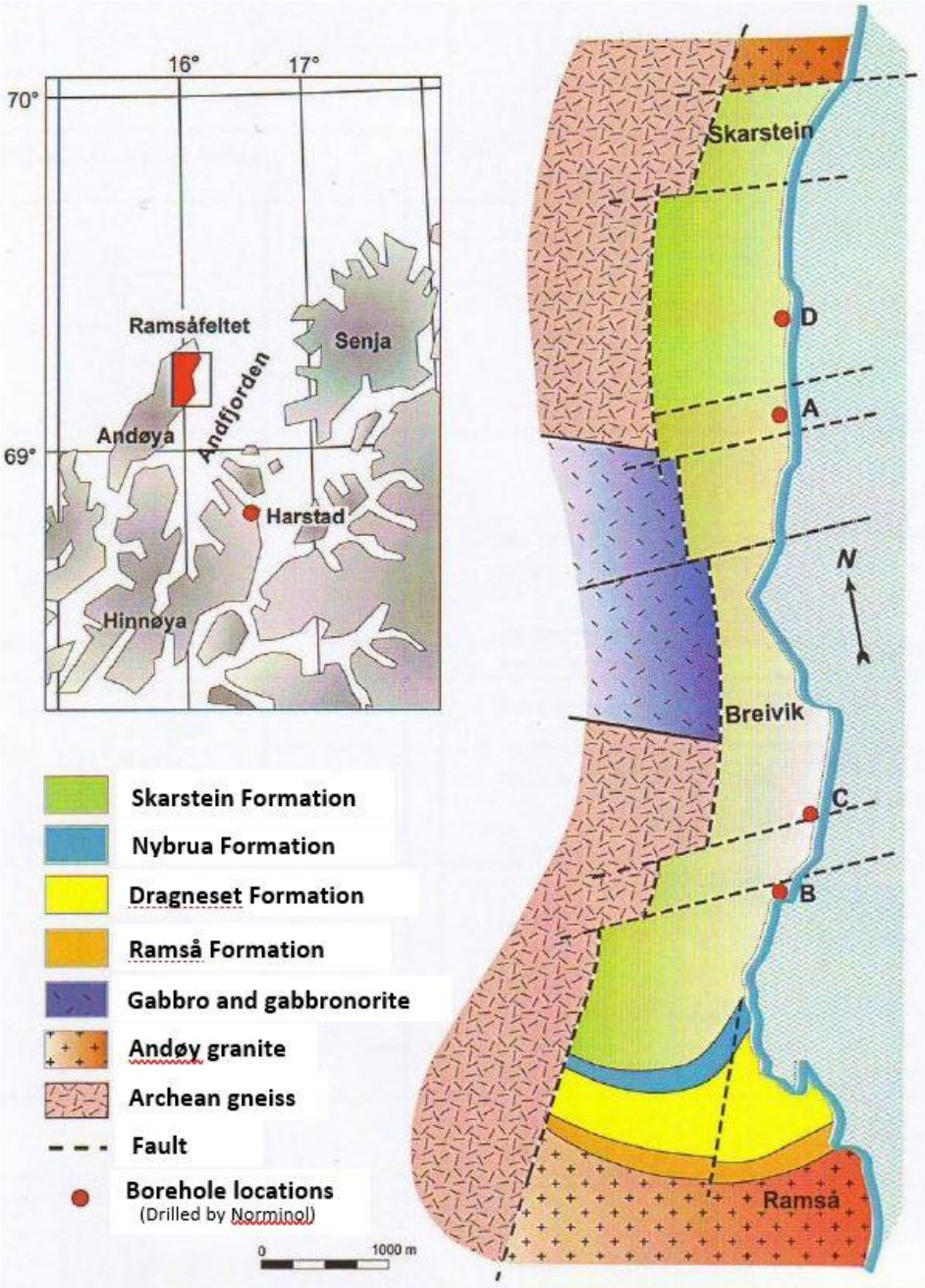

Figure 2.2: Simplified geological map of Ramså. The location at the north-eastern flank of Andøya is highlighted in red on the map to the left. Originally from Dalland (1980), modified from Midbøe (2011).

Outcrops of Mesozoic sedimentary rocks are exposed on the strandflat which are mostly overlain by peat swamps, beach ridges and Quaternary moraine (Figure 2.3).

Figure 2.3: Outcrops of Mesozoic sedimentary rocks on the beach at Ramså field with a view to the north. From Midbøe (2011).

A Mid-Jurassic faulting is responsible for an uplift to the west of Andøya which resulted to the formation of Ramså Basin to the east which extends under the main graben structure (Andfjorden) and probably continuous with the thick pile of sediments (Dalland, 1975). The area is bounded by faults except for the southern part of the area. The main direction of the faults are NNE - SSW, but faults in the E-W direction are also common (Dalland et al., 1973). Generally, the region is characterized by a complex system of uplifted and rotated basement blocks, where the various islands within the Lofoten - Vesterålen archipelago represent the exposed part of a basement high (Brönner et al., 2017). Figure 2.4 is a cross-section of the subsurface structure inferred from well logs obtained from Norminol wells A, B, C and D. From the figure, a basement high is shown in the north and a trough southward.

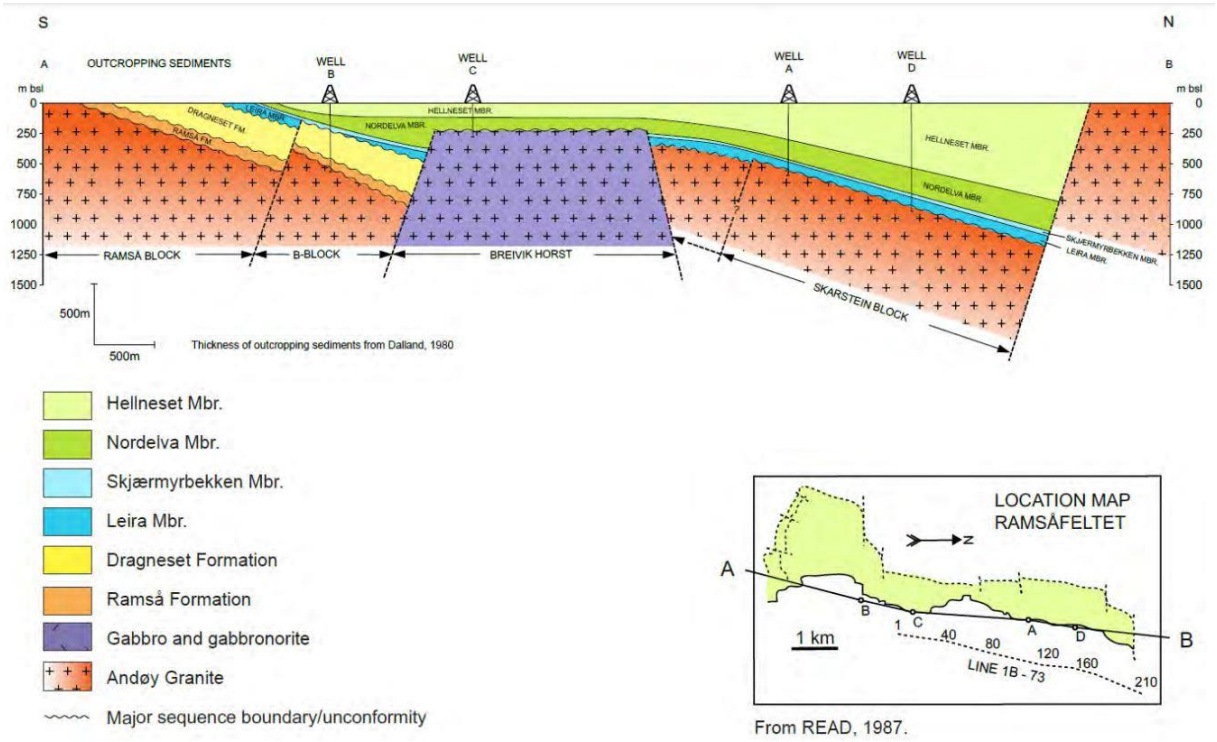

Figure 2.4: Cross-section of the subsurface structure along Norminol wells A, B, C, and D based on well logs. From Midbøe (2011).

2.4 Stratigraphy

In Ramså Basin, sedimentary rocks of Jurassic and Lower Cretaceous age are found in the southern trough, however, in the northern outcrop, rocks of Lower Cretaceous age constitute the main deposits (Dypvik, 1979), see Figure 2.4. These sediments lie unconformably on weathered basement (Dalland, 1975). The stratigraphic description of the area is mostly based on core samples extracted from different wells drilled in the area, including excavations and velocities derived from refraction seismic. Figure 2.5 represents the Mesozoic sedimentary succession at Ramså Basin, north-east Andøya. A brief description of the formations and lithology of their associated members are given below.

2.4.1 Basement

The basement complex comprises of coarse-grained granodiorite pluton (also known as the Hinnøya granodiorite) of Archaean age, and partly weathered gabbro of Early Proterozoic age (Brönner et al., 2017). The granodiorite pluton, which is the dominant basement rock is composed of quartz, feldspar, and mica (Brönner et al., 2017).

2.4.2 Weathered Basement

Before sedimentation began, the fractured basement rocks were deeply weathered (Dalland, 1975; 1981; Sturt et al., 1979). Deeply weathered Hinnøya granodiorite composed of quartz, K-feldspar and kaolinite is exposed in the area (Brönner et al., 2017). The weathering process is believed to have started during a period of humid climatic conditions prior to or during Early Jurassic period (Dalland, 1975).

2.4.3 Basal Limestone (Holen Formation)

From borehole data, an enigmatic sandy limestone of about 6 m thick is observed to overlay the weathered basement in a small segment of the area (Dalland, 1975; 1981). This layer which has not been observed in outcrop is now known as Holen Formation.

2.4.4 Ramså Formation

The downthrown fault block at Ramså field setup the process for deposition of Ramså formation which overlays the weathered basement. This downthrown block served as a local depocenter, and it is only close to this center that the enigmatic limestone and weathered basement were protected from erosion (Dalland, 1975; 1981). The source of the first sediments that were deposited were from the weathered basement (Dalland, 1975). Members of the formation include: Hestberget, Kullgøfta and Bonteigen.

Hestberget Member is about 30 m thick around the depocenter of the basin, but the thickness decreases rapidly away from the center in all directions, especially towards the northwestern part of the basin (Dalland, 1975). The sediments consist of coarse-grained sandstone interbedded with kaolin-rich shale, bituminous shale, micaceous siltstone, and a few layers of cannel coal. The lowest sandstone beds contain irregular quartz grains and little feldspar (Dalland, 1981).

Kullgrøfta Member overlays Hestberget member. A maximum thickness of about 12 m is observed, but just like the underlying member, the thickness also decreases away from the center in all directions (Dalland, 1975; 1981). It is dominated by dark-brown shales, few layers of micaceous siltstones and fine-grained sandstones (Dalland, 1975).

Bonteigen Member is about 55 m thick around the depocenter and decreases away from the center, but more rapidly towards the north-west where a thickness of about 25 m is observed about one kilometer away (Dalland, 1975; 1981). A significant unconformity is identified in this member which marks a transgression from lacustrine / paralic deposition below to open-marine deposition above (Brönner et al., 2017). The sediments consist of medium to coarse grained sandstones interbedded with shaly micaceous siltstones, few layers of bituminous shale and thin coal layers in the middle and lower part of the member. The upper part of the sandstones is calcareous and contain marine fossils, including few glauconite-rich layers which are also found near the top of the member (Dalland, 1975).

2.4.5 Dragneset Formation

The Dragneset Formation grades from medium to fine grained sandstone at the bottom to a fairly continuous sequence of siltstone in the middle, and shaly siltstones in the upper part (Dalland 1975; 1981; Bøe et. al., 2010). The formation is about 290 m thick and divided into three members: Breisanden, Taumhølet and Ratjønna.

Breisanden Member is about 40 m thick at the depocenter but decreases away towards the north-west (Dalland, 1975). It is composed of medium to fine grained sandstone with a few calcareous layers. Marine fossils are common, including a few vertebrate fossils (Dalland, 1975).

Taumhølet Member is about 150 m thick at the depocenter. It consists of mainly micaceous siltstones and fine-grained sandstones, with a few shaly layers. The sediments are dark grey due to presence of finely dispersed plant material (Dalland, 1975).

Ratjønna Member is about 100 m thick. It is dominated by partly laminated siltstone layers. The sediments are mostly dark in color, and just like the underlying member, the color is due to presence of dispersed plant material (Dalland, 1975). Marine fossils are common and some layers of hard, light and slightly calcareous sandstone are found in the upper part of the member (Dalland, 1975; 1981).

2.4.6 Nybrua Formation

According to Dalland (1975), the boundary between the underlying Dragneset Formation and Nybrua Formation seems to represent a period of non-deposition (unconformity). The

formation is nearly 80 m thick and dominated by calcareous sandstones and siltstones. It is divided into two members: Leira and Skjermyrbekken.

Leira Member is about 50 m thick and mainly composed of hard calcareous sandstone with intercalations of mildly calcareous siltstones. Deep vertical burrows are preserved in many of the sandstone layers (Dalland, 1975; 1981).

Skjermyrbekken Member is about 30 m thick and is dominated by brownish-red siltstones. Owing to the presence of slump structures found throughout the sequence, original layering of this member proved difficult (Dalland, 1975).

2.4.7 Skarstein Formation

The Skarstein Formation overlays the Skjermybekken Member of the Nybrua Formation. The sediments are composed of dark fine grained colored rocks, which ranges from siltstones and silty shales at the lower section, and mudstones, shales, and thin beds of sandstones in the upper section (Dalland, 1975). It is the thickest formation in the area, reaching up to 720 m as observed in well D (Brönner et al., 2017), see Figure 2.4. It is divided into two members: Nordelva and Hellnesset.

Nordelva Member is at least 70 m thick and consists of mainly dark siltstones, silty shales, and mudstones (Dalland, 1975). Few amounts of mica are found in most of the layers, including finely dispersed plant remains, and trace fossils (Dalland, 1975; 1981).

Hellnesset Member is dominated by dark colored shale and mudstone intercalated with a few layers of sandstone (Dalland, 1975). As seen from Figure 2.4 in well D, the thickness is at least 550 m. The fine grain sediments contain significant amount of dispersed organic material, including trace fossils and a few marine fossils (Dalland, 1975; 1981).

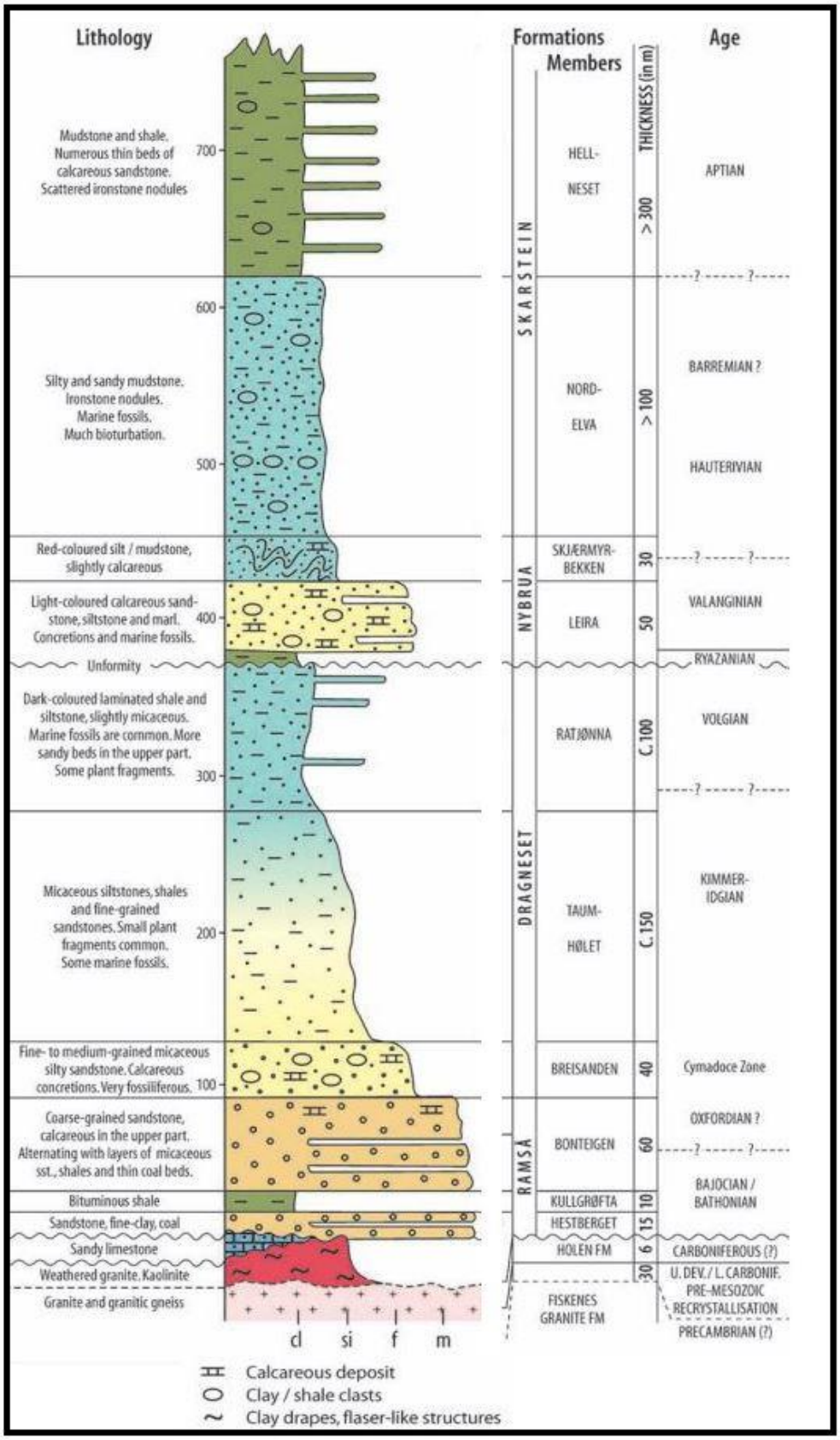

Figure 2.5: The Mesozoic sedimentary succession on Andøya. Originally from Dalland (1981), modified from Bøe et al. (2010).

Chapter 3: Onshore – offshore TZ-seismic

3.1 TZ

An onshore – offshore TZ can be described as an area ranging from shallow water near the coast to the coastline and further onto wet unconsolidated land. The environmental setting varies from place to place but they are generally dynamic and complex in nature. The area can include land, fresh and saltwater marsh, and swamp, near shoreline, surf and tidal zones, lagoons, shallow offshore coral reefs, and deeper waters up to approximately one hundred meters in depth (Hauer and James, 2009).

TZ subsurface images can be used to link similar images along the same onshore – offshore transect. By linking the datasets, valuable insights for developing better geological models for better understanding of the basin development and their tectonic relationship with surrounding region can be achieved. Seismic surveys are the most common and useful geophysical method for subsurface imaging and this method is also applied in TZ areas. However, the area is one of the most challenging terrains for data acquisition (Hauer and James, 2009; Aouad et al., 2012; Roberts and FitzPatrick, 2015). Hence, data acquired from the area can also be difficult to process and image.

3.2 Motivation for TZ-seismic - The Ramså Basin case

Deeply weathered Precambrian basement rocks have long been reported to underlay the Mesozoic sediments around the Andøya region (Friis, 1903; Dalland, 1975; 1981; Dypvik, 1979). These weathered basement rocks have also been observed, studied and reported by Paasche et al., (2006); Brönner et al., (2010) and Olesen et al., (2012). Some studies have suggested that the development of the strandflat landform observed along the coast of Andøya and many other areas along the Norwegian coastline is related to deep weathering (Olesen et al., 2013; Brönner et al., 2017).

The presence of weathered basement rocks is a great concern, especially for construction works, hence a geotechnical investigation to determine the extent of weathering is necessary and Ramså Basin is a perfect site for this kind of study. For this reason, a large-scale geological, geophysical and petrophysical study was conducted at Ramså Basin in 2013 and 2014, including seismic acquisition campaigns. The project was particularly set out with two objectives in mind:

- Test the likelihood of identifying deeply weathered basement from seismic images, including other geophysical, geological and petrophysical datasets.
- Develop a tectonic evolution model of Ramså Basin to improve the understanding of the regional geology of Andfjorden and the Lofoten-Vesterålen archipelago.

TZ-seismic data are a valuable component of several datasets acquired to achieve the set objectives. Details of the entire geophysical operation at Ramså Basin, including data processing and interpretation are documented in a 2017 NGU report (Brönner et. al.,2017). Johansen et al., (2020) reviewed the processing and interpretation of the onshore segment of the seismic data.

3.3 TZ-seismic data acquisition – The Ramså Basin case

The Ramså Basin TZ area is characterized by loose coastal materials (peat swamps, sand dunes, and Quaternary moraine), rapidly varying bathymetry and complex near subsurface geology. Landwards, there are inaccessible roads, structural barriers, and human / economic activities. Given the nature and diversity of the terrain, the seismic datasets were acquired in three different runs, as seasonal conditions which can be safe and favorable for efficient data collection using available equipment were taken into consideration. Figure 2.1 shows the map of the area, including the layout of all the seismic lines acquired.

Lines 1, 4 and 6 were acquired on dry land along existing roads in the autumn of 2013. The seismic source employed was a Vibsist (model: 3000). The source generates seismic energy using the Swept Impact Seismic Technique (SIST) which is an efficient and cost-effective technique well-adapted for shallow reflection surveys where high resolution and cost-effectiveness are critical (Park et al., 1996).

The area on which lines 2, 3 and 5 were positioned are characterized by peat swamps and were acquired in the winter of 2014 on frozen ground using a detonating cord source. However, 10 Hz geophones with soil spikes were used as receivers in both runs. Shallow marine lines (M2 to M12) were acquired in the autumn of 2014. The receiver array consisted of a short 50 m long mini-streamer containing eight receiver groups of which one was malfunctioning. Each receiver group consists of many hydrophones which are recorded as one channel. A 90 cu. inch single air gun was utilized for most of the marine lines. Four of the shallow marine seismic lines M3, M4, M5 and M6 were acquired along the same eastward orientation as the corresponding land seismic lines 3, 4, 5 and 6.

In addition to the land and shallow marine seismic lines, four TZ-seismic lines were also acquired to fill the gap between the four shallow marine seismic lines and land seismic lines placed along the same orientation. The lines marked red in Figure 3.1 represent source points for the TZ-seismic survey. The source is a small array consisting of four air guns with a total volume of 766 cu. inch. These air guns were used to generate acoustic waves at sea and simultaneously recorded marine seismic data with the streamer hydrophones along the lines offshore, and TZ-seismic with the geophones stationed along lines 3, 4, 5 and 6 on land. The TZ-seismic lines are within the area highlighted with dashed black lines in Figure 3.1.

It is not uncommon to use multiple seismic equipment when acquiring TZ-seismic data (e.g., Aouad et al., 2012; Roberts and FitzPatrick, 2015; Brönner et al., 2017). Apart from seasonal conditions, accessibility also plays a role in the choice of seismic equipment. For instance, during acquisition of the land seismic segment at Ramså Basin, detonating cord (explosive sources) were used in unmotorable areas which were considered far enough from human settlements. On the other hand, where motorable roads or trails exist which are mostly nearby inhabited buildings, a vibsist-3000 seismic source was used to avoid possible damage to buildings that may occur from the strong air waves that is generated by the detonating cord.

In some TZ areas, the landscape can range from undulating plains to low-lying hills and flat land. In such areas, the diversity of terrain, including the coastal shallow waters and nearshore relatively deeper waters can entail the survey being acquired using a range of seismic sources, including mid-range vibrators, dynamite, and air guns, and recorded into land and swamp geophone cable, rod hydrophones, and ocean bottom nodes (e.g., Roberts and FitzPatrick, 2015).

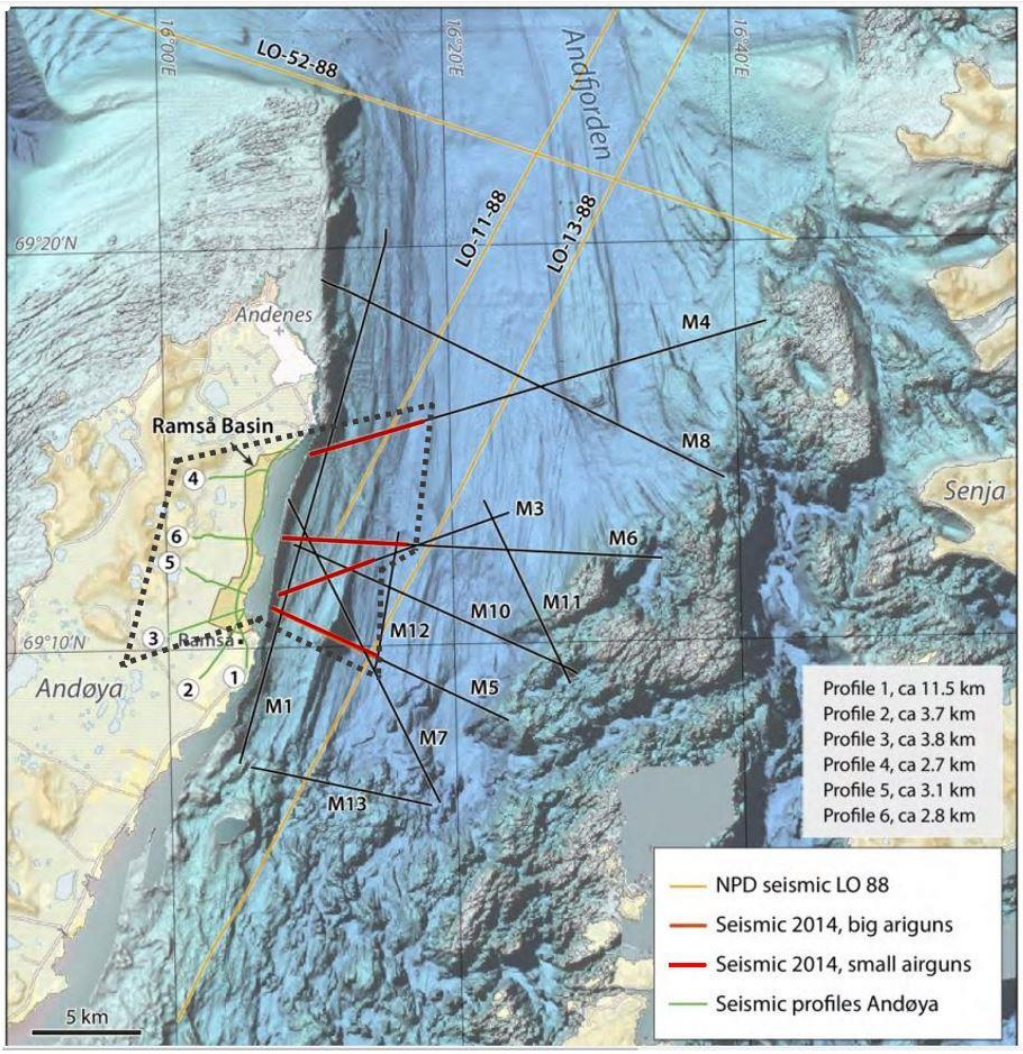

Figure 3.1: Map of the study area showing the land seismic lines (1 – 6), the 10 shallow marine seismic lines (M2 - M12) and the TZ-seismic source – receiver positions (red and green, respectively) in the area highlighted with dashed black lines. LO-11-88, LO-13-88 and LO-52-88 are old seismic lines which were acquired in 1988 using both 0.5 km and 3 km streamer. Modified from Brönner et. al. (2017).

Ocean Bottom Cable (OBC) or Ocean Bottom Node (OBN) seismic acquisition method which was primarily developed for shallow water regions are applied in some TZ areas (e.g., Aouad et al., 2012; Roberts and FitzPatrick, 2015; Liu et al., 2015). Typically, shallow OBC seismic exploration method can be used in areas where water depths are between approximately 50 m to 500 m.

When shallow OBC or OBN seismic is used in combination with TZ-seismic, specialized vessels and equipment are utilized in both applications to accommodate the appropriate water depths, hence creating significant operational variance between the two methods, particularly

in how crews deploy equipment (Hauer and James, 2009). Basically, operators must utilize equipment that can adapt to the diversity of terrain to meet various survey objectives. The combination of different source types and different receiver types will require recording systems which can efficiently support mixed-mode acquisition where source points can vary between air gun, dynamite, or vibroseis that are potentially shooting into 1C, 2C, 3C and/or 4C receiver stations simultaneously (Hauer and James, 2009).

Human / economic activities, structural barriers and environmental regulations were also among the challenges encountered during the Ramså Basin seismic acquisition. For instance, during acquisition of the land segment in the area, the impact (shot) sampling points using the vibsist-3000 seismic source was restricted only to motorable roads or paths and not along presumed optimum shot points. Moreso, due to environmental restrictions, the marine seismic lines were shot partly with a single air gun and partly with an array of air guns. One marine seismic source type, preferably an air gun array would have been sufficient. Ideally, air gun arrays are desirable sources in marine seismic surveys because they generate much louder sounds and stronger signatures than the single air gun which is too weak to generate good signal-to-noise ratio especially at depth (Dragoset, 2000). In addition, the choice of using a very short 50 m mini-streamer instead of a 3000 m streamer which is the available alternative was to avail the possibility to shoot as close as possible to the shore. Multiple attenuation in data acquired with a short streamer is difficult because of the small differences in Normal Moveout (NMO) between primaries and multiples.

Apart from the nature of the environment, the extent of environmental laws can also play a significant role in the success of data acquisition (Hauer and James, 2009) and in some cases, new laws are enacted in the process of seeking for data acquisition permits (Aouad et al., 2012).

3.4 TZ-seismic data processing – The Ramså Basin case

The challenges that are encountered during TZ-seismic data acquisition often translates to complex datasets that can be difficult to process. The rapidly varying environment, exclusion zones, equipment restriction and proximity to sources of noise can affect the data quality. Apart from noises associated with human activities near shore, the large fluctuations in water levels and noise associated with wave action can also lead to poor data quality (Larry and Ahmad, 2013). Moreso, combination of datasets that were acquired with different source –

receiver pairs, each with unique noise characteristics and statics, covering separate but overlapping Common Mid Points (CMP) can constitute a major challenge in processing (e.g., Aouad et al., 2012).

Noise attenuation and careful computation and application of refraction static corrections are crucial part of the processing routine for land segments of data acquired around TZ areas (e.g., Aouad et al., 2012; Johansen et al., 2020). In the Ramså Basin case for example, the movement of the vibsist-3000 land seismic source was along existing roads, hence the vibrations from moving vehicles along the road introduced ambient noise into the data (Brönner et al., 2017; Johansen et al., 2020). These unwanted signals were recorded as high energy events, thereby reducing the signal-to-noise ratio of the data. The ambient noise together with transient noise like low-frequency noise from the impact of the waves near the seashore were attenuated using specially designed processing techniques (see Johansen et al., 2020). Figure 3.2 illustrates the impact of the noise generated by vehicular movements on the data, and after attenuation of the noise.

The land segment of the Ramså Basin TZ area is also characterized by topographic variations, and near surface unconsolidated geological / structural variations. For this reason, a refraction statics correction is required to compensate for the effects of these variations and reference the data to a common origin (Johansen et al., 2020).

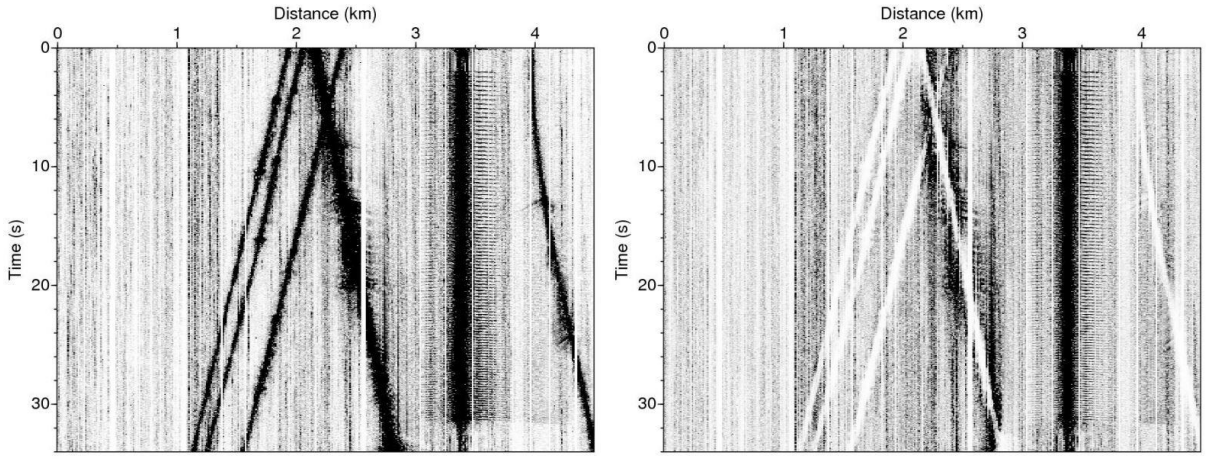

Figure 3.2: Raw data from a single sweep on land seismic line 1 marred by noise generated from vehicular movements (left) and the same data after noise suppression (right). From Johansen et al. (2020).

These variation effects are observable on the first-arrival curve. This is due to compressional waves propagating within the layer underlying the unconsolidated and rapidly varying surface as head waves near the interface between them. These compressional waves arrive earlier in time as refracted first breaks, thereby altering the steady and smooth delays in arrival times with offset between receiver levels. The time shifts applied for static corrections were computed using first-arrival times within offset ranges where the arrival wavelets were observed to be more stable (Brönner et al., 2017; Johansen et al., 2020). Figure 3.3 illustrates the effect of the variations on the data and after application of refraction statics correction.

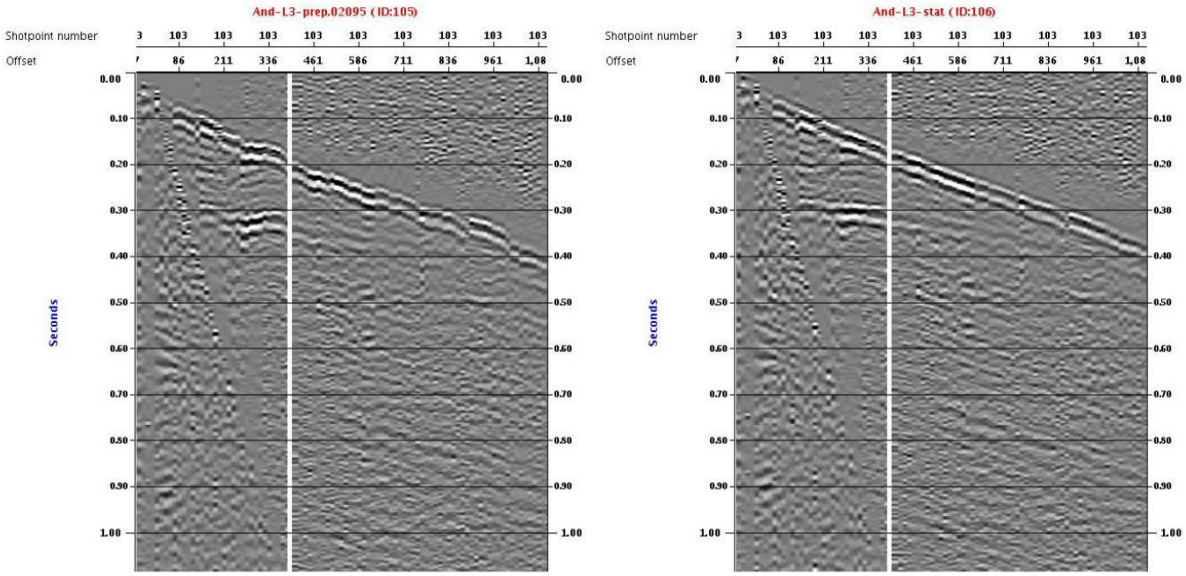

Figure 3.3: Data from a single receiver along line 1. Before static correction (left) and after static correction (right). From Johansen et al. (2020).

The reflection events in the Common Mid-point (CDP) gathers were too weak to be observed clearly in the datasets within the land segment, hence typical velocity analysis for obtaining NMO velocities (stacking velocities) could not be performed. However, velocities were computed via a seismic tomography inversion method based on first breaks (Brönner et al., 2017; Johansen et al., 2020). The technique has the capability of jointly inverting the refraction and reflection travel times for a 2-D velocity structure using a hybrid RT scheme hinged on the graph method (Korenaga et al., 2000). It assumes that the velocity within the subsurface is smooth and increases with depth. This velocity model was used to image the data in time domain, thus making the seismic events more observable. With the migrated

image, a typical velocity analysis was performed to obtain a final velocity model used for final imaging of the data. Details of the processing are documented in Brönner et al., (2017) and Johansen et al., (2020).

For the marine seismic sections, velocity analysis could not be performed due to the short source – receiver offset window of the 50 m long streamer. A stacking velocity model was computed with an assumed constant interval velocity of 3500 m/sec below the seabed. This velocity was estimated from refracted waves in the seabed below a thin layer of loose Quaternary deposits, using the marine seismic data acquired in 1988. The stacking velocity model was then used to migrate the marine seismic sections.

The main challenges that impacted processing of the Ramså Basin marine seismic segment (Andfjorden), including the TZ-seismic are summarized from Brönner et. al., (2017), see below:

- A single air gun source was used in areas where environmental restrictions apply, hence reducing the signal quality.
- The complex near subsurface geology and inability to use optimum survey design due to exclusion zones, made 3-D effects unavoidable.
- A short streamer was used to allow shooting close to the shore. This implies short source – receiver offset, hence making it difficult to distinguish and attenuate multiples because of insufficient reflection moveout times between the primaries and multiples. Figure 3.4 displays a Common Shot Gather (CSG) from a single shot along TZ-seismic line 3. Notice how the events are closely parked together with almost similar moveout times.
- The seabed velocities are also quite high, hence generating very strong multiples.
- Due to the rapidly varying bathymetry offshore (Figure 3.1), the seabed multiples mask or distort events deeper than its arrival time, hence making events below the multiple arrival time difficult to interpret.
- In addition to Mesozoic sediments, Precambrian basement rocks also dominate in the area. Basement rocks are usually very difficult to image using seismic method because they have very high seismic velocities and therefore low seismic resolution due to low acoustic impedance contrasts between the rocks.

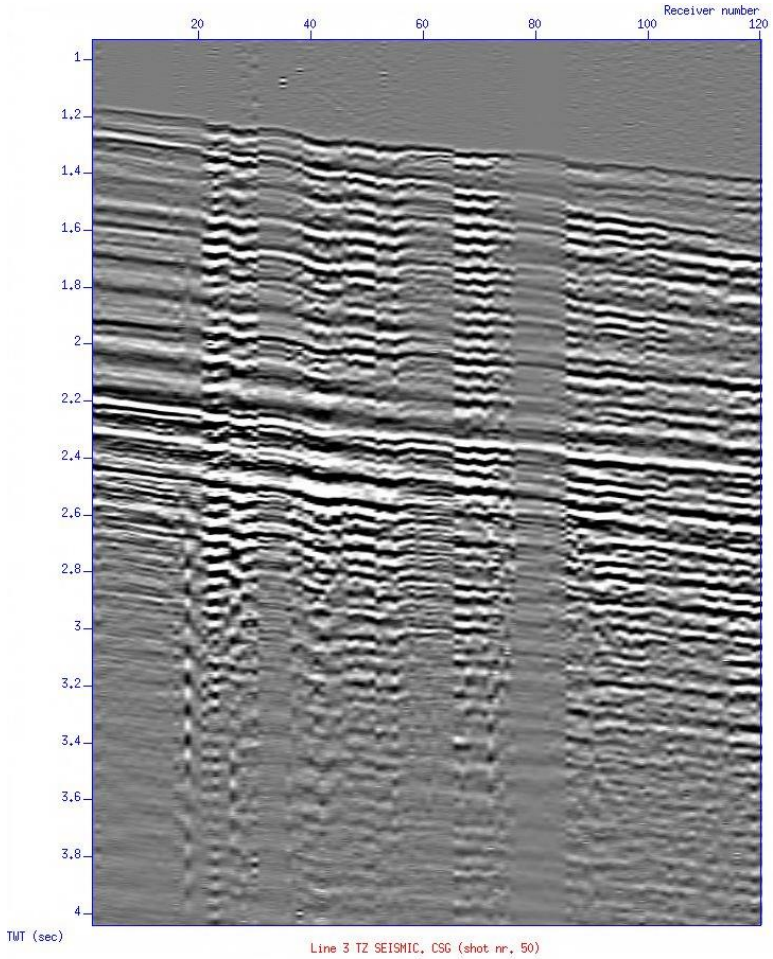

Figure 3.4: CSG from a single shot along TZ seismic line 3.

Nevertheless, some of the processable seismic sections especially those acquired within the land and marine (Andfjorden) segments were processed. The resulting subsurface image sections produced within the limits of the challenges encountered is encouraging (see Brönner et al., 2017; Johansen et al., 2020).

The onshore – offshore TZ-seismic sections were particularly difficult to process due to bathymetry effects and interference of different wave modes in the datasets (Brönner et al., 2017). Figure 3.5 illustrates the effects of bathymetry on the TZ and marine seismic data.

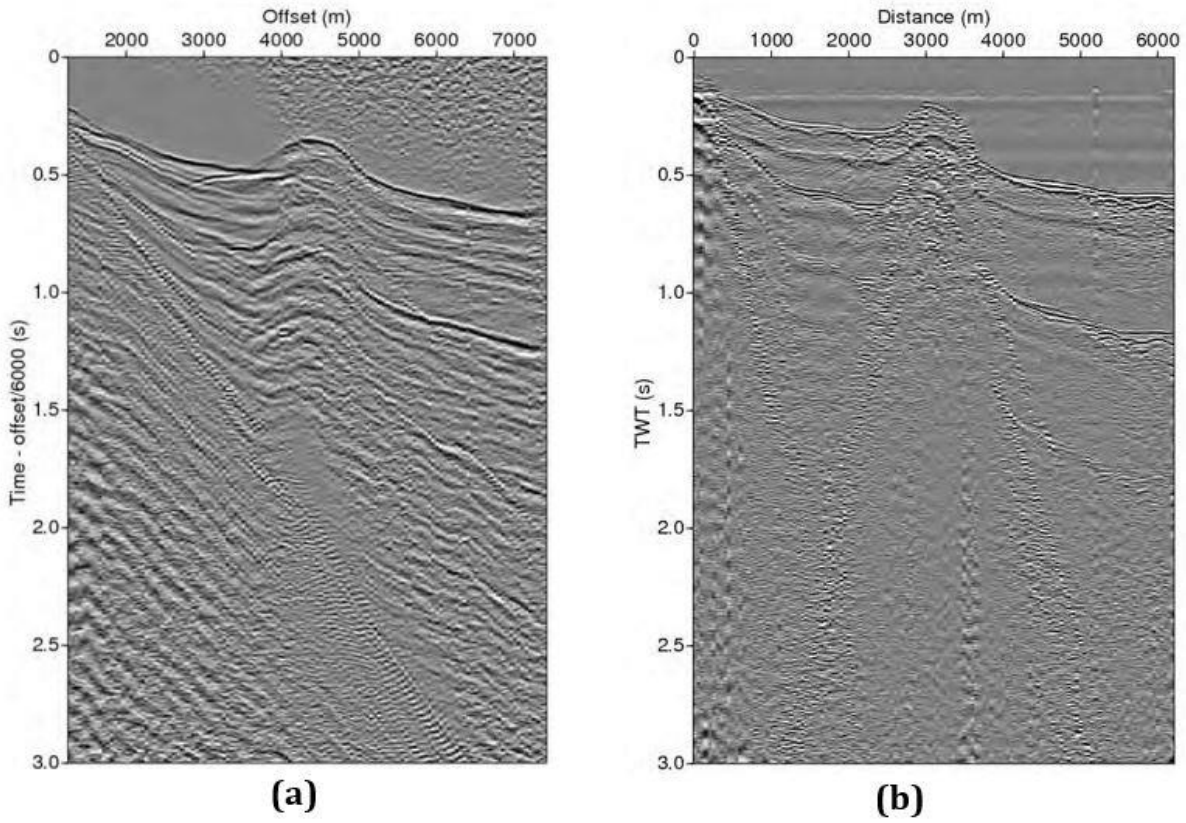

Figure 3.5: (a) Common Receiver Gather (CRG) of TZ-seismic line 5 recorded on land by receiver number 11. (b) Near trace seismic data obtained along marine seismic line M5. From Brönner et al. (2017).

Although an integrated interpretation of Ramså Basin using successfully processed seismic and other geoscientific datasets have been presented and discussed (Brönner et. al.,2017), these yet to be processed TZ-seismic datasets have the potential of improving upon the knowledge already acquired from the studies.

3.5 Importance of TZ-seismic

Over the years, seismic exploration has been associated with oil and gas, therefore the increasing demand for a transition to renewable energy due to climate change have led to increasing negative sentiments towards it. However seismic exploration, more specifically, TZ-seismic can play a vital role in the drive towards renewable energy transition. This is because TZ areas have been found to be the preferable sites for wind farms due to their proximity to offshore wind resource which are higher and more stable than potential onshore locations. In addition to offshore proximity and other criteria, water depth is also an important

factor for determining the eligibility of sites suitable for developing wind farms (e.g., Kim et al., 2013; Higgins and Foley,2014).

It is more economical to locate wind farms within TZ territory because operational cost increases with increase in water depth. Moreso, current technologies provide the possibility to develop marine wind farms at a maximum depth of 60 m with a stable offshore structure (Vagiona and Kamilakis, 2018). For example, most offshore wind farm projects in the United Kingdom that are operational or have consent are located at water depths of between 20 m and 40 m and at distances of 20 km to 40 km from shore (Higgins and Foley, 2014). As wind farm projects continue to grow across the globe, seismic based studies along TZ areas can provide useful information about the subsurface integrity and stability of the foundations upon which the wind turbines are built.

TZ-seismic data can also bridge the gap between marine and land seismic data which are relatively abundant, thus providing valuable subsurface information, including a better understanding of the historical processes that led to present day geological settings in regions where they occur.

Chapter 4: Theoretical background

4.1 Seismic modelling

Seismic modelling is a numerical simulation of seismic wave propagation in the subsurface to predict the seismogram that a set of seismic receivers would record, given an assumed subsurface structure (Carcione et al., 2002). It is a very useful tool for conceptual testing or validation of geologic models inferred from interpretation, provided that all necessary input information for constructing the model is available and an appropriate modelling method is used (Lecomte et al., 2015). Ray tracing (RT) and Finite difference (FD) modelling methods in particular can be used to analyze and understand complex seismic datasets (e.g., Mjelde et al., 1993). Another application of seismic modelling is the evaluation and design of seismic surveys (Carcione et al., 2002; e.g., Masoli et al., 2020). By evaluating the survey area prior to data acquisition, potential illumination and resolution effects (see Lecomte and Gelius,1998; Gjøystdal et al., 2002 and Lecomte, 2006; 2008) based on a given survey geometry can be known in advance, and if necessary, a target-oriented survey can be simulated to determine the optimum survey geometry that can minimize these effects and meet the survey objectives. Seismic modelling can also be used post-acquisition to estimate the effects leading to a loss of resolution in a migrated image and this information can then be used to adjust the migration parameters to improve the results (Lecomte, 2008). Complex seismic datasets can also be analyzed via seismic modelling to mitigate uncertainties and understand the data better (e.g., Mjelde et al., 1993; Liu et al., 2015). This chapter gives a brief overview of the basic theories that provide the backdrop for seismic modelling and the modelling methods (RT and FD) used in this thesis.

4.2 Basics about seismic waves and rays

When seismic energy is generated by either a natural or controlled (artificial) source, the energy radiates outward from the source point and propagates through the earth in all directions as elastic (seismic) waves. The edge of the seismic wave energy vibrating in the same phase is known as wavefront and several studies of seismic wave propagation in 3-D are best performed using wavefronts (Gadallah and Fisher, 2009). Wavefronts can be simulated with RT as the loci of points with equal traveltime at a given propagation time.

In an isotropic media, all rays will be perpendicular to a given wavefront (Gelius and Johansen, 2010), beginning at the source location and connecting equivalent points on successive wavefronts, thus representing the direction of wave motion (Gadallah and Fisher, 2009). Figure 4.1 shows the relationship between wavefronts and rays.

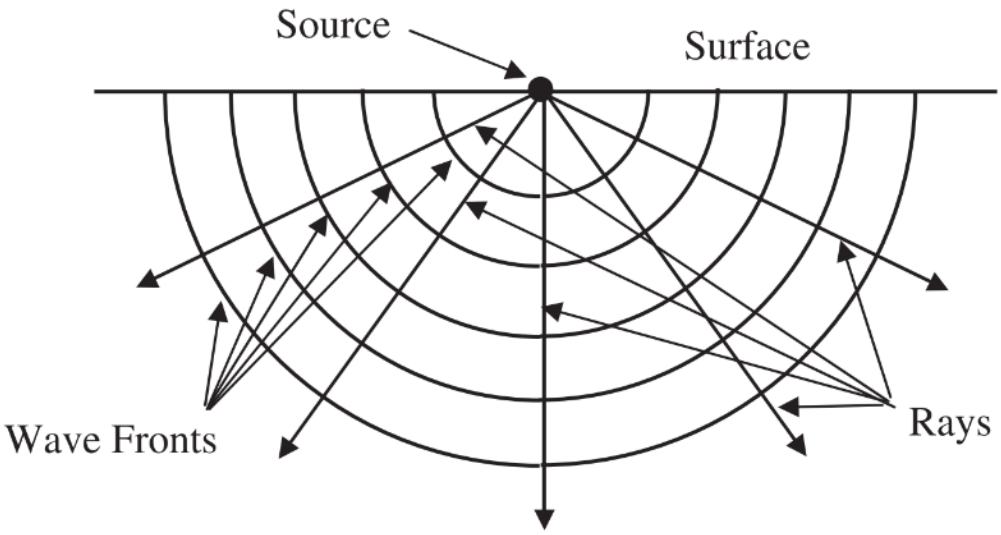

Figure 4.1: Wavefronts and rays in isotropic media. From Gadallah and Fisher. (2009).

Seismic waves can be classified into body waves and surface waves. Body waves can propagate through the subsurface, while surface waves can only propagate along the interface between two media. Body waves are further classified into Primary waves (also known as P-waves, compressional waves, or longitudinal waves) and Secondary waves (also known as S-waves, shear waves, or transverse waves).

Particle motion within the medium in which P-waves propagate are in the same direction as the wave motion, while for S-waves, particle motion is perpendicular to the direction of wave motion. P-waves travel faster than S-waves and can propagate in solids, liquids, and gasses while S-waves can only propagate in solids.

Surface waves are classified into Rayleigh waves and Love waves. When Rayleigh waves propagate through a medium, the particle motion is elliptical in a vertical plane relative to the surface (Gelius and Johansen, 2010). However, for Love waves, particle motion is akin to S-waves, but the motion is only parallel to the surface.

Body waves are mostly used in seismic exploration and will constitute the main type of waves discussed in this thesis.

4.2.1 Huygens' principle

Seismic modelling by ray-based methods is made efficient by Huygens' principle. The principle states that each point on the wavefront at a given instant of time can be seen as secondary point sources which emit a spherical secondary wave that are in phase with the original wavefront and propagates outward with the same velocity. The secondary waves constructively interfere, and their envelope creates a new wavefront, and in the same way, the envelope of the secondary waves from this newly created wavefront produces another wavefront (Robinson and Clark, 2017). Figure 4.2 shows a simple illustration of Huygens' principle. In a homogenous media, spherical wavefronts will remain spherical and plane wavefronts will remain plane (Gelius and Johansen, 2010). Huygens' principle is crucial for understanding and determining relative positions of wavefronts as they propagate through the subsurface.

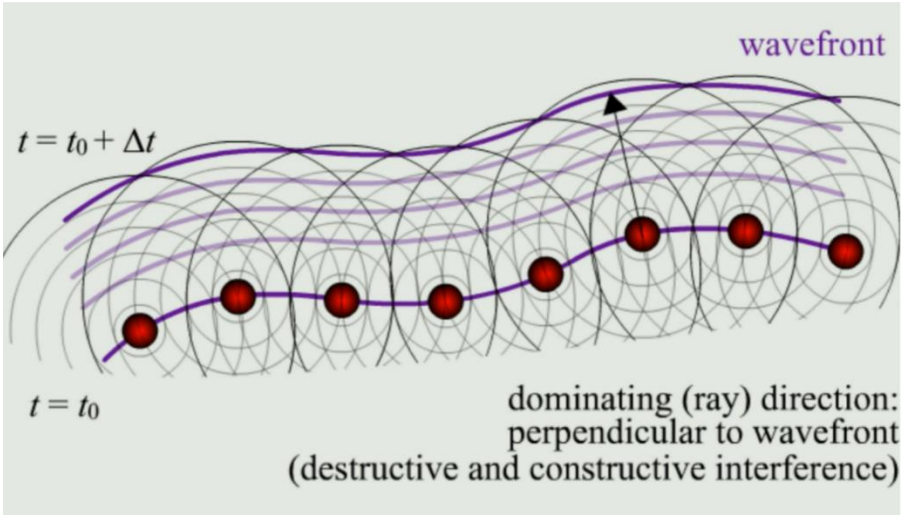

Figure 4.2: Envelope of secondary waves forming a new wavefront. The red circles represent unit points on the original wavefront. From Gelius and Johansen. (2010).

Long-established seismic modelling methods of computing wavefronts without using rays are based on the local application of Huygens' principle (Cerveny, 2001), for example the integral-equation modelling methods which are based on integral representations of the

wavefield as waves, originating from point sources (Carcione et al., 2002). Nevertheless, wave propagation is best simplified and analyzed as rays. This is possible because the constant-phase wavefronts can simply be represented by rays which are normal to the wavefronts (in isotropic media) and the wavefront motion can be followed by moving along the directions of the rays (Robinson and Clark, 2017). But even if rays are not normal to the wavefronts (in anisotropic media), slowness vectors are, hence the same principle of secondary point sources holds.

4.2.2 Snell's law

The principle that governs how raypaths bend across boundaries between two isotropic media is known as Snell's law. The law states that the ratio of the sine of incident angle (θ_1) and the medium velocity (V_1) in which the wave is propagating is equal to the ratio of the sine of the refraction angle (θ_2) and the contrasting medium velocity (V_2) in which the refraction occurred (Figure 4.3).

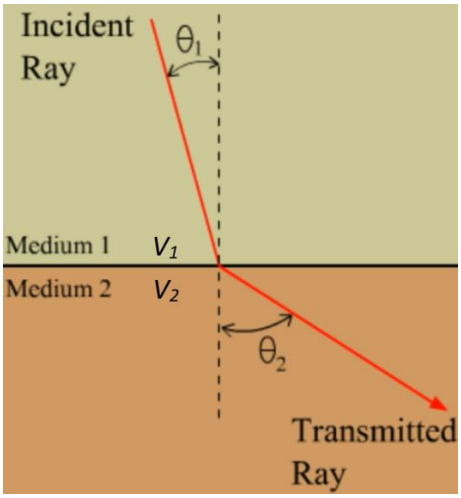

Figure 4.3: An incident ray propagating from a low velocity medium (medium 1) into a higher velocity medium (medium 2). As the incident ray is transmitted into the higher velocity medium, it bends towards the boundary separating the two media. Modified from Gelius and Johansen (2010).

The mathematical expression of Snell's law is represented in equation (4.1 and it is applicable to both P-waves and S-waves (Gelius and Johansen, 2010):

$$\frac{Sin\ \theta_1}{V_1} = \frac{Sin\ \theta_2}{V_2} = p, \tag{4.1}$$

where p is the so-called ray parameter. The value of $p = (Sin\ \theta) / V$ at an interface between two elastic media is the same for incident, reflected and refracted waves (Sheriff and Geldart, 1995). Snell's law also applies to P-wave to S-wave conversion (and vice versa) upon reflection or refraction (Sheriff and Geldart, 1995).

Basically, when an incident wave from a lower velocity medium propagates into a medium with higher velocity, the wave refracts or changes direction and propagates closer towards the interface separating the two media. The higher the incident angle, the closer the refracted wave bends towards the interface. When the refracted wave bends to the extent where the angle of refraction is 90°, the angle of incidence at which that refracted wave is generated is known as the critical angle (θ_c). Figure 4.4 shows the refracted raypath for an incident ray which has reached the θ_c. The refracted wave propagates as head waves along the interface separating the two media, but within the higher velocity medium. As the head wave propagates along the interface, considerable amount of energy escapes into the overlying lower velocity medium at the same θ_c (Figure 4.5). This phenomenon is behind the basic principle in seismic refraction surveys where the escaping energy is recorded by surface geophones (Robinson and Clark, 2017).

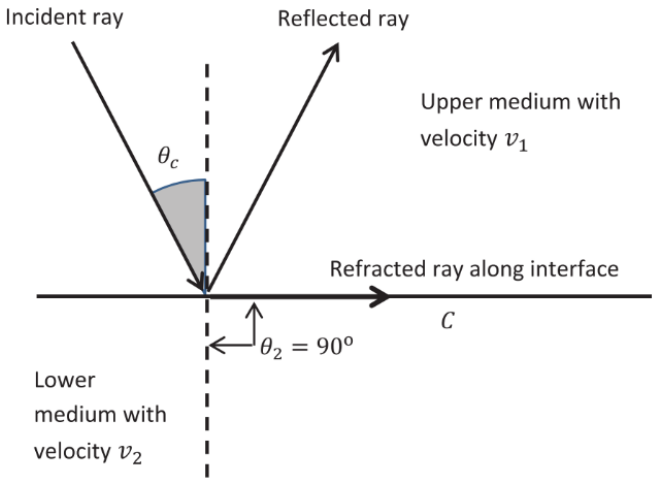

Figure 4.4: Critical angle. From Robinson and Clark, (2017).

θ_c can be calculated using Snell's law as represented in equation (4.2 (Gelius and Johansen, 2010):

$$\frac{Sin\ \theta_c}{V_1} = \frac{Sin\ 90°}{V_2} \Rightarrow Sin\ \theta_c = \frac{V_1}{V_2}\ . \qquad (4.2)$$

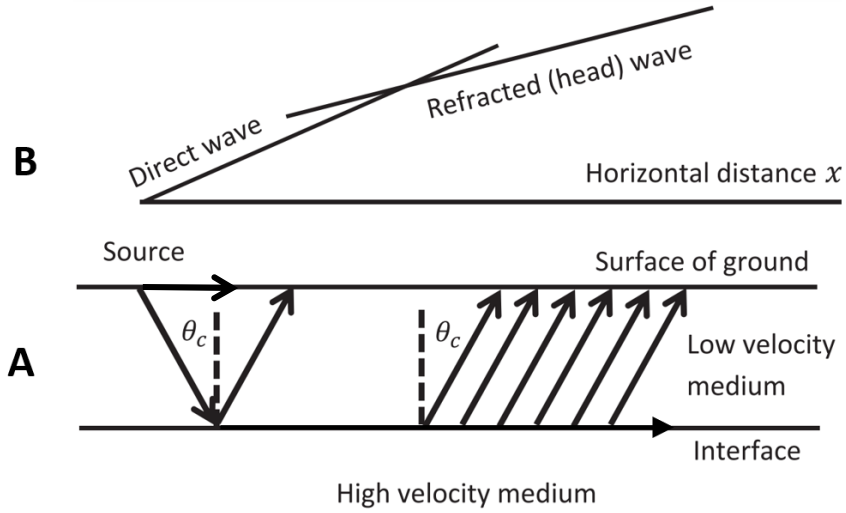

Figure 4.5: Critical angle and head wave in refraction seismic survey (A). The moveout of direct and refracted arrivals in seismic data (B). Modified from Robinson and Clark (2017).

When the incident wave angle exceeds the θ_c, Snell's law is no longer satisfied and there will be no transmission at the interface separating the two media, hence the total wave energy is reflected; this is known as total reflection.

When a propagating wave encounters a curved interface with radius of curvature less than a few wavelengths, or where the reflecting interface is terminated by a fault, pinchout, unconformity, etc, Snell's law will no longer be applicable because the energy is diffracted rather than reflected or refracted (Sheriff and Geldart, 1995). Figure 4.6 shows a simple illustration of diffraction. In seismic data, diffracted waves are characterized by distinctive curved alignments (Gelius and Johansen, 2010).

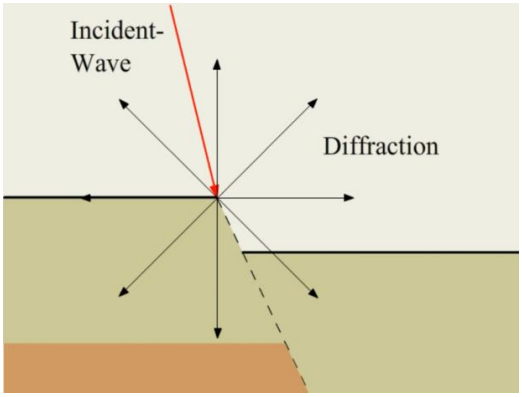

Figure 4.6: Diffracted waves from the termination of an interface due to a fault. From Gelius and Johansen (2010).

4.2.3 Normal- and oblique-incidence waves in layered isotropic media

When an incident elastic wave hits an interface between two media with different velocities of wave propagation, the energy is partly reflected and transmitted (Gadallah and Fisher, 2009). The amount of energy (amplitude) that is reflected and transmitted depends on the media velocities (V) and densities (ρ), and angle of the incident wave (Gelius and Johansen, 2010). The total sum of the reflected and transmitted energy is equal to the incident energy. This principle is valid for either P-waves or S-waves.

If we consider only a propagating P-wave that is incident at right angle (normal) to an interface between two media with different velocities, only P-waves are reflected and transmitted and their raypaths are also at right angle to the interface (Gadallah and Fisher, 2009), see Figure 4.7. The amount of energy that is reflected and transmitted in this case is determined by the contrast in a property known as acoustic impedance (Z) between the two media. Z is the product of seismic velocity (V) and density (ρ), and in reflection seismic, it is the rapid change in Z that is represented as reflectors (interfaces or boundaries) and not necessarily changes in lithology. The reflection coefficient (R), which is the ratio of the reflected wave energy and incident wave energy (Gelius and Johansen, 2010) is given by:

$$R = \frac{A_1}{A_0} = \frac{\rho_2 V_2 - \rho_1 V_1}{\rho_2 V_2 + \rho_1 V_1} = \frac{Z_2 - Z_1}{Z_2 + Z_1}, \tag{4.3}$$

where A_0 and A_1 are the amplitudes of the incident and reflected waves, respectively. R is positive when the wave propagates from a lower to higher Z medium. On the other hand, a

negative *R* is indicative of wave propagating from a higher to lower *Z* medium and the corresponding reflection is represented by a 180° phase change, meaning a sign change.

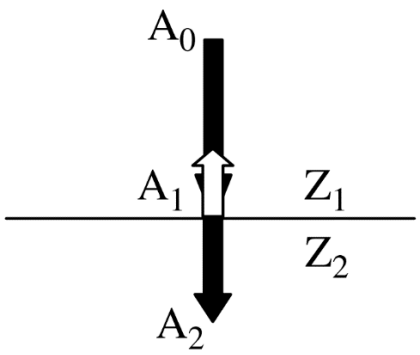

Figure 4.7: Reflection and transmission raypaths for a normal incident P-wave. From Gadallah and Fisher (2009).

The transmission coefficient (*T*) can be defined as the ratio of the transmitted wave energy to the incident wave energy (Gadallah and Fisher, 2009):

$$T = \frac{A_2}{A_0} = 1 - R\,, \tag{4.4}$$

where A_2 is the amplitude of the transmitted wave.

If a propagating P-wave is incident on an interface between two media at an oblique angle (except θ_c), four new waves may be generated (Figure 4.8). Unlike the normal incident setting, transmitted and reflected S-waves are also generated in addition to transmitted and reflected P-waves. The S-waves are known as shear-vertical waves (SV waves) because they are polarized in the vertical plane (Gadallah and Fisher, 2009). However, this assertion assumes a local 2-D model (Gelius and Johansen, 2010), in which case the particle motion is in the vertical plane of propagation. The reflection and transmission coefficients in this case are rather complex, and the mathematical relations to solve for these coefficients as a function of incident angle is given by the Zoeppritz' equations (Zoeppritz, 1919).

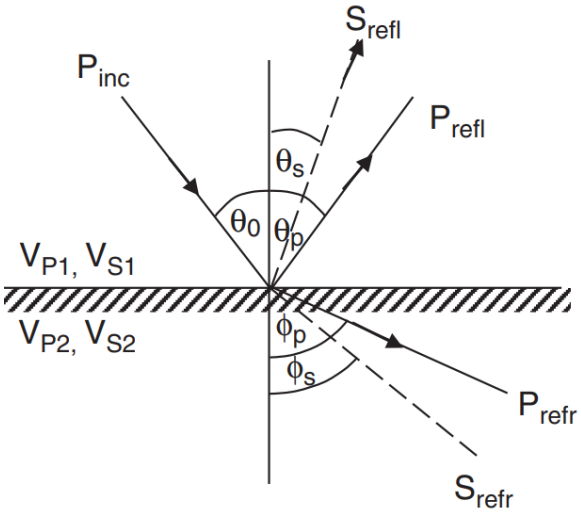

Figure 4.8: Reflection and transmission (refraction) for an oblique incident P-wave at an interface between two elastic media. From Gadallah and Fisher (2009).

4.2.4 Illumination

Illumination and resolution effects are key constraints which can limit the use of seismic waves for subsurface imaging.

Illumination can simply be described as the ability or extent to which a target is mapped. Overburden conditions in the subsurface (e.g., dipping reflectors and varying topography), elastic properties (e.g., lens structure such as a salt body with elastic property significantly different from surrounding properties), target geometry (e.g., flat, folded, dipping, or faulted layer) and the survey (e.g., source – receiver placements and acquisition direction) can affect illumination of subsurface targets (see Gjøystdal et al., 2002; Lecomte, 2006; 2008). Figure 4.9 shows an example of how overburden structure and velocity can influence illumination of a target.

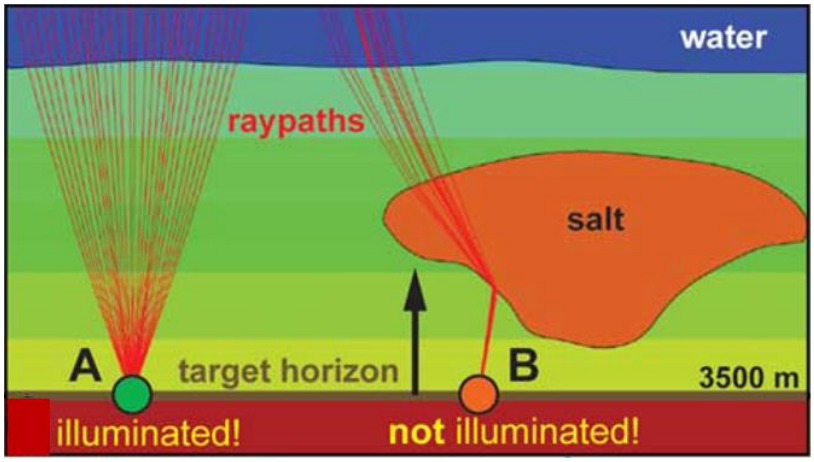

Figure 4.9: Overburden effects on wave propagation. Target point A is illuminated, while illumination of target point B is hindered by the overlying salt body. Modified from Lecomte (2008).

Energy reflected from a folded interface will focus or defocus the energy, depending on the curvature (Robinson and Clark, 2017). An illustration of how the geometry of a reflector can influence its illumination is represented in Figure 4.10. Basically, a synclinal interface will concentrate the reflected energy, thereby causing an increase in amplitude of the reflection, whereas an anticlinal interface will spread the reflected energy outwards, hence causing a decrease in amplitude.

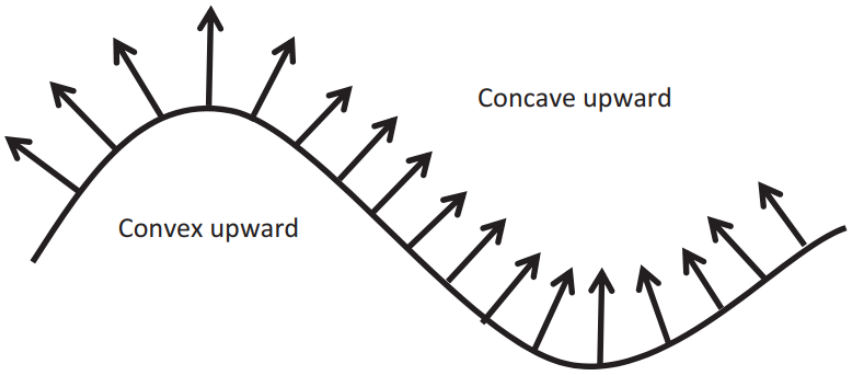

Figure 4.10: Reflected raypaths from anticlinal (convex upward) and synclinal (concave upward) interface. From Robinson and Clark (2017).

In seismic data, illumination effects could be present in the form of weak reflection energy (low amplitude), amplitude variation, shadow zones (no reflections), or poor / irregular reflection coverage.

A 2-D model experiment which studied and compared the relationship between RT-based illumination / amplitude maps with amplitudes observed in pre-stack depth migrated (PSDM) data is presented in Gjøystdal et al., (2002). Results from the study showed that the variation observed in the PSDM amplitude is comparable to the modelled illumination amplitude. Hence, seismic modelling can be beneficial during pre-survey feasibility studies and/or interpretation of data after PSDM by looking at typical modelled illumination attributes like integrated amplitude (amplitude density) and reflection point density (Gjøystdal et al., 2002), including other parameters. Figure 4.11 shows an example of how survey geometry can influence illumination.

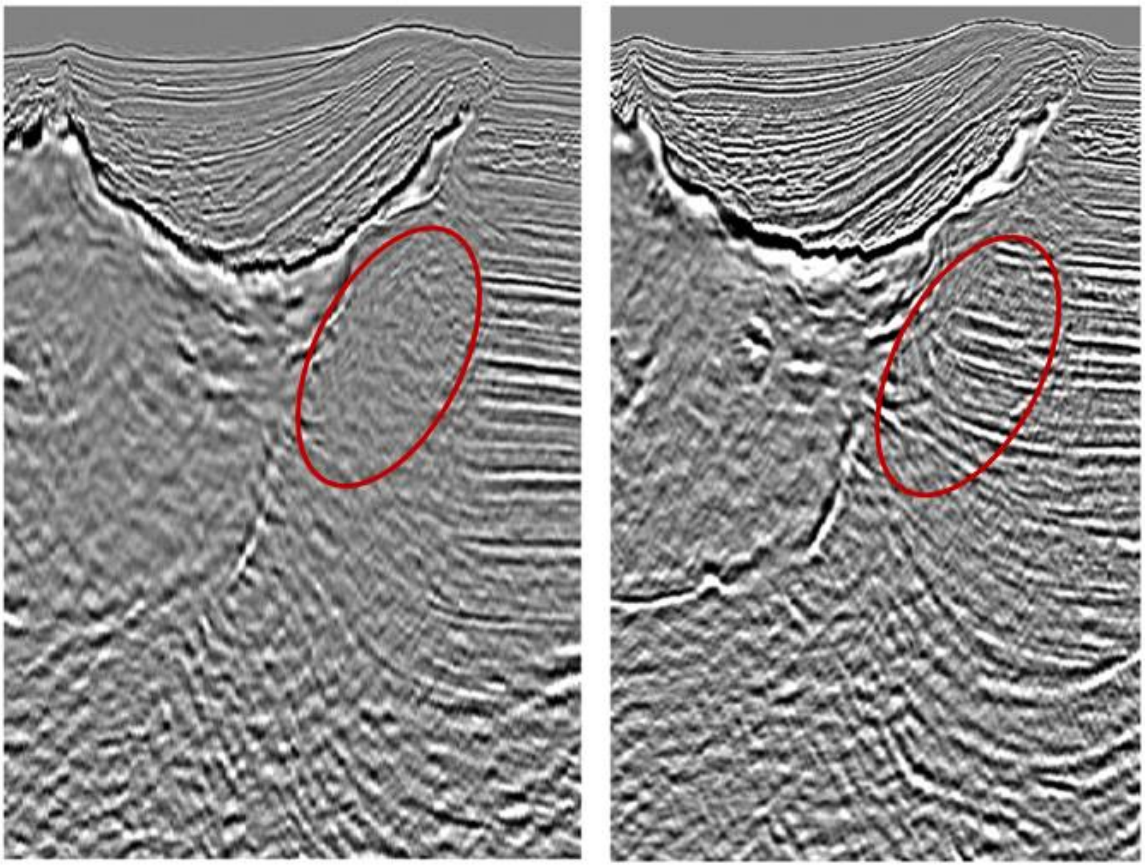

Figure 4.11: Comparison between seismic images acquired with conventional narrow-azimuth (NAZ) survey geometry (left) and wide-azimuth (WAZ) towed-streamer survey geometry (right). The shadow zone (highlighted area) which was not illuminated in the NAZ survey was illuminated in the WAZ survey. Modified from Moldoveanu (2008).

4.2.5 Resolution

Resolution refers to how close two points or features can be, yet still be distinguished as two points or features instead of one (Yilmaz, 1987; Sheriff and Geldart, 1995). In seismic methods, how far apart either in space or time two interfaces must be to be observed as separate reflectors is termed vertical resolution, and on the other hand, how far apart two distinct features on a single interface must be separated to be observed as separate features is known as lateral resolution (Sheriff and Geldart, 1995).

Lateral resolution is determined by the Fresnel zone. This zone can simply be described as the area of constructive reflection accumulation surrounding the specular-reflection point (i.e., where Snell's law is satisfied) (Lindsey, 1989). In practical terms, it is the area on an interface from which the reflected energy can reach the receiver within a time range that is less than half a period (or wavelength) of the first reflected energy arrival (i.e., the specular-reflected ray as defined by Snell's law). Hence, reflections that are considered as almost arriving at the same time at the receiver can be ascribed to reflections coming from a region known as Fresnel zone (Gelius and Johansen, 2010).

Given a flat interface and a zero-offset source – receiver position, the Fresnel zone for reflections arriving from the flat interface will be circular (Gelius and Johansen, 2010) as represented in Figure 4.12, with the Fresnel zone radius (R_f) represented mathematically as:

$$R_f = \sqrt{\frac{\lambda Z}{2}} = \sqrt{\frac{VZ}{2f_c}}, \tag{4.5}$$

where λ is the dominant wavelength which is given by $\lambda \approx V/f_c$, V is the wave velocity, f_c is the centre frequency of the pulse (most energetic part), and Z is the distance from the source / receiver point to the specular-reflection point.

Generally, the longer the wavelength, the lower the resolution. Hence it follows that velocity and frequency can affect lateral resolution given their mathematical relationship with wavelength. Basically, high velocity implies long wavelength which will result in lower resolution. On the other hand, high frequency implies short wavelength and therefore higher resolution.

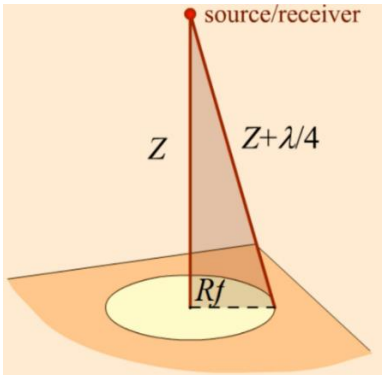

Figure 4.12: Fresnel zone radius on a flat reflecting interface, given a zero-offset source-receiver position. R_f is the Fresnel zone radius, Z is the distance from the source-receiver point to the specular-reflection point, and λ is the dominant wavelength. From Gelius and Johansen (2010).

Without sufficient vertical resolution, thin beds or small wedges and pitchouts cannot be detected (Robinson and Clark, 2017). Vertical spacing between interfaces must be more than one-quarter of the dominant wavelength to be identified as separate events. In other words, if the spacing between the two interfaces (or thickness of the bed) is less than one-quarter of the dominant wavelength, the bounding interfaces may be identified as a single event instead of two separate events. This is known as the tuning thickness (Gelius and Johansen, 2010). For beds or interface spacings that are less than the tuning thickness (i.e., *λ/4*), an interference effect will occur, which may lead to either generation of one reflection event with a high amplitude (constructive interference), or one with significantly low or zero amplitude (destructive interference).

Generally, high frequency and short wavelengths will give better resolution in both vertical and lateral directions. Resolution also depends on the data quality and the ability of the interpreter to distinguish between features, especially where the differences are subtle (Sheriff and Geldart, 1995).

4.2.6 Seismic energy loss

Seismic waves loose energy as it propagates through the subsurface. This loss of energy is represented by a reduction in amplitude which typically decreases with distance from the source. Seismic amplitude can be described as the magnitude of the wiggles of seismic records and quantifies the energy level of seismic waves (Zhou, 2014). There are several

factors which causes reduction of seismic amplitude, but the main factors which are related to the media in which the waves propagate are: geometrical (spherical) spreading, intrinsic attenuation (absorption) and extrinsic attenuation (scattering).

Geometrical spreading is the loss of seismic energy due to spherical divergence of the waves as it propagates through the subsurface. As the waves diverge or spread with distance from the source, the wave energy per unit area reduces, and since seismic amplitudes are proportional to the square root of energy per unit area (energy density), the amplitudes become smaller even at a greater rate than the reduction in energy per unit area (Gadallah and Fisher, 2009). Given a homogenous medium, the geometrical spreading of a line source will be cylindrical and inversely proportional to the square root of the distance from the source; for a point source, the geometrical spreading will be spherical and inversely proportional to the distance from the source (Zhou, 2014).

Seismic attenuation is the loss of frequency content in a seismic data due to intrinsic (absorption) and extrinsic (scattering) effects. Intrinsic attenuation occurs due to anelasticity of the propagating medium, while extrinsic attenuation is due to scattering of energy because of lateral heterogeneities (Thirunavukarasu et al., 2016), for example, a faulted subsurface medium. Attenuation is described by the seismic quality factor (Q), which is the ratio of total energy in the seismic wave to the energy lost in one cycle (period) or each wavelength (Zhou, 2014; Thirunavukarasu et al., 2016). The higher frequencies in the wavelet are attenuated more than the lower frequencies, hence the deeper the reflection arrival, the lower the frequency content and resolution (Yilmaz, 1987; Gelius and Johansen, 2010). Q is especially sensitive to rock type. The smaller the Q value, the higher the energy loss and vice-versa, thus Q is the inverse of attenuation (Pujol, 2003; Costain and Coruh, 2004; Gelius and Johansen, 2010). Essentially, Q is a combination of intrinsic (Q_i) and extrinsic (Q_{sc}) attenuation (Thirunavukarasu et al., 2016):

$$Q^{-1} = {Q_i}^{-1} + {Q_{sc}}^{-1} \tag{4.6}$$

4.3 Seismic modelling methods

There are several seismic modelling methods (Carcione et al., 2002). The most basic method is the 1-D convolutional trace model. The method is illustrated in Figure 4.13. It is based on the assumption of a horizontally layered earth, normal incident plane waves, stationary source pulse, and zero-noise contribution (Gelius and Johansen, 2010). The seismic trace *x(t)* is then

simply described as a linear convolution between the source pulse *s(t)* and the Earth's reflectivity series *r(t)*:

$$x(t) = s(t) * r(t) \tag{4.7}$$

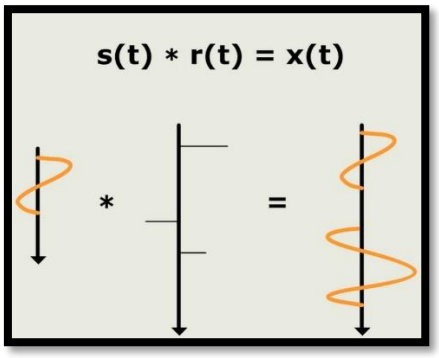

Figure 4.13: Convolutional trace model. From Gelius and Johansen (2010).

This method is still extensively used in many applications, especially for computing synthetic seismograms from well logs for well-to-seismic tie. However, the results are unreliable in complex sub-surface geometries where lateral velocity variations and illumination issues occur (Lecomte et al., 2015).

Over the years, seismic modelling methods have evolved from 1-D convolution to 3-D elastic wave equation representation of the total wavefield, and some assumptions are often used by the different methods to make the complexities associated with seismic wave propagation through the subsurface easy to deal with (Sayers and Chopra, 2009). Seismic modelling is categorized into three methods: direct methods (e.g., FD), integral-equation methods, and RT (or asymptotic) methods (Carcione et al., 2002). Emphasis is given to FD and RT methods which are the methods applied in this thesis. Integral-equation methods are based on Huygens' principle where waves are used as integral representation of the wavefield originating from point sources (Carcione et al., 2002).

Each seismic modelling method has its merits and drawbacks and no method is superior to another. Moreover, it is not a 'one-size-fits-all', rather it is about finding the right method or a combination of methods that is suitable for a particular seismic modelling objective (Gjøystdal et al., 2002).

The methods are unique in the sense that each of them represents a solution obtained by solving the wave equation in a different way. Basically, seismic modelling aims to solve the equation of motion for seismic waves using the wave equation which originates from Hooke's law (normal stress = normal strain) and Newton's second law of motion (force = mass x acceleration), for particle motion in a solid medium as elastic waves propagate through it (Krebes, 2004; Gelius and Johansen, 2010).

The elastic wave equation is a partial differential equation which describes the micro-scale changes in particle displacement in time and space within an elastic medium as waves propagate through the medium (Gelius and Johansen, 2010): for a homogenous and general elastic medium, the equation is given by

$$\rho \frac{\partial^2 u_i}{\partial t^2} - c_{ijkl} \frac{\partial^2 u_l}{\partial x_j \partial x_k} = 0 , \tag{4.8}$$

where ρ is density, $\boldsymbol{u}(\boldsymbol{r},t)$ is the particle displacement at position $\boldsymbol{r}=(x,y,z)$ and time t, and c_{ijkl} are the components of the fourth-order elastic stiffness tensor which describes the elastic properties of the medium.

The wave equation for the pressure p in an acoustic medium (a medium with no shear strength so that no S-waves can exist) can be written in scalar form (Robinson and Clark, 2017):

$$V^2 \nabla^2 p = \frac{\partial^2 p}{\partial t^2}, \tag{4.9}$$

where V is the wave velocity, and ∇ is the vector differential operator (del) whose coefficients in Cartesian coordinate system can be written as:

$$\nabla = \left(\frac{\partial}{\partial x}, \frac{\partial}{\partial y}, \frac{\partial}{\partial z}\right), hence \quad \nabla^2 = \frac{\partial^2}{\partial x^2} + \frac{\partial^2}{\partial y^2} + \frac{\partial^2}{\partial z^2} , \tag{4.10}$$

where ∇^2 is termed Laplacian operator.

4.3.1 RT modelling method

RT modelling method is a high-frequency approximation of the elastic wave equation (Cerveny, 1985; Gjøystdal et al., 2002; 2007). When the elastic wave equation is solved with a high-frequency approximation, it yields two separate equations: the eikonal equation which gives the traveltimes and rays, and the transport equation which gives the amplitudes (Cerveny, 2001; Gjøystdal et al., 2002).

Solving the wave equation with a high-frequency approximation implies that the medium parameters (interfaces and properties) must be sufficiently smooth and not change very much within the size of the dominant seismic wavelength (Krebes, 2004). In other words, the RT results are only valid for wavelengths significantly smaller than any physical scale used in the model (Gjøystdal et al., 2002), see Figure 4.14.

The eikonal equation is a non-linear partial differential equation of the first order (Cerveny, 2001). If the condition for high-frequency is fulfilled, the traveltime $t(\boldsymbol{r})$ of a wave from a source to a point $\boldsymbol{r} = (x, y, z)$ in a heterogenous isotropic medium obeys the eikonal equation (4.11), which is obtained by substituting a trial solution for $\boldsymbol{u}$ into the wave equation and making the necessary high-frequency approximations (Cerveny, 2001; Carcione et. al., 2002; Krebes, 2004):

$$(\nabla \mathrm{t})^2 = \left(\frac{dt}{dx}\right)^2 + \left(\frac{dt}{dy}\right)^2 + \left(\frac{dt}{dz}\right)^2 = \frac{1}{V^2}\,, \tag{4.11}$$

where $V = V(\boldsymbol{r})$ is either P or S wave velocity at a given point $\boldsymbol{r}$.

In the high-frequency approximation, the amplitude of the rays can also be computed by solving the transport equation (4.12) for the wave (Cerveny, 2001; Carcione et al., 2002; Krebes, 2004). For instance, if an acoustic wave is considered, the transport equation for the amplitude $A(\boldsymbol{r})$ of the pressure wave at a given point $\boldsymbol{r}$ can be computed once the travel time (t) is known by solving the eikonal equation (4.11) (Krebes, 2004):

$$2\nabla A \cdot \nabla t + A\nabla^2 t = 0\,. \tag{4.12}$$

The RT method is divided into kinematic and dynamic RT. Kinematic RT computes the using the eikonal equation (4.11), while dynamic RT computes the geometrical spreading factors and amplitude coefficients along the rays using the transport equation (4.12) (Cerveny, 1985; Gjøystdal et al., 2002). Kinematic RT is dependent only on the seismic velocity of the subsurface model while dynamic ray tracing is dependent on both velocity and density of the subsurface model (Alaei, 2012).

In the RT method, reflection and transmission of rays at velocity contrasts is governed by Snell's law (4.1). The method is very efficient for calculating traveltimes, hence they are widely used for generating synthetic seismograms, tomographic inversion, and migration (Carcione et al., 2002). Surface waves and head waves are not modelled in the RT methods, but diffractions can be simulated approximately (Gjøystdal et al., 2002).

Only traveltimes and amplitudes from RT were used in this thesis. However, synthetic seismograms are usually computed using the information derived from dynamic RT by convolving RT results with a specified wavelet (Gjøystdal et al., 2002).

4.3.1.1 Model parameters

Two main model parameters are required to perform RT modelling: an interface which describes the *Impedance constrast* between two different layers in the subsurface, and elastic properties (e.g., P-wave and S-wave velocities, density; optionally Q-factors, and anisotropy parameters) which represent bulk material properties within the layers defined in the model (Gjøystdal et al., 2002). Figure 4.14 shows an example of a simple model showing the medium parameters.

The threshold for the interface smoothness is defined by the curvature radius of the interface, and to ensure that the interface is smooth enough, the minimum curvature radius of the interfaces should be larger than the dominant wavelength in the seismic signal (Alaei, 2012).

To perform RT, a user-defined ray code which determines the wave type and how the waves are to be transmitted/reflected at interfaces is required (Gjøystdal et al., 2002).

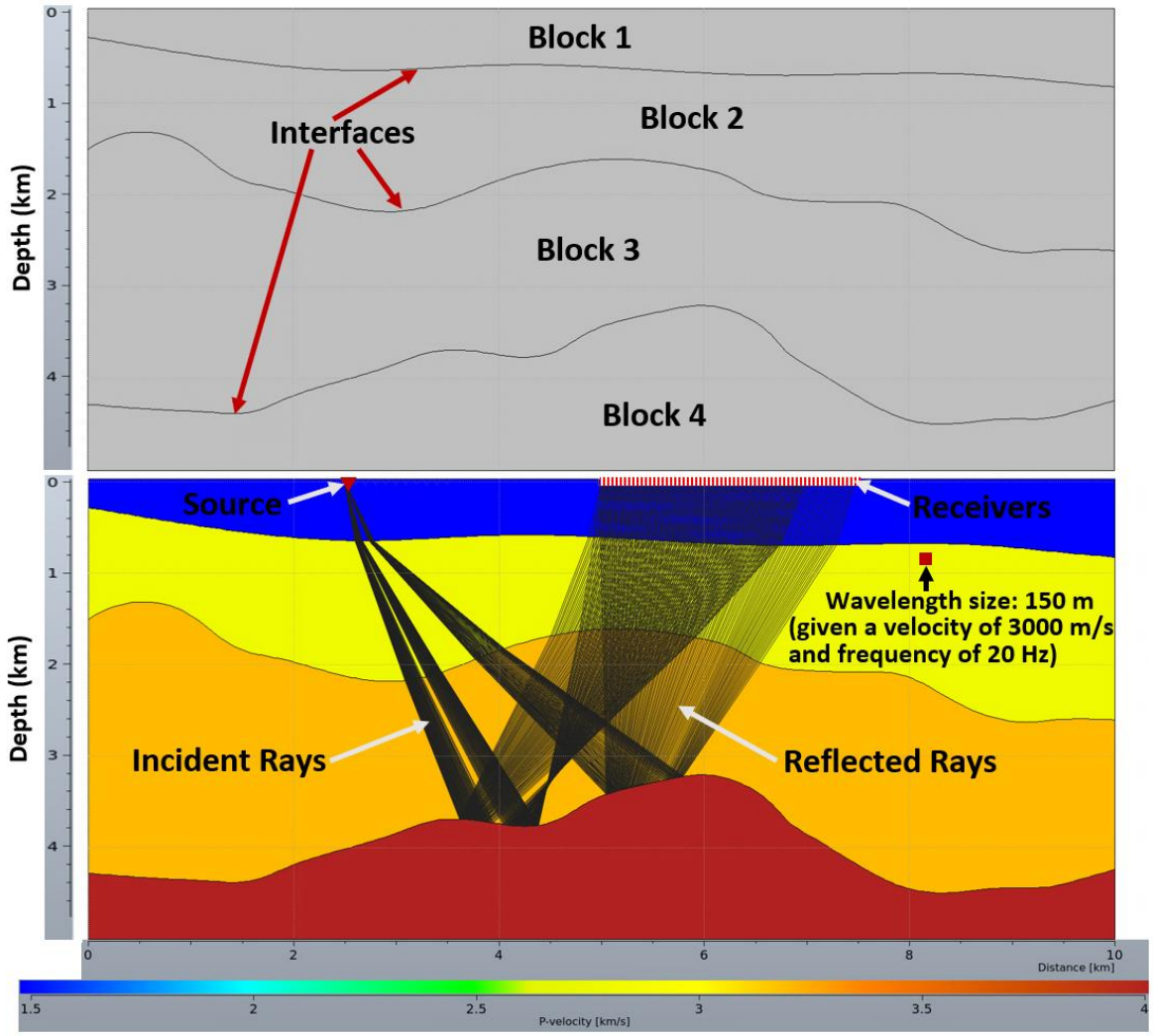

Figure 4.14: A simple illustration of a model with three interfaces and four layers represented as blocks (top), and complete model with P-wave velocity assigned to the blocks (bottom), including raypaths from a single shot to multiple receivers (specified ray code is primary P-wave reflection from the deepest interface). Here the model parameters (for example, the P-wave velocity variation) is smooth enough, relative to the size of the wavelength.

4.3.1.2 Paraxial ray method (PRM)

According to Cerveny (1985), for laterally heterogenous subsurface models with curved interfaces, there are three RT approaches that can be utilized: the standard-RT method, PRM, and the Gaussian-beam method. The approach used for the RT modelling in the present work is the PRM, hence PRM is mostly discussed here. The model and simulations were restricted to 2-D.

Paraxial rays can be described as rays whose path do not deviate from a given geometrical ray as it propagates between two points in a certain area of the subsurface model (Krebes, 2004).

The PRM was developed in response to the computational challenge associated with performing RT using the standard-RT method (Gjøystdal et al., 2002). The standard-RT method is computationally inefficient because the traveltime and displacement vector of the waves are computed only along rays, hence, to evaluate the wavefield at any given point, the ray which passes exactly through that point must be found (Cerveny, 2001). This standard-RT method utilizes a two-point RT technique in which attempts are made to find all rays connecting a specified source and receiver location using either shooting or bending algorithms (Cerveny, 1985; 2001; Gjøystdal et al., 2002). In contrast, the PRM is more computationally efficient and can compute the traveltime and displacement vector of the waves not only along the ray, but also within its vicinity (Cerveny, 2001).

Generally, in complex subsurface models, tracing a ray between defined source – receiver locations is mostly done by the shooting method, where the angle at which the ray departs the source location (take-off angle) is determined iteratively through trial and error (Krebes, 2004). This shooting algorithm is behind the PRM used in the present work. Basically, in the PRM, a fan of rays covering a wide range of ray directions is shot and traced from the source location, and then using the local wavefront curvature and spreading information derived from dynamic RT, the wavefield is extrapolated away from the ray to neighbouring receivers, such that two-point ray tracing is not required (Cerveny, 1985; Beydoun and Keho, 1987; Gjøystdal et al., 2002). In other words, the extrapolation is achieved by extrapolating the succeeding ray from the spreading information (spreading factor) obtained from the preceding ray.

The following should be noted about the PRM (see Beydoun and Keho, 1987):

- The spatial limit between extrapolations is important, i.e., how far away from the ray the extrapolation should be considered valid must be defined. This is because the accuracy of the RT result is improved when the density of the fan of rays is increased; however, it comes at the cost of increased computation time.
- It is more accurate for computing traveltimes, but less accurate for determining amplitudes.
- In comparison to the standard RT method, it is faster for computing traveltimes and amplitudes, given a dense grid of receivers.

4.3.1.3 Benefits and drawbacks of RT methods

There are several benefits in the RT methods, but the most valuable advantage of the method includes the flexibility to choose the type of waves (e.g., P-wave or converted S-wave) to be modelled, and the type of transmission or reflection (e.g, primaries or multiples) desired at interfaces between layers defined in the model (Lecomte et al., 2015). This provides the opportunity to analyze the contribution of various wave modes in seismic data. How the specific wave types are to be transmitted / reflected at interfaces are defined as ray codes (see Figure 4.14) specified by the user (Gjøystdal et al., 2002).

The RT results can be stored as event files, where attributes (e.g, traveltimes, incident angles, amplitudes, etc.) can be extracted; in addition, propagation effects (i.e., geometrical spreading factors, reflection / transmission effects, etc.) can also be directly extracted (Gjøystdal et al., 2002).

One of the main drawbacks of RT methods is the unreliable amplitudes in specific instances. This is mainly due to the high-frequency assumption which thus requires smoothing of the model parameters (interfaces and properties) to avoid amplitude issues, though this prevents considering geological details (Gjøystdal et al., 2007). Amplitudes are also erroneous in caustic zones where unrealistic high amplitudes are calculated, for example where rays from a single source converge (focus) due to changing velocity gradients (Krebes, 2004; Gjøystdal et al., 2007). In addition, at near-critical offsets (near-critical angle) where the transmitted P-wave or S-wave becomes evanescent and propagates along the interface, computed amplitudes are also inaccurate (Krebes, 2004).

4.3.2 FD modelling method

The FD modelling method is a numerical solution to the wave equation (Levander, 1989; Carcione et al., 2002; Moczo et al., 2004; Krebes, 2004). It is based on the direct discretization of the governing differential equations (Gjøystdal et al., 2002). The basic idea behind the FD method is to compute the particle displacement $\boldsymbol{u}\ (\boldsymbol{r}, t)$ at a discrete set of densely sampled grid points in the given model, by directly approximating the derivatives in the wave equation (4.8) with FD formulas (Krebes, 2004), and iteratively solving the resulting difference equation (i.e., from time step to time step). In simple terms, the method works by iteratively computing the particle displacement at any given point at a certain time in a subsurface model time step after time step.

In most FD methods, the model parameters (velocity and stress components) are distributed as conjugate physical quantities on staggered grids (Virieux, 1986; Moczo et al., 2004) in which each displacement (or particle velocity) component and each shear stress-tensor component has its own grid position (Moczo et al., 2004). In most applications, the temporal derivatives are approximated in second-order accuracy while the spatial derivatives are often approximated in a higher order accuracy, e.g., fourth-order (Dai et al., 2014).

The algorithm behind the FD method used in the present work is also based on model parameters populated on staggered grid with an automatically adjustable operator-length in space and second-order in time (cf. Mittet, 2002). The operator-length is computed automatically based on the resolution (very sparse to very dense) of the subsurface model grid.

Higher-order operators (higher-order derivative approximations) allow decrease in spatial sampling, thus enhancing efficiency in 2-D modelling (see Levander, 1989): given the same subsurface model, a fourth-order scheme needs approximately twice as many operations per node than the second-order scheme, but requires only about one-quarter as many nodes as required by the second-order scheme. Therefore, denser sampling will require more computational cost and time; hence most users choose the coarsest sampling rate that will produce a manageable level of artifacts (Zhou, 2014). However, the cost of choosing a coarser grid sampling is the prevention of models with finer level of details.

Time and spatial sampling of the subsurface model are constrained by the frequency content of the propagated signal and the velocity range; a general rule of thumb is that the higher the frequency and the lower the smallest velocity, the smaller the sampling, both in time and space (Lecomte et al., 2004).

Elastic FD modelling in 2-D was applied in the present work. Elastic FD modelling provides a more realistic simulation of wave propagation through a subsurface model because it supports the propagation of both P-waves and S-waves (Levander, 1989), unlike acoustic FD modelling which only considers P-waves, in which case amplitudes will not be reliable. However, acoustic FD modelling is less time-consuming than elastic FD modelling, hence it is often used where little or no concern is given to amplitude variations. Full elastic 3-D FD computations are very time-consuming and can take several hours if not days to run for realistic subsurface models, hence it is common practice to run the computations in 2-D which is comparably less time-consuming (Krebes, 2004).

It is important to note that in a 2-D FD simulation, the source will act as a line source rather than a point source as applicable in 3-D (and in actual cases), therefore the amplitude decay due to geometric spreading or spherical divergence in the case of a medium with constant velocity is $1/\sqrt{r}$ (where r is the distance along the rays between the source and receiver), whereas in 3-D domain, the source is a point source exhibiting their impulsive character as spherical waves (Levander, 1989); in which case the amplitude decay is $1/r$.

A major advantage of the FD methods is their ability to completely describe the wave motion in a subsurface model with any spatial variation of elastic properties (Levander, 1989), thus generating synthetic seismograms containing the full wavefield (reflections, refractions, etc.) with correct amplitudes and phases (Krebes, 2004), unlike RT methods in which a specific wave mode is generated at a time. In addition, because the wavefield is computed throughout the computational domain, the FD method also generates continuous movie (snapshots) of the wave propagation along with the synthetic seismogram of the full wavefield (Levander, 1989; Carcione et al., 2002; Mittet, 2002). These snapshots provide the only possibility to analyze the full wavefield in FD modelling contrary to RT methods where rays can be visualized for each modelled wave phase (Lecomte et al., 2004).

There are several sources of numerical errors which can introduce artifacts into the synthetic seismogram generated via FD methods. These errors can occur due to numerical dispersion (i.e., waves propagating with a frequency-dependent velocity due to the discrete grid), stability (errors growing exponentially), artificial reflections from the edge of the model due to inefficient absorbing boundary conditions, and inaccurate boundary conditions at the boundaries within the model (Bernth and Chapman, 2011). Because of these potential sources of error, certain conditions must be met to ensure that the FD computations are reliable. The conditions and concerns are discussed in the following subsections.

4.3.2.1 Stability and dispersion conditions

Numerical stability and accuracy of the FD computations are key issues in FD modelling; therefore, the computations are constrained by a stability condition and a dispersion condition (see Virieux, 1986; Levander, 1989). The numerical stability depends on the grid spacing, the time step, velocity, and the order (and type) of the operators. Dai et al., (2014) showed that temporal dispersion error causes phase rotation, which is related to the time spacing in addition to the frequency and the propagation time. The stability condition is represented in

equation (4.13), it ensures that the time step (Δt) is not too coarse in relation to the smallest grid spacing (Δh) (Gjøystdal et al., 2002):

$$\frac{V_{max}\Delta t}{\Delta h} \leq \alpha\,, \tag{4.13}$$

while the dispersion condition ensures that the shortest wavelength is not aliased as a result of the model being too sparsely sampled; i.e., it ensures that a minimum number of grid points per wavelength follows the expression in (4.14):

$$\frac{V_{min}}{f\Delta h} \leq N_{min}\,, \tag{4.14}$$

where V_{max} and V_{min} represent the highest velocity (typically P-wave velocity) and the lowest velocity (typically S-wave velocity), respectively, in the subsurface model, and f_{max} is the maximum frequency. The smallest wavelength occur for the minimum velocity and the maximum frequency. Generally, the accuracy of the FD computation is impaired by grid (or numerical) dispersion if the grid spacing is too coarse (Levander, 1989) and this can lead to introduction of artifacts to the calculated results. Numerical dispersion depends on the number of grid points per wavelength and the order of the operator. The errors associated with spatial differentiations can be made arbitrarily insignificant if the operator-length is chosen depending on the required number of nodes (grid points) per shortest wavelength (Mittet, 2002). For instance, in second-order FD schemes there is a rule of thumb stating that a minimum spatial sampling of 10 grid points / wavelength is required to minimize the effects of grid dispersion (Virieux, 1986; Levander, 1989; Krebes, 2004). In the FD modelling application used in the present work, model sampling in time is automatically checked and adjusted to ensure that the sampling is sufficiently fine (based on stability condition) to avoid temporal dispersion (see Mittet, 2002).

4.3.2.2 Boundary conditions

Boundary conditions of the subsurface model is also a very important issue in FD modelling. The spatial FD model grid is bounded by artificial boundaries (Moczo et al., 2004) from which artifacts can be introduced into the modelling results. Therefore, boundary conditions are required at the edges of the computational grid (Levander, 1989). Figure 4.15 shows an example of a 2-D Cartesian system for an FD formulation for a heterogenous media described in Levander (1989). The numerical scheme consists of an internal grid FD operator and numerical boundary conditions applied around the edges of the grid. Without application of these boundary conditions, the artificial boundaries can act as reflecting surfaces from which artificial reflections can be generated (Krebes, 2004) as shown in Figure 4.16.

The artificial reflections can be avoided by using either transparent boundary conditions (non-reflecting) or absorbing boundary conditions at the grid edges (Krebes, 2004; Moczo et al., 2004), or by a combination of the two types of boundary conditions (Mittet, 2002). Note that the artificial reflections may not be removed entirely, but it can be approximately suppressed (Krebes, 2004). A particular source of concern are waves incident on the artificial boundaries at grazing angles (large incident angles), leading to total reflection which generates backscattered noise regardless of any type of boundary condition applied (Mittet, 2002; Zhou, 2014). An example of a total reflection effect for large incident angles is represented in Figure 4.16 (middle).

There are several boundary condition techniques, but the technique used in this thesis is known as perfectly matched layer (PML). The technique was originally developed by Berenger (1994) for electromagnetic waves but have been adapted for use in seismic modelling using FD methods. The main idea behind this technique involves extending the artificial boundary edges, and then using a damping algorithm to absorb the waves incident upon the artificial boundary within the extended layer (Collino and Tsogka, 2001) (see Figure 4.17). PML is so far the best technique used to prevent artificial reflections (Moczo et al., 2004). It has the unique ability of generating a negligible R for all angles of incidence and all frequencies after discretization (Komatitsch and Tromp, 2003). Collino and Tsogka, (2001) presented results from experiments carried out on a heterogeneous anisotropic model with PML boundary conditions. The results showed that the R can be as low as about one percent for layer thickness (absorbing layer) measuring about five nodes of the discretization steps.

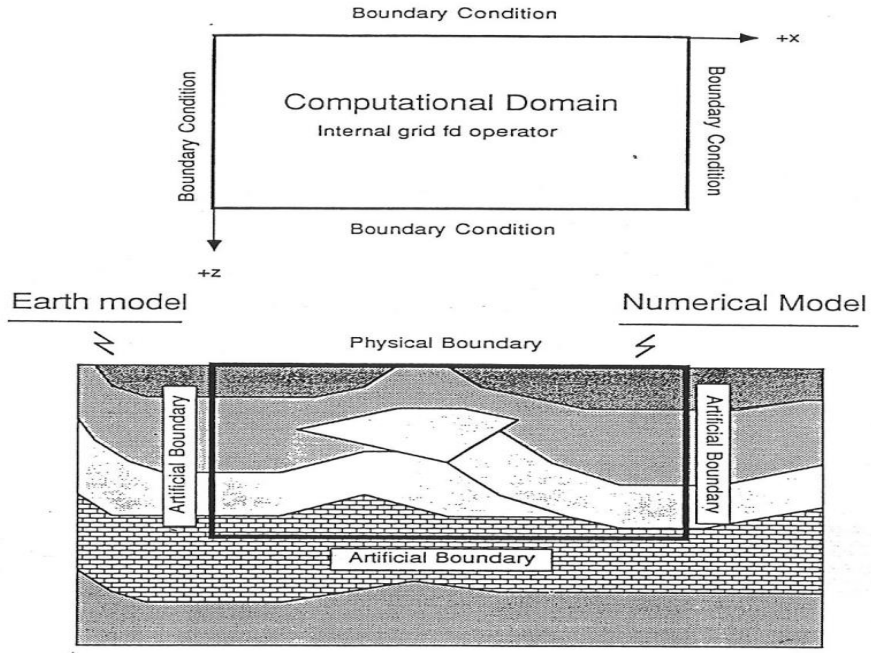

Figure 4.15: 2-D Cartesian system for an example FD scheme showing the internal grid FD operator and where numerical boundary conditions were applied. The numerical scheme is designed to simulate wave propagation in a heterogenous subsurface model and the boundary conditions at the edges may be physical or artificial conditions which are designed to make the computational domain appear infinite or plane layered outside the area of interest. From Levander, (1989).

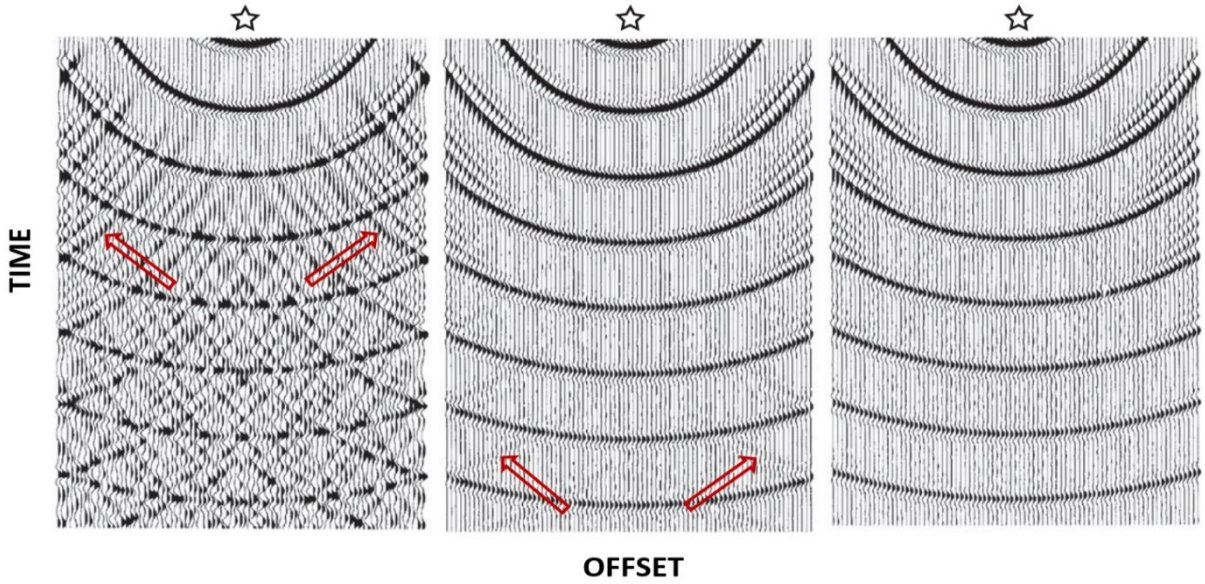

Figure 4.16: Cross-section of snapshots for three absorbing boundary conditions in an FD simulation of monochromatic waves from a point source (star). The edges of the model are perfect reflectors (left), absorbing reflections of high incident angles (middle) and using the right absorbing boundary condition. The red arrows are pointing to waves reflected from the edges of the model boundaries. Originally from Clayton and Engquist (1980). Modified from Zhou (2014).

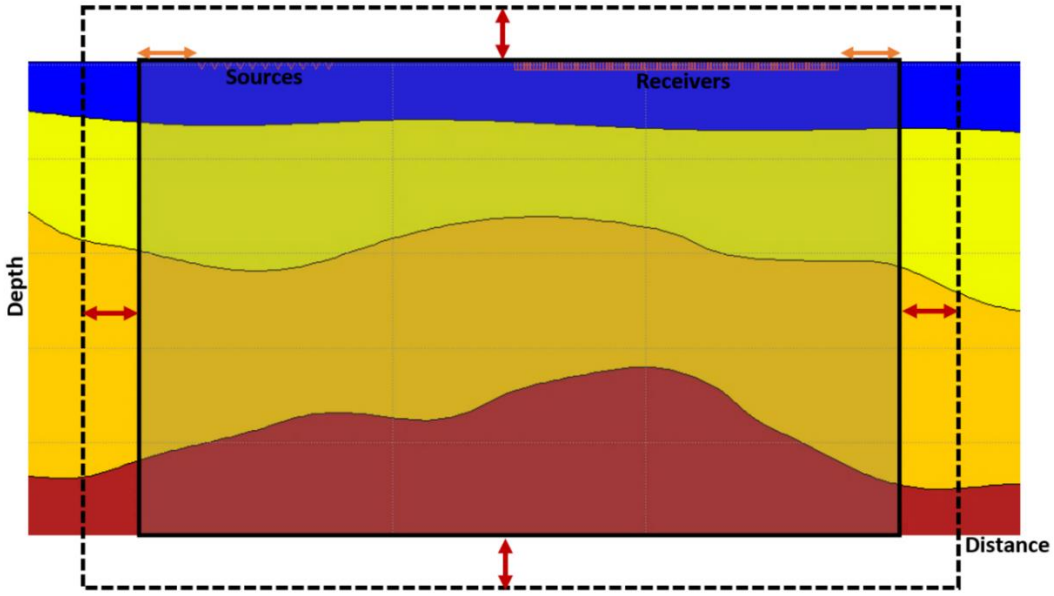

Figure 4.17: A Simple illustration of a subsurface model and absorbing layer. The black solid line highlights the model edges, the dashed line indicates the extended boundary region. The orange arrows represent the model buffer zone, and the red arrows represent the absorbing layer within which the waves are absorbed or attenuated.

4.3.2.3 Errors due to internal subsurface model grid

Consider a sufficiently smooth interface as typically used to represent *Impedance constrast* in the RT methods. In FD method, this smooth interface will be represented as a succession of grid cells (nodes) forming a step-like structure which may generate artificial diffractions, especially at the seafloor due to the high *Impedance constrast* between the water column and the seabed (Lecomte et al., 2004). In the FD modelling package used in the present work, this problem is solved by direct averaging of the medium properties, but with a condition that the averaged shear modulus is zero on a fluid/solid interface (see Mittet, 2002).

4.3.3 Comparison between RT and FD methods

RT and FD methods have their merits and drawbacks, and one method should not be favoured against the other; rather, they should complement each other (Gjøystdal et al., 2002). For instance, RT can help to initialize an FD simulation by setting up the time and space dimensions and subsequently help with analyzing the FD results; conversely, FD can be used to verify the wave modes generated by RT (Lecomte et al., 2004).

Some of the main comparisons between RT and FD methods is summarized in Table 4.1, (see Gjøystdal et al., 2002; Lecomte et al., 2015).

Table 4.1: Comparison between RT and FD modelling. Modified from Gjøystdal et al (2002) and Lecomte et al (2015).

RT	**FD**
High frequency assumption	High frequency assumption not applicable
Smooth model parameters represented with interfaces and properties	Gridded model with properties. Interfaces absent
Can simulate one wave mode at a time	Can only simulate full wavefield
Synthetic seismogram with user-specified wave mode	Synthetic seismogram will always contain all possible wave modes
Can choose wavelet for computing synthetic seismogram	Frequency range is predefined
Variety of output: synthetics seismograms, traveltimes, raypaths, ray angles and many other attributes	Only synthetic seismograms and snapshots
Unreliable amplitudes	More reliable amplitudes
Surface waves and head waves are not modelled	Surface waves and head waves included in the modelling
Diffractions can only be modelled approximately	Diffractions included in the modelling
Useful for survey planning and data analysis	Useful for benchmark studies
Provides traveltimes for migration and tomographic inversion	Used for testing full waveform migration algorithms
Less computation time	More computation time

Figure 4.18 is an example of results from Gjøystdal et al. (2002) obtained from RT (A) and FD (B) simulations using the same subsurface model, the same vertical seismic profile (VSP) survey geometry, and the same source pulse. The ray codes specified for the RT modelling were direct arrivals and P-wave reflected as P-wave from all possible interfaces in the model. For the FD modelling, free surface multiples were excluded in the simulation by specifying absorbing boundary conditions at the surface.

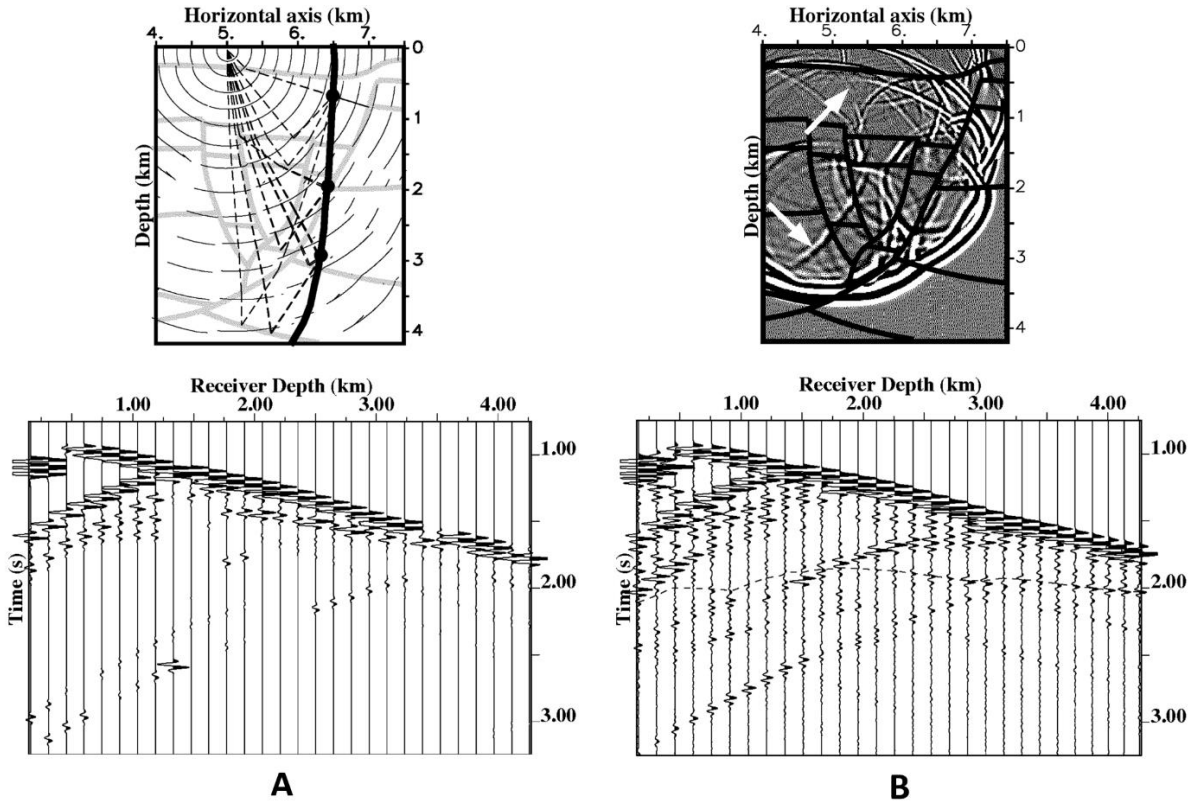

Figure 4.18: Comparison between RT (A) and FD (B) modelling using the same subsurface model and a VSP survey. A (top) represents the model: the thick grey lines represent interfaces, the thick black line represents the well path with three geophone stations along the well, the thin black lines represent wavefronts, and the dashed black lines represent some selected raypaths for direct arrivals and primary reflections. A (bottom) represents the RT based synthetic seismogram. B (top) represents snapshot from FD modelling at 1.5 s: the thick black lines represent the interfaces; the white arrows are pointing at artificial boundary reflections from one of the edges of the model. B (bottom) represents the FD synthetic seismogram. From Gjøystdal et al. (2002).

From the results shown in the figures, the following observations are summarized from Gjøystdal et al. (2002):

- A (top): The 'holes' (or missing data) observed on the wavefronts as it propagates through the faulted area are due to diffractions or over-critical incidence angles. Neither diffracted nor head waves are shown (head waves are not modelled by RT methods).
- B (top): The snapshot at 1.5 s shows various events that are difficult to analyze, hence not all the events can be confidently associated with a particular wave mode.

- A (bottom): The RT synthetic seismogram do not contain all the possible events, but direct arrivals are mostly of good quality. The primary reflections are incomplete due to diffractions associated with the faults.
- B (bottom): The FD synthetic seismogram contain more events (full wavefield, except multiples in this case) with less amplitude distortion in comparison with the RT synthetic seismogram. However, it is difficult to associate each of the events with a particular wave mode. The reflected arrival to the deepest receiver (event at 2 s) is an artificial reflection from the left edge of the model (wavefront pointed by two white arrows in the snapshot above) which was not completely attenuated by the boundary condition applied. This artificial reflection would have been very difficult to identify without analyzing the rays (RT modelling can take into account the edges of the FD-modelling grid).

4.4 Time-to-depth conversion

Time-to-depth conversion of interfaces (or horizons) interpreted from time migrated seismic data are a very important step in seismic exploration. Time-to-depth converted data are required to tie the seismic data with well log data since seismic data are recorded as a function of time and well log data as a function of depth (Zhou, 2014). The conversion is performed by converting the interpreted interfaces or time-migrated data which represent zero-offset two-way traveltimes, to depth using a known velocity field (Keydar et al., 1989).

There are various time-to-depth conversion methods, and the method chosen is often dependent on the complexity of the model, and computation time and cost. A description of the various methods used for time-to-depth conversion is beyond the scope of this thesis; however, for interfaces interpreted from simple subsurface geology, the common procedure involves the following steps (see Yilmaz, 2001):

- From a time-migrated seismic image, interpret a set of horizons which represent reflectors indicating an *Impedance constrast* between two media in the subsurface.
- Intersect root-mean-square (RMS) velocity functions (preferably picked from pre-stack time-migrated gathers) with the TWT horizons to obtain RMS velocity maps consistent with the interfaces.
- Convert the RMS velocity maps to interval velocity maps using the Dix formula.

- Using the interval velocity maps, convert the TWT horizons to depth using vertical-ray or image-ray depth conversion techniques.

If the converted depth horizons are to be used as depth structure maps for well positioning, then the horizons may be calibrated to well data (Yilmaz, 2001) like VSP, check-shot surveys, sonic logs, or a combination of these in several wells (Etris et al., 2001).

In the present work, a vertical-ray technique known as vertical stretching was used for the time-to-depth conversion of the TWT horizons. It is a relatively straightforward process which simply converts a point at a given horizontal distance (X) and TWT (T) to horizontal distance (X) and depth (Z) by integration of the P-wave velocities along vertical timelines from the top of the model to X, T. The drawback of this technique is that X will remain the same in the depth converted data, hence the process does not include lateral positioning (Etris et al., 2001).

4.5 Seismic traveltime tomography

In seismic data processing, an accurate velocity model is key to the optimum imaging of complex subsurface structures (Le Bégat et al., 2004). In most cases where conventional velocity analysis may not be sufficient to obtain a reliable subsurface velocity model, traveltime tomography is often employed.

In seismic methods, tomography can be defined as the back projection of data along a path connecting a source and receiver using a mathematical inverse method (Zelt, 2011). A typical seismic traveltime tomography entails the reconstruction of a velocity model within a subsurface area of interest in which the computed traveltimes match the traveltimes obtained from the observed (real) seismic data (Lines and Newrick, 2004). Basically, the traveltimes in a seismic data corresponding to several criss-crossing rays can be used to construct 2-D or 3-D image of the subsurface seismic velocity variations (Zelt, 2011). The traveltimes are almost exclusively the first-arrivals of any wave phase because later arrivals due to multi-pathing are difficult to identify and pick (Rawlinson et al., 2010). The process itself involves RT, thus ray theory (Cerveny et al., 1977; 2001) is the foundation upon which the forward modelling used in most traveltime tomography algorithms were built (Zelt, 2011).

A linearized gradient approach to traveltime tomography is often used. In this approach, an initial model is required, and both the model and rays are updated iteratively with the

expectation of a final model that is comparable with the real data (Zelt, 2011). A simple illustration which shows the basic approach and typical features in most seismic travel time tomography is represented in Figure 4.19. In this simple illustration by Rawlinson et al. (2010), a synthetic model consisting of evenly spaced grid points and smooth velocity field is generated, then the traveltimes of the earliest arriving geometric rays are computed for a given set of source-receiver pairs. The computed traveltimes were considered to be equivalent to the traveltimes one may obtain from seismic data recorded in the field. In Figure 4.19c, an initial velocity model (constant velocity in this case) with identical source receiver positions as in Figure 4.19a is subjected to repeated forward RT, and linearized inversion finally generates the solution model represented in Figure 4.19d, which remains the same despite further iterations, and matches the synthetic model in Figure 4.19a. In practice, there is no prior idea of a reference model that is accurate enough to predict the rays beforehand due to the degree of lateral velocity heterogeneity in the earth's interior, especially at shallow depths, hence a nonlinear tomographic method must be applied to controlled (artificial) source data in which the rays must be determined along with the unknown velocity structure as part of the inverse problem (Zelt, 2011).

As applicable to most methods, the seismic traveltime tomography method used in the present work is also based on first-arrival times. It is akin to the method presented by Korenaga et al. (2000). The method assumes a smooth velocity field which increases with depth. Initial (input) velocity models are parametrized as a sheared grid. The purpose of the sheared grid is that it allows accurate traveltime computation where rapidly varying topography exists (Korenaga et al., 2000). This method is well-suited for the velocity model in this study, given the rapidly varying bathymetry, hence it will ensure that the known water depth is represented accurately prior to the traveltime computation. The method is capable of inverting refraction traveltimes (with an option to also include reflection traveltimes) to obtain a 2-D velocity structure. It utilizes a hybrid RT scheme based on the graph method with ray-bending correction, and a set of tomographic equations (Korenaga et al., 2000; 2012). In the graph RT method, the computed rays will always follow the shortest paths between the source and receiver, hence it is also known as the shortest path method (Korenaga et al., 2000, Zelt, 2011). The method is widely used, and it is very well suited for complex heterogenous media (Van Avendonk et al., 2001; Zelt, 2011). However, the hybrid RT scheme which includes ray bending corrections to the graph-based RT computations is more efficient and computes

highly accurate traveltimes for a wide range of seismic refraction studies (Van Avendonk et al., 2001). Details of the traveltime tomography method is provided in Korenaga et al. (2000).

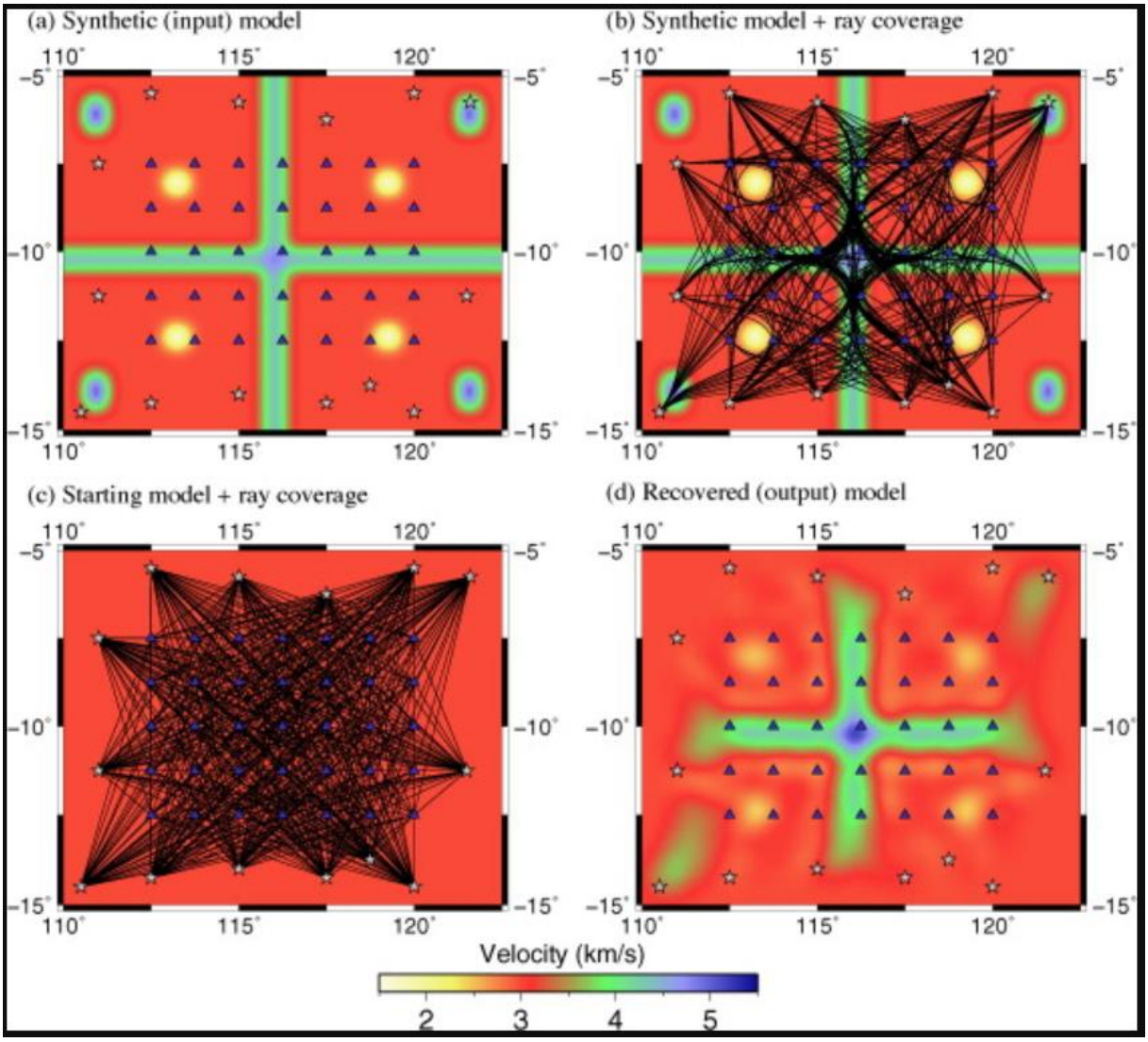

Figure 4.19: Typical features of seismic traveltime tomography. (a) Test model in spherical shell coordinates showing sources (grey stars) and receivers (blue triangles) overlaying the model; (b) same test model in (a) with raypaths of all first-arrivals plotted; (c) initial model showing the raypath coverage for the iterative non-linear inversion; (d) computed model which can be compared with (a). From Rawlinson et al. (2010).

Chapter 5: Data

This chapter presents the datasets that were used to construct the model. They consist of interpreted TWT 2-D / 3-D horizons, velocities from well and seismic data, and densities from well data. Most of the datasets were provided by NGU.

5.1 Interpreted 3-D horizons

3-D TWT horizons supplied by NGU were produced by interpolation of interpreted 2-D seismic sections acquired within the land segment of the Ramså Basin and the Andfjorden marine area (see Figure 3.1). To mitigate uncertainties in the interpretation, gravity and magnetic interpretation were integrated with the seismic to interpret obscured areas, especially for the top Basement horizon (Brönner et. al.,2017). Three 3-D TWT horizons were provided:

- Base Quaternary
- Near Base Cretaceous Unconformity (BCU)
- Near Basement

Figure 5.1 below represents the 3-D TWT horizons.

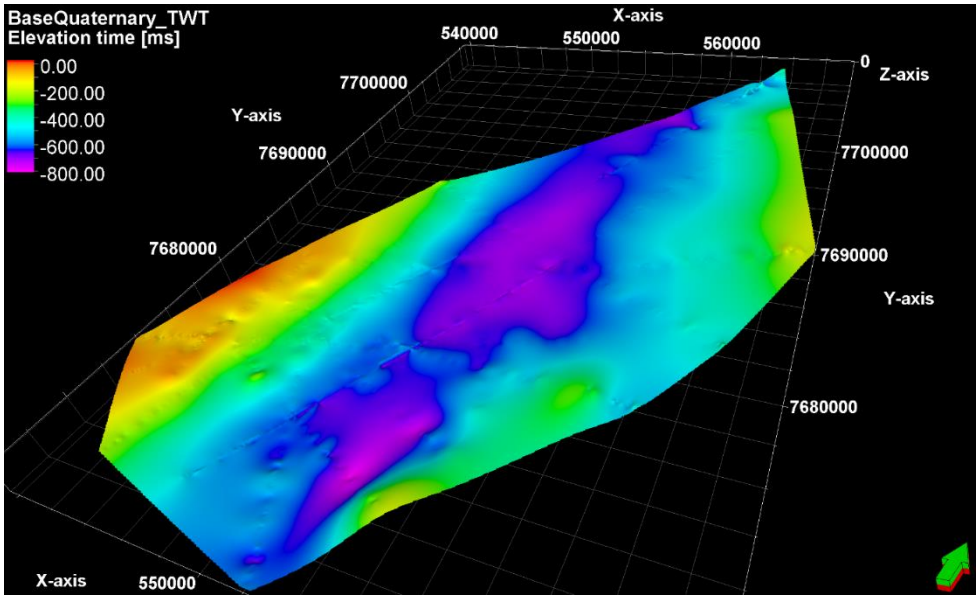

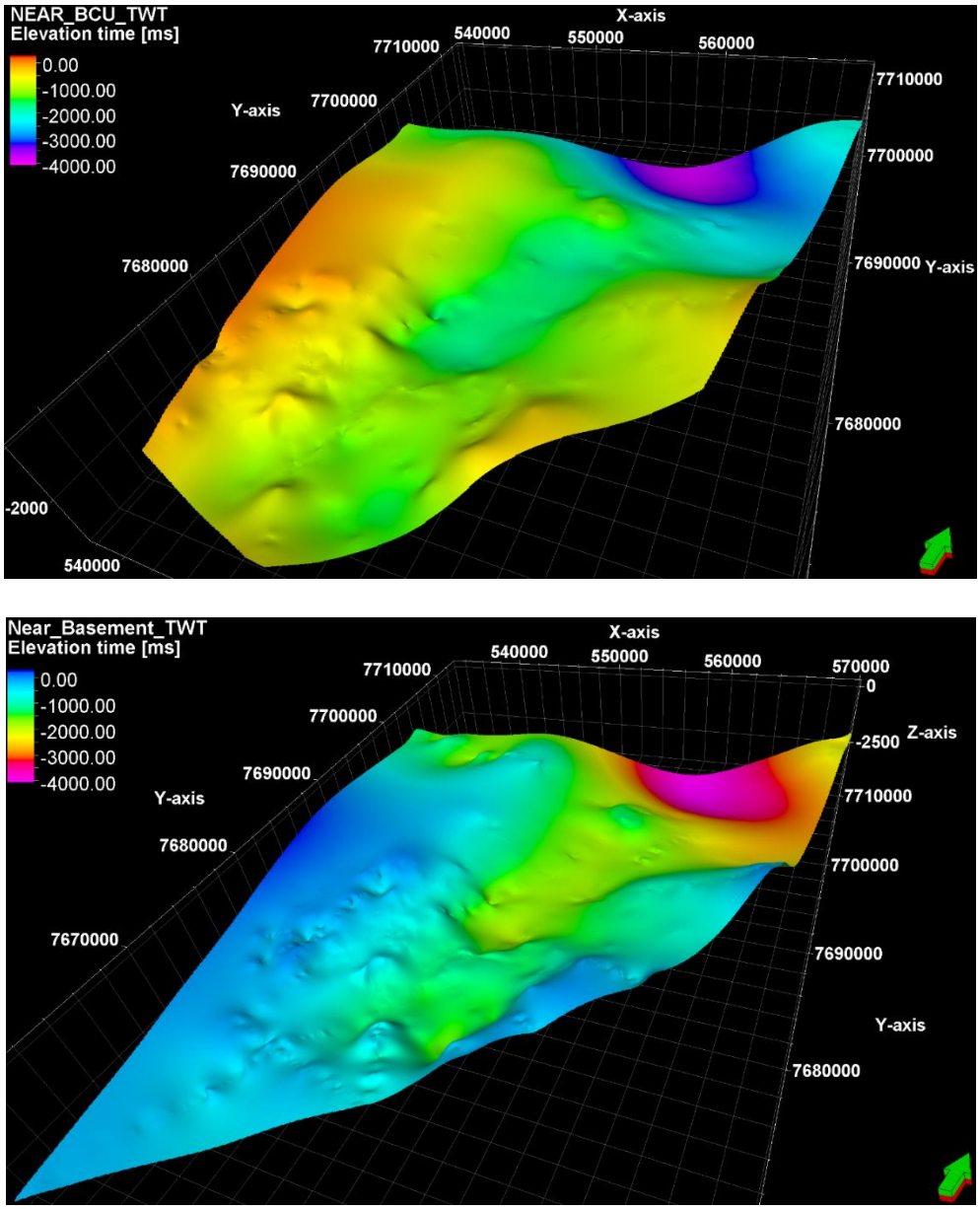

Figure 5.1: 3-D TWT horizons provided by NGU. Base Quaternary (top), Near BCU (middle), and Near Basement (bottom). UTM-X and UTM-Y are in metres. Vertical exaggeration is 2.

5.2 Digital Elevation Model and Digital Bathymetric Model

Digital elevation model (DEM) and digital bathymetric model (DBM) data of the study area were extracted from høydedata.no and dybdedata.no, respectively. These representations of the topographic surface of land and seabed within the study area are measured in depth and can help to constrain the model. Figure 5.2 represents the elevation around the Ramså Basin area and the bathymetry in the marine Andfjorden segment.

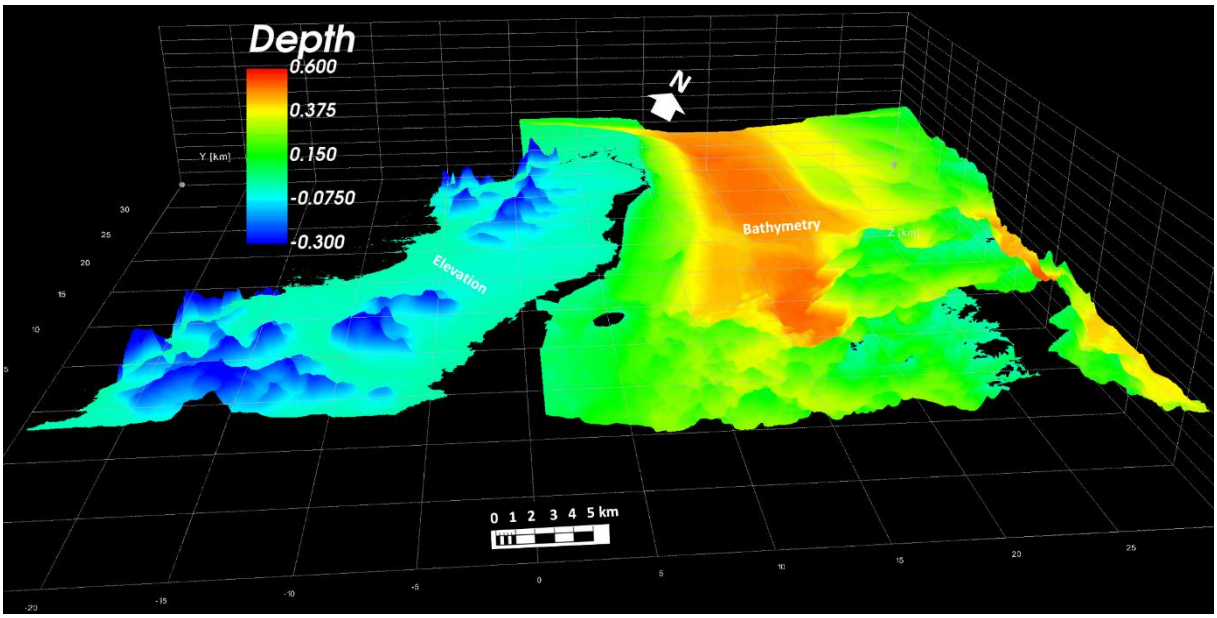

Figure 5.2: DEM and DBM data of the study area. Vertical exaggeration is 5. The black area in the TZ and at some locations on the bathymetry are due to unavailability of data. Data courtesy of høydedata.no and dybdedata.no.

5.3 Processed 2-D seismic images and interpretation

Migrated land and marine seismic sections in the same orientation as TZ-seismic line 3 were provided in SEG-Y format. A composite plot of the land and marine seismic section is represented in Figure 5.3. The acquisition parameters are shown in Table 5.1. The coverage of the land and marine seismic sections are 3.74 km and 16.0 km, respectively. The distance between the land and marine seismic lines is 1.46 km. Therefore, the total distance of the composite seismic image of the land and marine lines, including the gap along the TZ zone is 21.2 km. The receiver spread of TZ-seismic line 3 is much shorter (1.5 km) and the shot range is about 4.8 km which gives an offset in the range of 1.5 to 7.8 km.

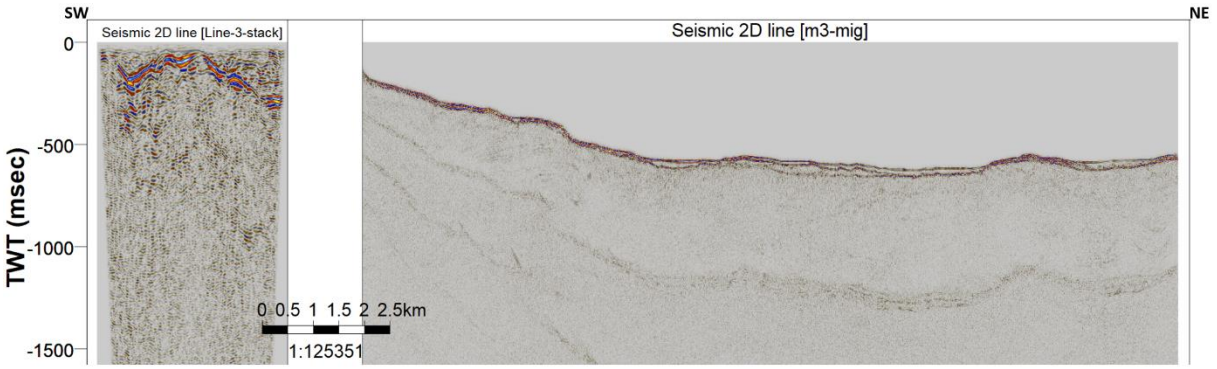

Figure 5.3: Composite seismic images of 2-D land and marine lines in the same orientation as TZ-seismic line 3. Plotted with exaggerated TWT axis.

Table 5.1: Acquisition parameters for the processed land and marine seismic sections in the same orientation as TZ-seismic line 3.

	LAND	**MARINE**
Seismic source	Detonating cord	Air gun
Source depth	Ground Level (GL)	3 m
Source (gun) pressure	-	2000 psi
Source (gun) total volume	-	90 cu. in.
Shot interval	25 m	15 m
Receiver	Sercel Unite nodes (RAU3)	Mini-streamer
Receiver depth	GL	3 m
No. of receiver groups	300	8
Receiver group interval	12.5 m	6.25 m
Receiver sampling interval	2 ms	1 ms

Figure 5.4 represents the interpretation of the processed land and marine seismic lines. The acquisition challenges and complexity of the subsurface geology affected the data quality of the seismic image, hence gravity and magnetic data aided in the interpretation of top Basement (Brönner et al., 2017). Base Quaternary, BCU and two lower Cretaceous reflectors inferred to be near Base Barremian and near Base Aptian were identified and interpreted from the seismic data. The interpretation also includes faulted layers, especially in the marine segment. Details of the interpretation are presented in Brönner et al. (2017).

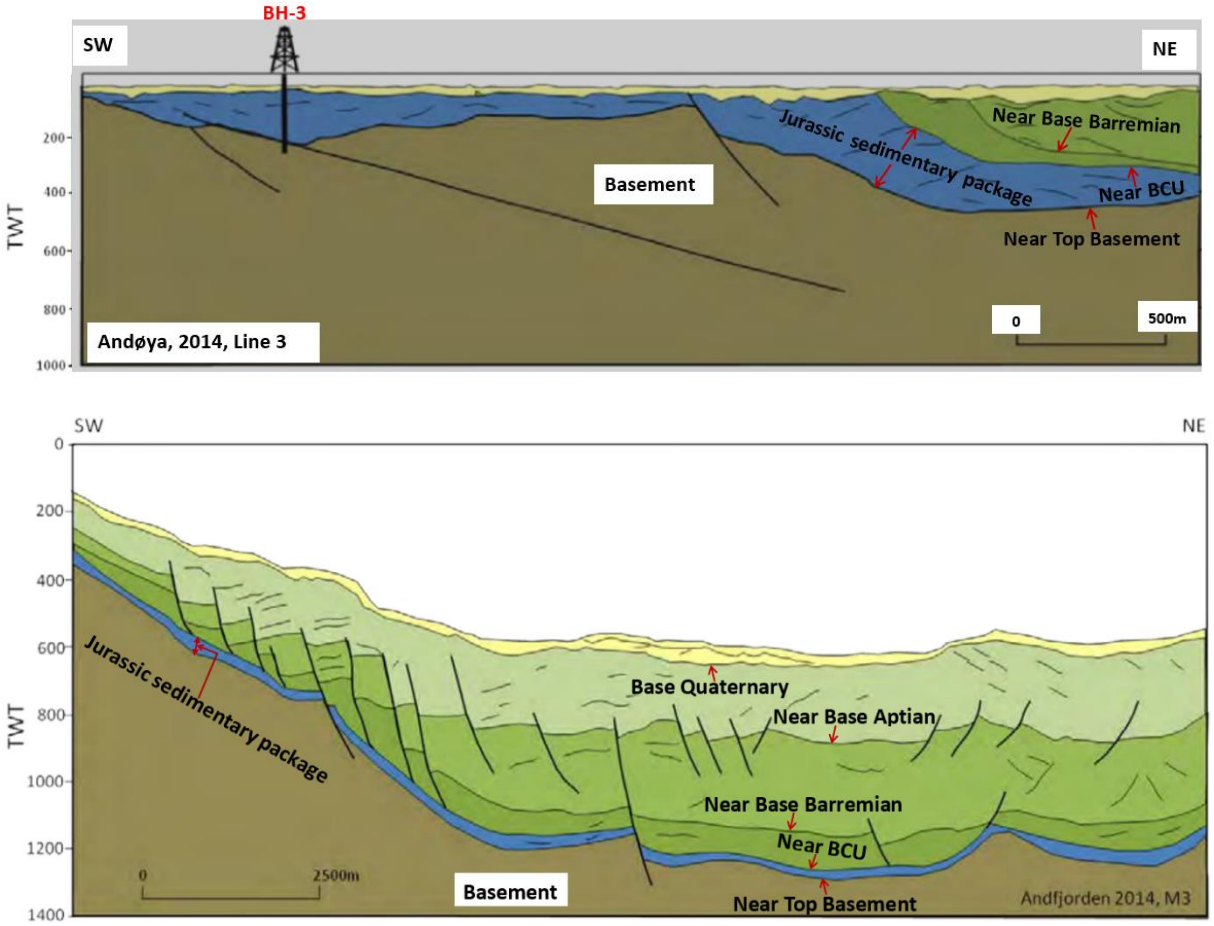

Figure 5.4: Interpretation of land (top) and marine (bottom) seismic lines in the same orientation as TZ-seismic line 3. Modified from Brönner et al. (2017).

5.4 Well data

Three out of four well datasets were obtained from core samples taken from shallow exploration wells drilled by Norminol Oil Company between 1972 and 1974. The core samples, which were stored by the Norwegian Petroleum Directorate (NPD), were retrieved by NGU and measured for P-wave velocity and for density. Figure 5.5 shows the P-wave velocity and density profiles from wells A, B and C. The locations of the wells are shown in Figure 5.6. The density values range between 2.4 to 2.7 g/cm^3 for the sediments and up to 3.0 g/ cm^3 for the basement rocks. The P-wave velocities range between 2500 m/s to 4300 m/s on the average, but up to 6000 m/s were measured in the basement rock in well C. The spikes indicating high values in density and P-wave velocity are suspected to be caused by calcite veins (Brönner et al., 2017). The total depths of the measured interval are 545 m, 541 m and 346 m for wells A, B and C, respectively.

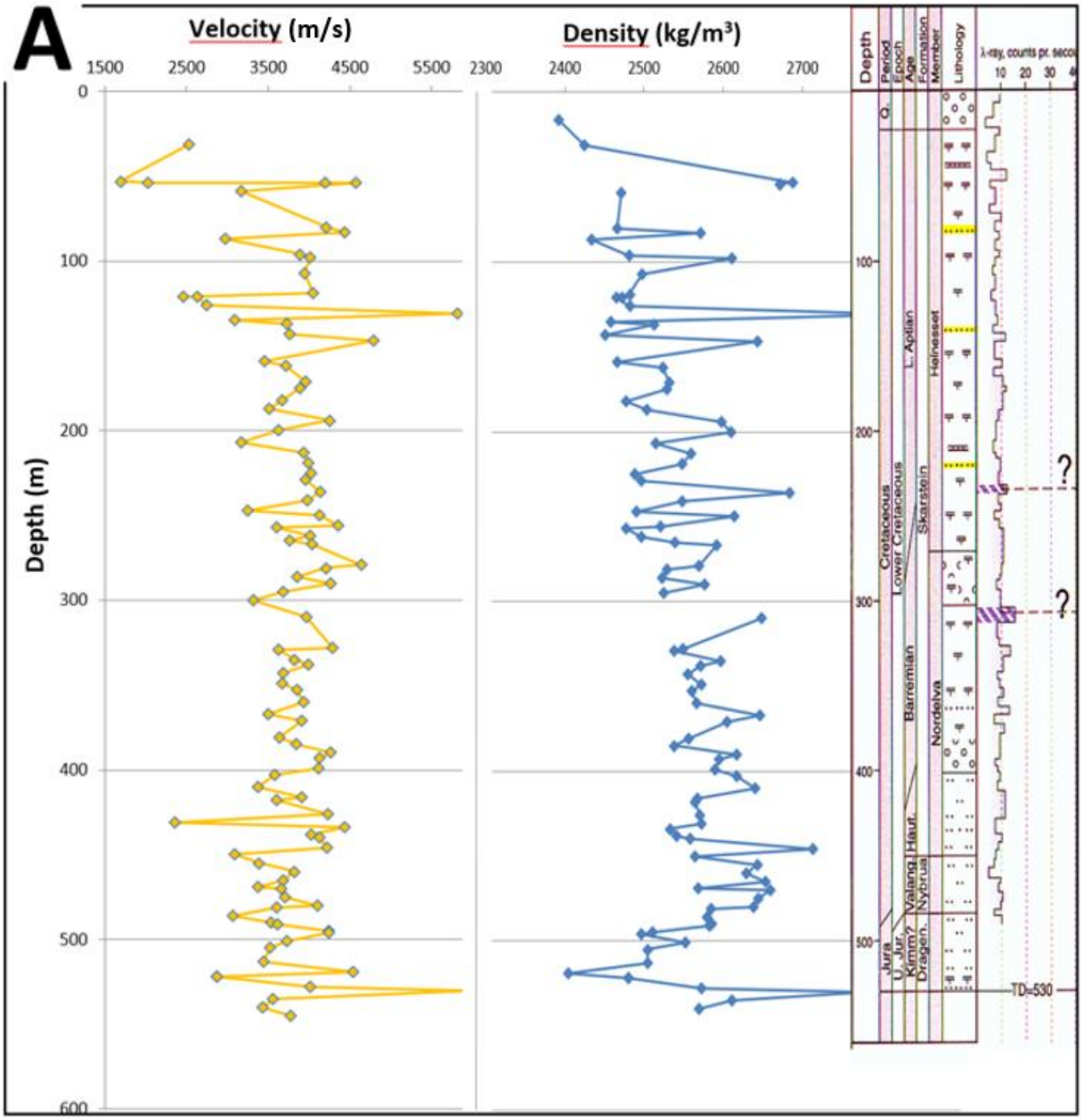
A
Velocity (m/s)
1500
2500
3500
4500
5500
Density (kg/m³)
2300
2400
2500
2600
2700
Depth (m)
0
100
200
300
400
500
600
Depth
Period
Epoch
Age
Formation
Member
Lithology
Q.
Cretaceous
Lower Cretaceous
L. Aptian
Barremian
Valang.
Haut.
Nybrua
Skarstein
Nordelva
Jura
U. Jur.
Kimm?
Dragen.
?
?
TD=530

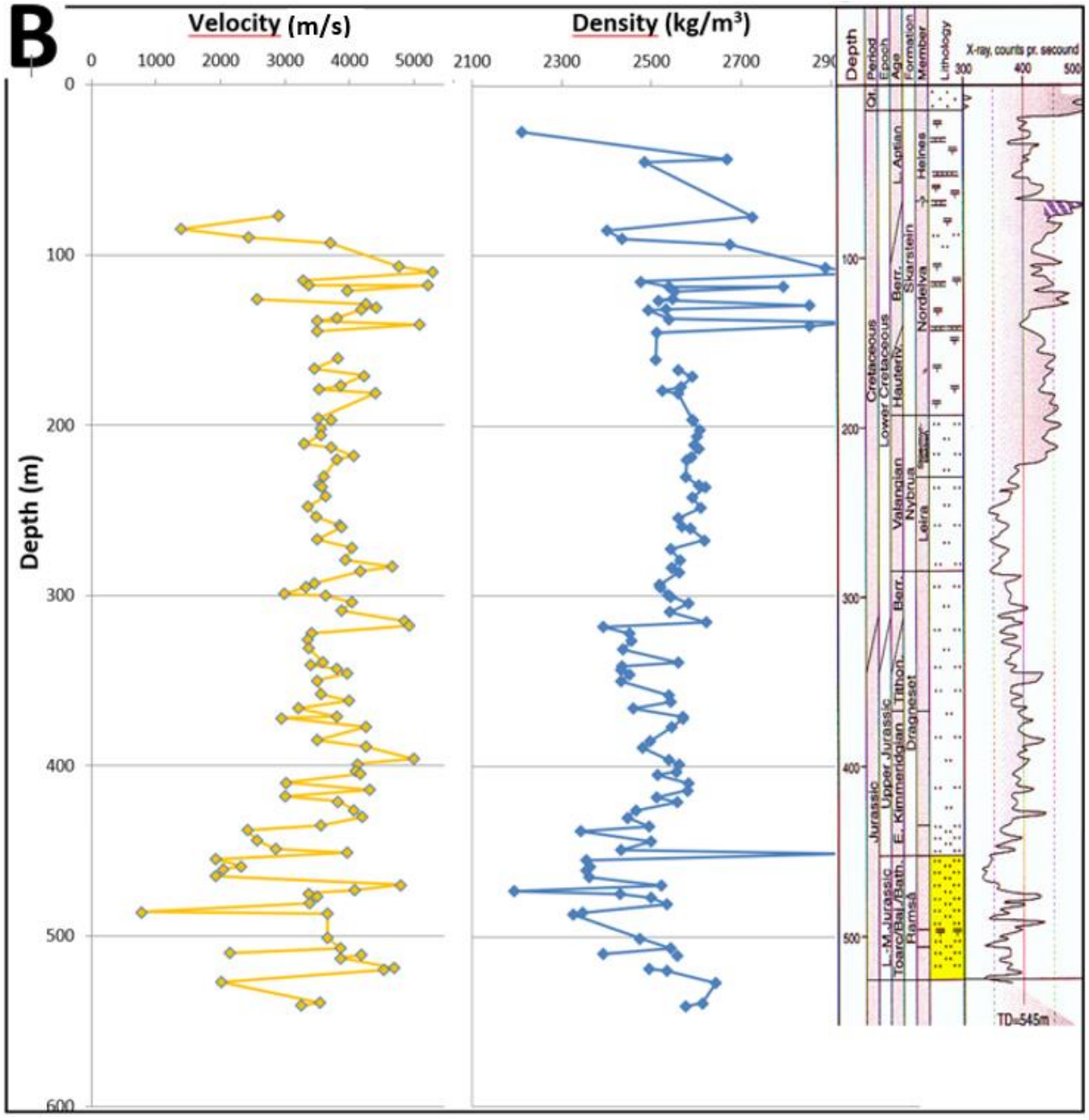
B
Velocity (m/s)
0
1000
2000
3000
4000
5000
Density (kg/m³)
2100
2300
2500
2700
Depth (m)
0
100
200
300
400
500
600
Depth
Period
Epoch
Age
Formation
Member
Lithology
X-ray, counts pr. second
300
400
500
Cretaceous
Lower Cretaceous
Jurassic
Upper Jurassic
L. Aptian
Berr.
Hauterivian
Valanginian
Berr.
Tithon.
E. Kimmeridgian
L.-M. Jurassic
Toarcian/Bath.
Heimdal
Skarstein
Nordvik
Nybrua
Lomvi
Dragonset
Heimdal
TD=545m

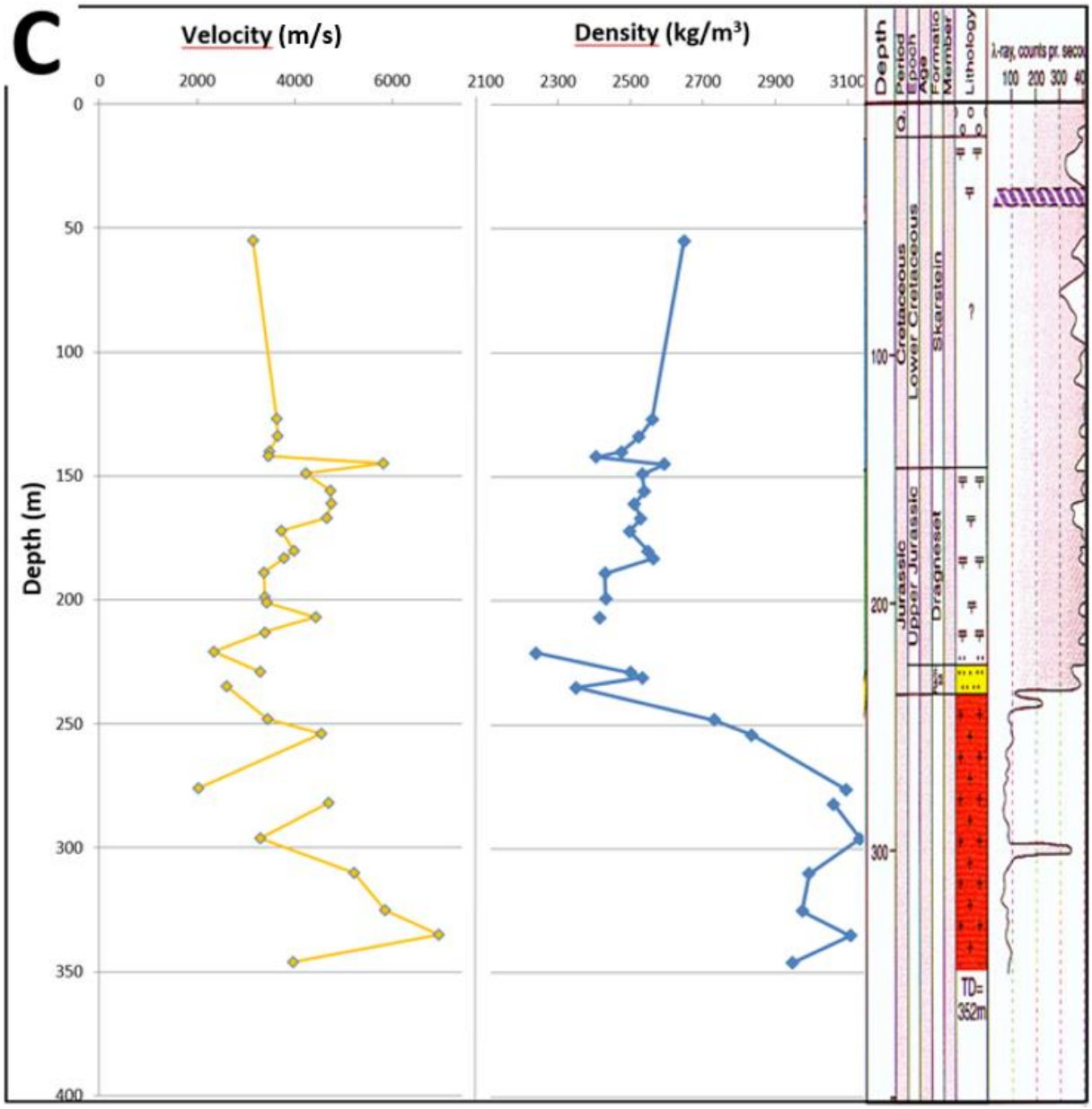

Figure 5.5: P-wave velocity and density profiles measured from core samples extracted from old shallow exploration wells drilled by Norminol Oil Company. The location of the wells are represented in Figure 5.6. Well A (top), Well B (middle), and well C (bottom). Modified from Brönner et al., (2017).

Four new wells were drilled in the area by NGU in 2015 and 2016 to facilitate achievement of the objectives set out for the large-scale geoscientific study at Ramså Basin. The four wells were logged and petrophysical datasets including velocities were acquired. Figure 5.6 represents the location of the new wells (BH1, BH2, BH3 and BH4) including the old Norminol wells (A, B, C and D).

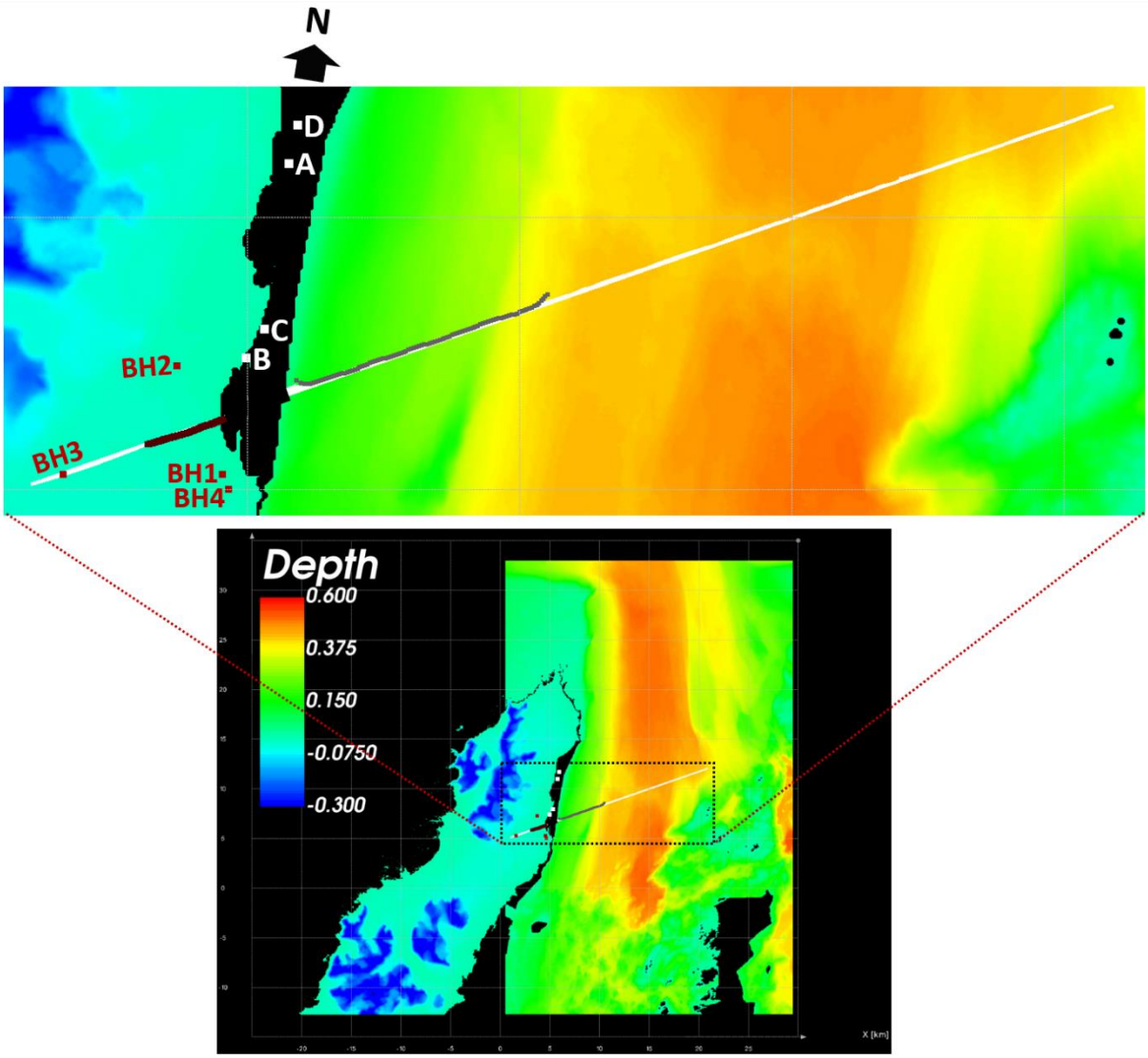

Figure 5.6: Top view of elevation and Bathymetry within the study area showing positions of old Norminol wells (A - D) and new NGU wells (BH1 - BH4). The white line represents the coverage of the processed land and marine seismic sections acquired in the same orientation as TZ-seismic line 3. The dark brown and grey lines represent the receiver and shot positions, respectively, for TZ-seismic line 3. The gap between the elevation and bathymetry is due to unavailability of data.

BH4 was drilled at the assumed southern border of Ramså Basin to test a further extension of sedimentary units (Brönner et al., 2017). The borehole was drilled to a depth of 53.7 m, continuously revealing bedrock, which confirms the location to be outside the Ramså Basin area. During subsequent logging in the bore, the resistivity sonde got stuck at 52 m depth and was abandoned after several unsuccessful attempts to recover it (Brönner et al., 2017). Table 5.2 shows the total depth, logged depth and deviation for all the four wells.

Table 5.2: Borehole information for the four wells drilled by NGU at Ramså Basin. Modified from Brönner et al., (2017).

WELLS	M.A.S.L	DEPTH (m)	DIP (°)	AZIMUTH (°)	LOGGED DEPTH (m)
BH1	10	203.5	66	N 180	142 – 157
BH2	15	217.5	60	N 290	201 – 215
BH3	26	225	90	Vertical	220 – 223
BH4	9	53.7	65	N 180	51.5

Formation velocities (P-wave) were acquired from the new wells using a sonic probe with a transmitter and three receivers placed at 20-cm interval between each of them. Figure 5.7 represents the P-wave velocity profile from three of the wells. The average estimates of the formation velocities and corresponding lithologies are listed in Table 5.3. As also observed in the old wells, the abrupt spikes in velocities are suspected to be caused by calcite veins (Brönner et al., 2017). In BH1, velocities along several depth ranges were edited out due to a depth error caused by faulty equipment (Brönner et. al.,2017).

Generally, the P-wave velocity contrasts between the sedimentary layers are relatively low and ranges between 2400 m/s at the shallowest level to about 3500 m/s along the deeper sedimentary layers. A gentle variation in P-wave velocities is observed along most part of the profile except for a slight velocity contrast between Dragneset and Ramså Formation, and between Kullgrøfta and Hestberget members within the Ramså Formation. However, the P-wave velocity contrasts between the sedimentary and basement rocks are clearly visible, with values in the basement reaching up to 4500 m/s in BH3 (the basement in BH3 is a compacted weathered basement). The basement is severely fractured in BH2, hence the very low P-wave velocity value.

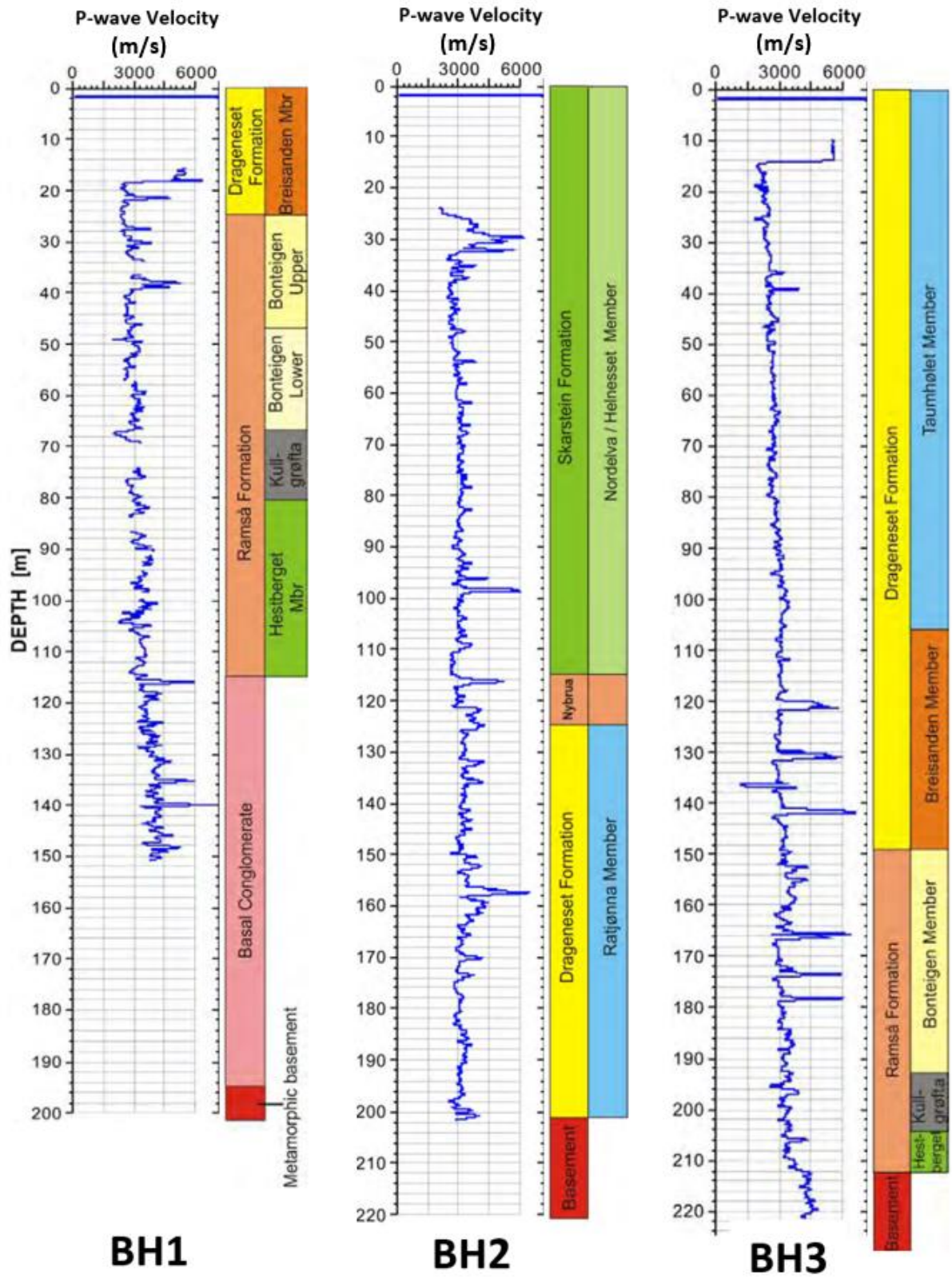

Figure 5.7: P-wave velocity profile of the formations from the new wells drilled by NGU (the well locations are shown in Figure 5.6) Modified from Brönner et al., (2017).

Table 5.3: Average P-velocity profiles of the formations and associated lithologies from the new wells drilled by NGU. Modified from Brönner et al., (2017).

Formation	Member	BH1 P-vel (m/s)	BH1 Lithology	BH2 P-vel (m/s)	BH2 Lithology	BH3 P-vel (m/s)	BH3 Lithology
Skarstein	Nordelva			3060	Mudstone, sandstone		
Nybrua				3380	Sandstone, siltstone, marls		
Dragneset	Ratjønna			3300	Laminated siltstone		
Dragneset	Taumhølet					2700	Fine-grained sandstone
Dragneset	Breisanden	2800	Micaceous sandstone			3025	Micaceous sandstone
Ramså	Bonteigen	2965	Sandtone, siltstone, thin layers of coal			3210	Coarse-grained sandstone, siltstone, thin coal layers
Ramså	Kullgrøfta	2880	Bituminous shale (oil shale)			3335	Bituminous shale, oil shale
Ramså	Hestberget	3290	Coarse-grained sandstone			3515	Coarse-grained sandstone
Basal Conglomerate / Basement		4000	Basal Conglome-rate	3400	Granodior-ite	4350	granodiorite

5.5 Velocities derived from seismic data

The migration velocity model used for imaging the land-seismic section was provided. The velocity was obtained via 2-D seismic tomography based on first breaks (Brönner et al., 2017;

Johansen et al., 2020; cf. Korenaga et al., 2000, for details about the method). The velocity model was provided in SEG-Y format and is displayed in Figure 5.8.

The sub-seabed velocity information within the marine Andfjorden area is relatively unknown. An interval velocity of 3500 m/sec between the water column and the seabed was derived from the stacking velocity model which was used for processing the marine seismic lines (Brönner et al., 2017).

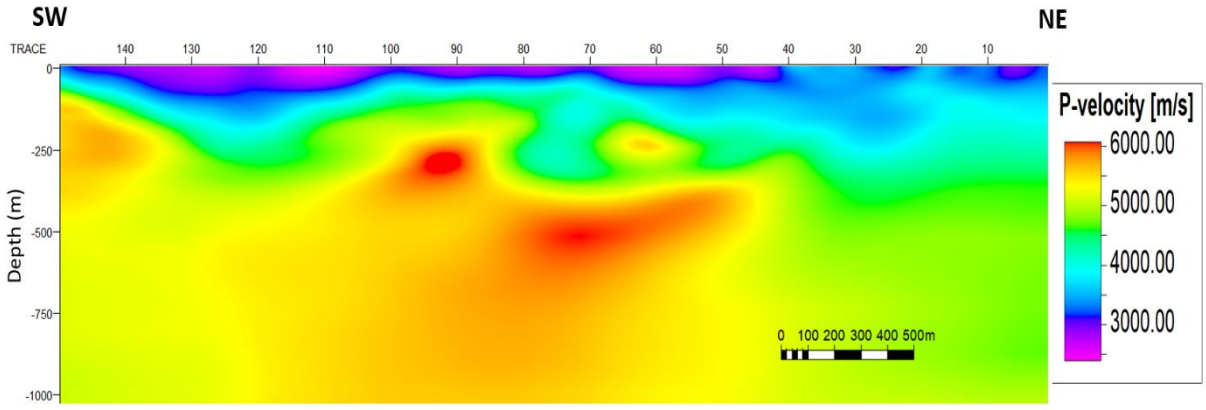

Figure 5.8:Velocity field obtained along the land seismic section acquired in the same orientation as TZ-seismic line 3.

P-wave velocities derived from refraction seismic surveys performed at Andøya between 1969 and 1971 are documented in Dalland et al. (1973). The P-wave velocities were used to stratify the Jurassic – Cretaceous successions at Andøya and correlate them with similarly stratified sedimentary successions on the continental shelf off the coast of northern Norway (Dalland et al., 1973). The P-wave velocities estimated from the refraction seismic profiles are listed in Table 5.4. Figure 5.9 is a simplified map of the Ramså Basin showing where the seismic profiles were located, and the P-wave velocities estimated from each location.

Table 5.4: P-wave velocities obtained from refraction seismic survey at Andøya. Error limits are approximately ± 0.2 km/sec. Modified from Dalland et al. (1973).

Profile number	**Sediments**			P-wave velocity in crystalline Basement (km/s)
	P-wave velocity in water-filled moraine and weathering layer (km/s)	P-wave velocity in L. Cretaceous layer (km/s)	P-wave velocity at the transition between U. Jurassic – L. Cretaceous (km/s)	
1				4.72
2	2.04			4.92
3			3.05	
4			3.10	5.03
5	1.75		3.05	
6	1.92	2.49	3.18	
7	1.89	2.42		

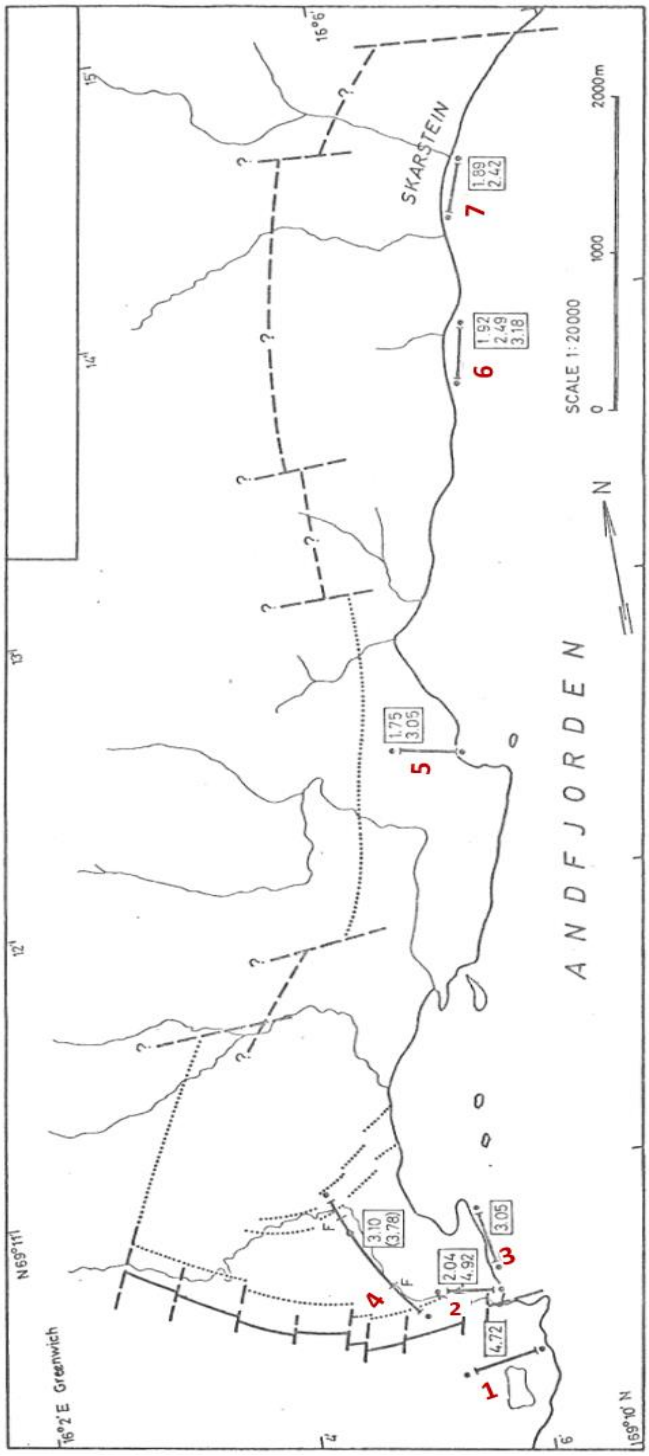

Figure 5.9: Simplified map of the Ramså Basin showing locations of the refraction seismic profiles and P-wave velocities (in km/s) observed at various locations within the field. The dotted and solid lines represent the shot points and cable layout, respectively. The numbers (in red) are the profile numbers. The P-wave velocities in the mashes and Quaternary sands are not included in the map. Modified from Dalland et al. (1973)

From the refraction seismic survey, the P-wave velocities in the water-filled moraine and weathering layer (about 15- to 20-m thick) are between 1700 to 2040 m/s. In the Lower Cretaceous layer, P-wave velocities between 2420 to 2490 m/s were measured. Within the transition between the Upper Jurassic and Lower Cretaceous sediments, P-wave velocities between 3000 and 3180 m/s were estimated. In addition, within a coarse-grained sandstone layer from the lower part of the Upper Jurassic, P-wave velocities close to 4000 m/s were measured (Dalland et al., 1973). The P-wave velocities of the basement rock ranges between 4700 to 5000 m/s.

Chapter 6: Methodology

This chapter presents the methodology used in the present work. 2-D full wavefield synthetic seismograms and traveltimes were generated via FD and RT modelling, respectively. The subsurface models were constructed using available data. The initial set of P-wave velocity models were derived iteratively using various combination of values based on well and seismic data. The final P-wave velocity model was computed via traveltime tomography. The subsurface models were initialized and constructed using the NORSAR Software Suite (NSS). The seismic traveltime tomography inversion was performed using Tomo2D package (implemented based on Korenaga et al., 2000) and the observed traveltimes used in the process were picked using Geogiga seismic pro application. The RT and FD simulations were performed using the NSS and Nucleus+ package, respectively.

6.1 Definition of model geometry

The processed 2-D land and marine seismic data which were acquired in the same orientation as TZ-seismic line 3 were part of the datasets which contributed to the interpretation of the 3-D surfaces in the Ramså Basin area (see Brönner et al., 2017). Figure 6.1 represents the layout of the processed 2-D land and marine seismic lines in the same orientation as TZ-seismic line 3, including the source and receiver positions of the TZ-seismic line and the well locations within the area. The land and marine lines were used to define the model geometry and initial lateral extent of the model. The main horizons used in the model are 2-D versions of the interpreted 3-D horizons (i.e., Base Quaternary, Near BCU, and Near Basement) along the land-marine seismic sections. An example using the near Basement horizon is represented in Figure 6.2.

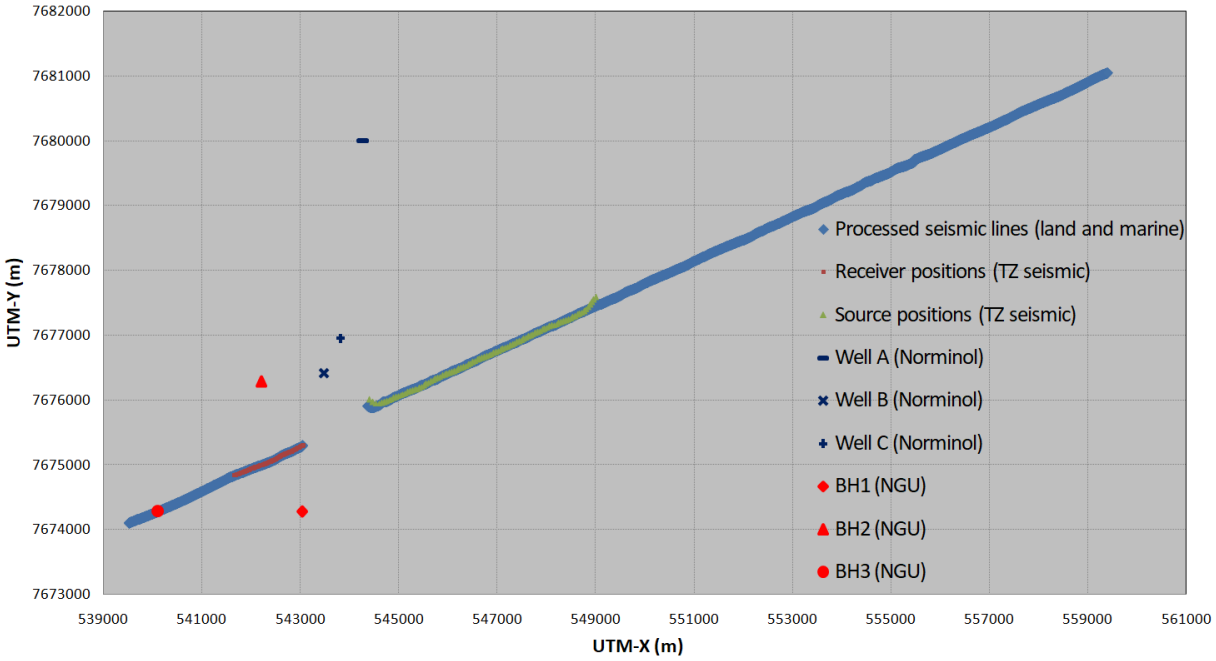

Figure 6.1: Geometry of the processed land and marine seismic lines in the same orientation as TZ-seismic line 3. The source and receiver positions of TZ-seismic line 3 are also shown in the plot, including the well locations in the area.

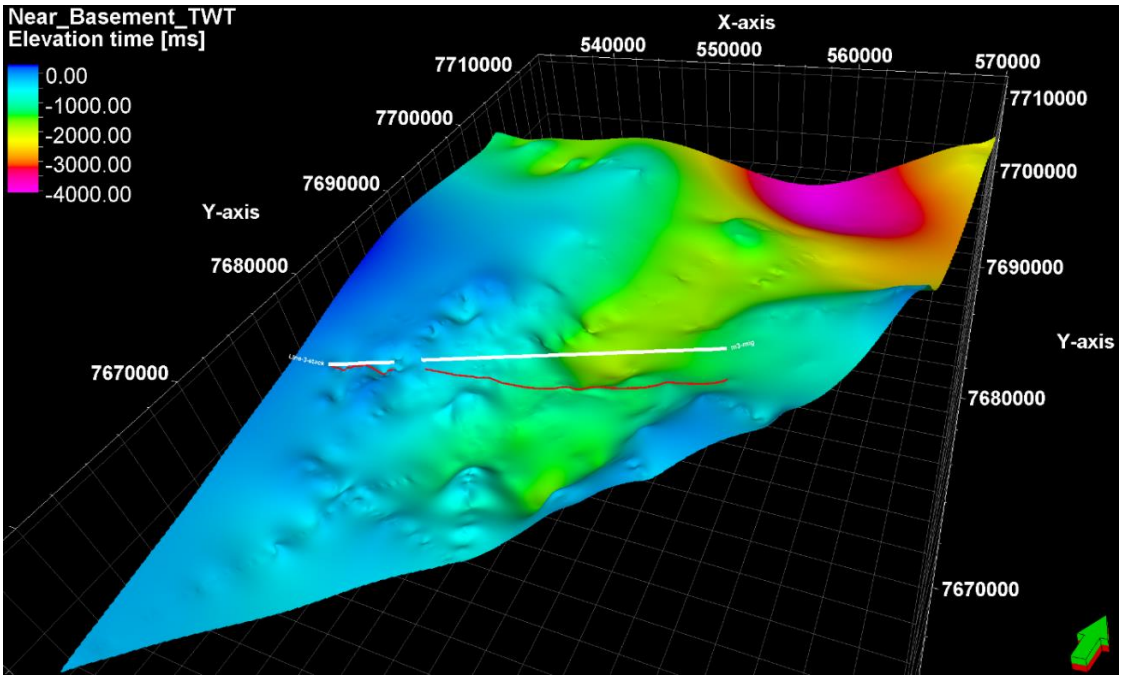

Figure 6.2: Interpreted Near Basement surface showing a cross section of the land and marine seismic sections in the same orientation as TZ-seismic line 3. The white lines represent the land (left) and marine (right) seismic profiles. The red line is a projection of the land and marine seismic lines on the Near Basement surface. The gap in-between the lines is the TZ. UMT-X and UMT-Y coordinates are in m.

6.2 Digitization of interpreted 2D TWT horizons and faults

Horizons and geological structures can be digitized from a background image and used to construct a model. To create a background image for constructing the subsurface model along TZ-seismic line 3, a composite plot of the land and marine seismic images in the same orientation as TZ-seismic line 3 was generated. The composite plot includes 2-D versions of the interpreted 3-D surfaces provided by NGU (Figure 6.3). However, to capture the structural details of the subsurface, especially in the marine segment, the interpretation presented in Brönner et al. (2017) was utilized. The interpretation includes two intra-Cretaceous reflectors (near Base Barremian and near Base Aptian) and faults. The components of the composite plot were plotted with the same spatial and TWT scale. The plot was then used as the background image for digitizing the interfaces and faults. Figure 6.4 represents the background image. The lateral extent of the composite plot is 21.2 km, including the gap at the TZ.

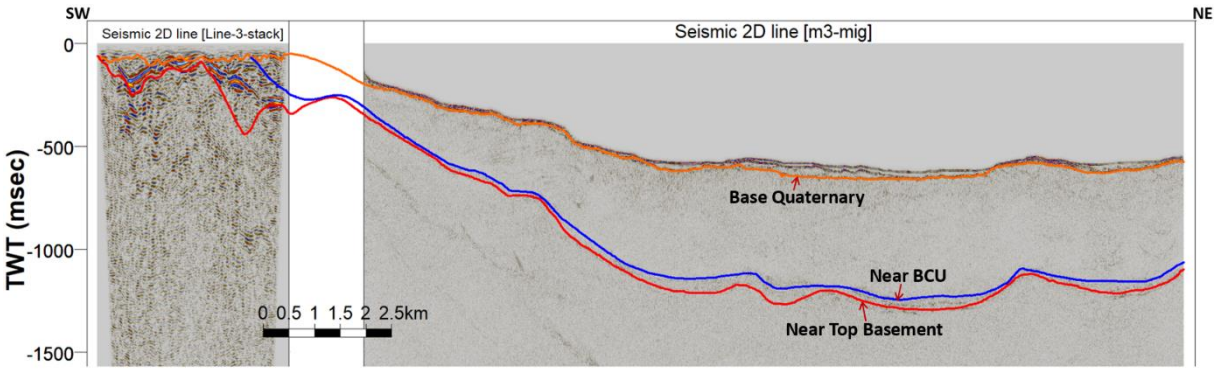

Figure 6.3: Composite plot of land (left) and marine (right) seismic interpretations in the same orientation as TZ-seismic line 3. The gap represents the TZ. Vertical exaggeration is set to five for display purposes.

Prior to digitizing the background image, three reference points were defined (in local coordinates) on the background image, i.e., the two extreme ends at the top of the image which define the origin and lateral extent of the model, and the bottom corner of the image which defines the vertical extent of the model in TWT. The distance and TWT locations of the digitized interfaces and faults were then computed based on the definition of the three reference points.

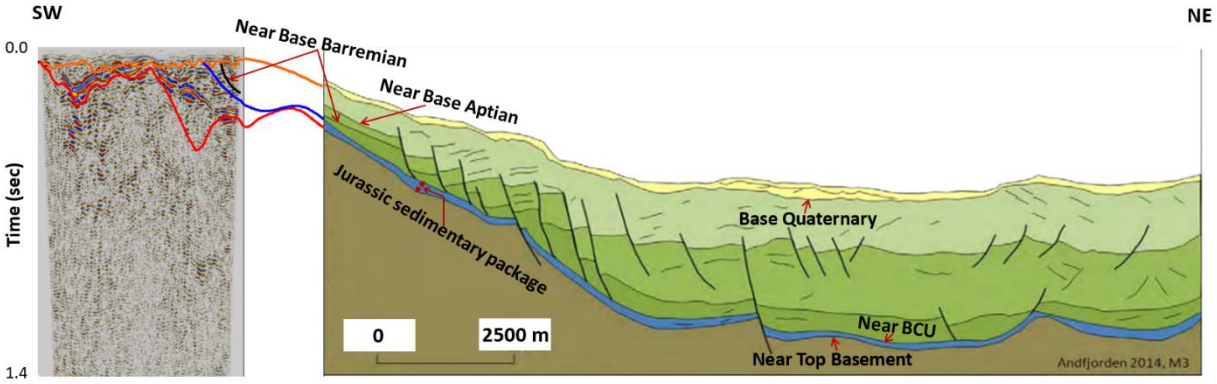

Figure 6.4: Background image used for digitizing the horizons and faults. The horizons in the land segment (left) which continues into the marine segment (right) include Base Quaternary (orange), near BCU (blue) and near Basement (red). Vertical exaggeration is set to five for display purposes.

The digitized interfaces and faults must either intersect the boundary of the model or another interface on both ends for layers (blocks) to be created in the software. Figure 6.5 represents the digitized interfaces and faults based on the background image. Near Base Barremian interface was interpolated along the TZ and near Base Aptian, which was only identified in the marine segment, was extrapolated to intersect with Base Quaternary. The extrapolation was done to meet the requirement for interfaces to intersect with the boundary of the model or another interface as mentioned above. In the model, it is assumed that near Base Aptian is truncated by Base Quaternary horizon somewhere within the TZ. This will not make any significant difference in the results given that the velocities as observed from well data are not varying very much within the sedimentary sequence.

Figure 6.5: Digitized interfaces and faults based on the background image in Figure 6.4. The two red arrows indicate the interpolated zone of near Base Barremian (green) and extrapolated part of near Base Aptian (red). Vertical exaggeration is set to five for display purposes.

6.3 Time-to-depth conversion

The digitized interfaces which are in TWT are required to be in depth-domain to perform seismic modelling. Hence, the interfaces were converted from time-to-depth using the vertical stretching method (see section 4.4). Prior to the conversion, the interfaces were smoothed and resampled. The smoothing was done to ensure that their curvature radius is large enough (Alaei, 2012), while the resampling was done to ensure that each interface is adequately sampled such that enough interface sample points will go into the time-to-depth transformation process to properly position the interfaces in depth-domain. Subsequently, blocks were generated based on the interfaces (see section 6.5) and P-wave velocities which is required for time-depth conversion, were assigned to the blocks. The initial P-wave velocities were based on well and seismic data. The final depth model was obtained through an iterative process of altering the P-wave velocities until the modelled synthetic data appeared reasonably comparable to the observed TZ-seismic data. If the interface intersections are preserved after the depth conversion, the velocities assigned to the blocks prior to the depth conversion will be retained in the depth-domain model. Otherwise, the intersections are repeated where necessary and P-wave velocities reassigned. Details about the P-wave velocities, including S-wave velocities and densities used in the model are discussed in section 6.6.

6.4 Preparation and processing of depth-converted interfaces

After time-to-depth conversion, the interfaces were ready to be used for constructing the model. For convenience and efficiency, the model area was cropped to constrain the model to the area of interest which includes the source and receiver positions of TZ-seismic line 3.

DEM data along the land seismic segment were imported into the model building tool, as well as DBM data which replaced the depth-converted seabed interface after confirming a match between the two datasets. Both datasets were interpolated at the gap (TZ) between them. Prior to importing the DEM data, the origin of the depth axis was adjusted to -0.05 km to accommodate the elevation data (i.e., elevations are negative numbers while depth below MSL are positive numbers). A new interface representing the mean sea level (MSL) was also created. The MSL interface positioned at zero depth is intersected with the interface representing the DEM – DBM interpolation. The intersection point defines the demarcation between the land (elevation) and sea.

The interfaces in the model were smoothed to ensure that their radius of curvature is large enough relative to the dominant wavelength in the observed TZ-seismic data. The TZ-seismic data have a dominant frequency of 18 Hz. For P-wave velocities ranging from 1.5 km/s to approximately 6.0 km/s, the wavelength will range from 0.08 km to 0.3 km (calculated using the relation: wavelength = velocity / frequency). Hence, the smoothing was performed by setting the minimum curvature radius of the interfaces to 0.5 km. This implies that any interface curvature radius smaller than 0.5 km will be smoothed out. In theory, RT results are considered valid for wavelengths that are several times smaller than any physical scale in the model; however, in practice it is often more robust than assumed and may provide valid results for structures down to one-fifth of the wavelength (Gjøystdal et al., 2002). The minimum curvature radius for smoothing the interfaces was kept at a minimum in order not to severely smooth out structural details in the model.

6.5 Generation of blocks (layers)

After inspection of the interfaces and faults to ensure that each of them is intersected in at least two points, blocks representing subsurface layers or geological units were regenerated (Figure 6.6). Each block is defined by an area bounded within intersecting interfaces and/or model boundary. It is important to note that some blocks with different numbers may correspond to the same geological unit (see Figure 6.6). It was not possible to create a topographic boundary in 2-D, hence a block was also generated above the topmost horizon representing the ground elevation and MSL (block 1 in Figure 6.6). This block represents air in practice and was included to confine the model at the top, given the uneven elevation above zero (MSL).

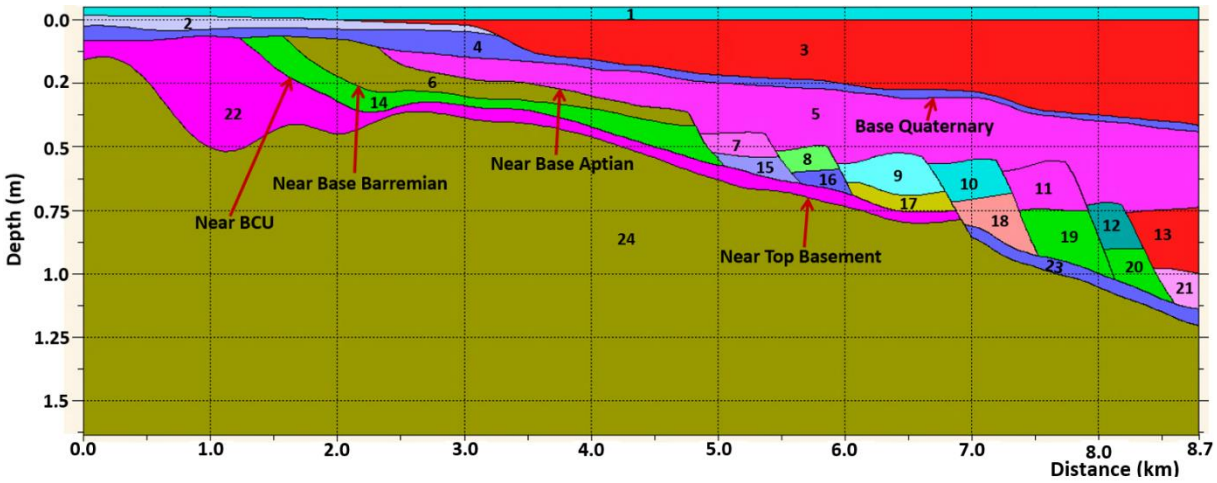

Figure 6.6: Blocks representing subsurface layers. The numbers represent the block units. Note that some blocks with different numbers may correspond to the same geological unit, these blocks are: blocks 6 -13 (between near Base Aptian to near Base Barremian); blocks 14 – 21 (between near Base Barremian to near BCU); blocks 22 and 23 (between near BCU and near top Basement). Vertical exaggeration is two.

6.6 Elastic properties

P-wave and S-wave velocities, including densities were assigned to the model on a block-by-block basis but according to the geological units. There is no information about attenuation, therefore it was not included in the model. The properties were assigned either as a constant value or gradient function. The following sub-sections describes the properties used and how they were derived.

6.6.1 P-wave velocity

The P-wave velocities of the initial set of models were based on well and seismic data (section 5.4 and 5.5). Several versions of the model were also constructed with different degrees of variation of the P-wave velocities. In an effort to derive the best attainable model that could be used to generate synthetic data comparable to the observed TZ-seismic data, a P-wave velocity model was computed via seismic traveltime tomography (section 4.5). A version of the P-wave velocity model which produced synthetic data with the closest match yet with the observed TZ-seismic data was used as the initial model (Figure 6.7). The P-wave velocity values assigned to the individual layers in the initial model consist of constant and gradient velocity functions. The velocity function is a vertical gradient which is computed by choosing a starting reference depth which can either be an interface or a constant depth along

which a given value is constant. Then a constant gradient value is defined with a sampling increment starting from the reference depth. The constant and gradient velocity functions assigned to the initial model is represented in Table 6.1 and Table 6.2, respectively.

Following the block numbers in Figure 6.6, the P-wave velocity assigned to block 4 (between the first reflector on land/seabed and Base Quaternary) is 3.4 km/s. This is close to the velocity of 3.5 km/s estimated from refracted waves within the Quaternary layer below seabed, using the marine seismic data acquired in 1988. Furthermore, within the same shallow level in the migration velocity model obtained via tomography inversion and used for imaging the land seismic section (Figure 5.8), velocities in the region of 3.4 km/s can also be observed. The average velocity of 3.1 km/s assigned to block 2 (between ground elevation and the first reflector at the land segment) is also consistent with the tomography-based velocity model.

The P-wave velocities assigned to block 5 (between Base Quaternary and near Base Aptian), blocks 6 to 13 (between near Base Aptian to near Base Barremian), and blocks 14 to 21 (between near Base Barremian to near BCU) were based on average velocities measured from the core samples extracted from the old Norminol wells, especially wells A and B (Figure 5.5). A velocity function was applied to block 5 to reflect an increasing velocity gradient from 3.5 km/s to 3.6 km/s.

Block 22 and 23 is the Jurassic sedimentary layer (between near BCU and near top Basement). The transition into this layer is marked by a reduction in velocity and density as observed from the Norminol well datasets in Figure 5.5. Although the negative velocity contrast is not easily noticeable in well A, a clear decrease in density is observed. For these layers, a gradient velocity function was computed, with velocities ranging from 3.55 km/s at the shallower level of the layer within the land segment to 3.63 km/s at the deeper levels underlaying the marine segment.

A gradient P-wave velocity function was computed and assigned below top Basement. The gradient starts with a velocity of 4.3 km/s below the basement high at the land segment to about 5.0 km/s at the base of the model. The choice of starting with a velocity of 4.3 km/s is based on the basement velocity measured from the new NGU well, BH3 (Figure 5.7).

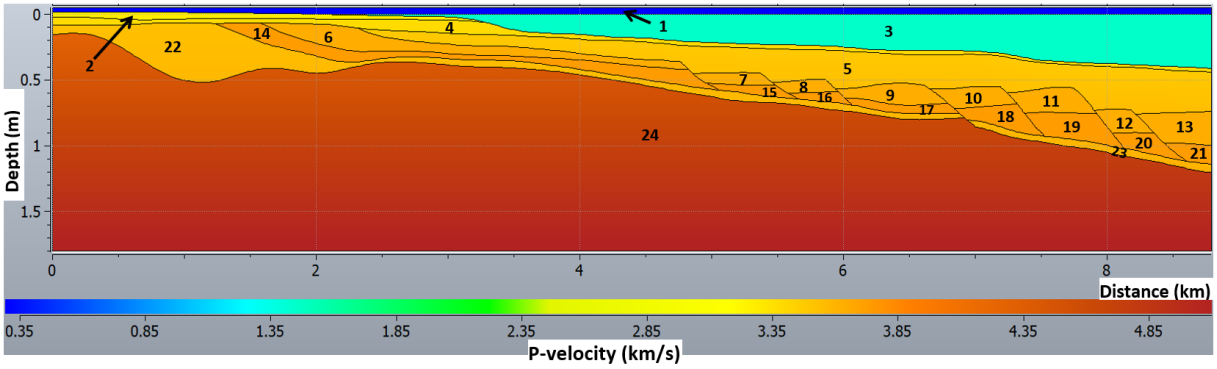

Figure 6.7: Iinitial P-wave velocity model input to seismic traveltime tomography inversion.

Table 6.1: P-wave velocities assigned to the initial velocity model input to traveltime tomography.

Blocks (layers)	**P-wave velocity (km/s)**
1	0.35
2	3.1
3	1.5
4	3.4
5	Gradient (Velocity range: 3.5 – 3.6)
6 - 13	3.65
14 - 21	3.75
22 and 23	Gradient (Velocity range: 3.55 – 3.63)
24	Gradient (Velocity range: 4.3 – 5.0)

Table 6.2: Definition of the gradient P-wave velocity functions of the initial velocity model input to traveltime tomography.

	Blocks (layers)		
	5	**22 and 23**	**24**
Reference horizon / constant depth (km)	Base Quaternary	Base Quaternary	0.15
Property along interface (km/s)	3.5	3.55	4.23
Constant gradient (km/s /km)	0.2	0.1	0.5
Sampling increment (km)	0.05	0.05	0.1

The procedure followed in the seismic traveltime tomography is described below:

1. The TZ-seismic data were sorted into CRGs which amounted to 120 set of receiver gathers. First-arrival times (first breaks) were then picked on every fourth gather. An example of the first-arrival times picked on one receiver gather is displayed in Figure 6.8. The first-arrival times were picked automatically where the wavelets have clear first breaks (trough in this case) and manually where they are not, especially at far offsets. The software used for the traveltime tomography does not allow sources in the water layer, hence prior to picking the first breaks, the sources and receivers were swapped.

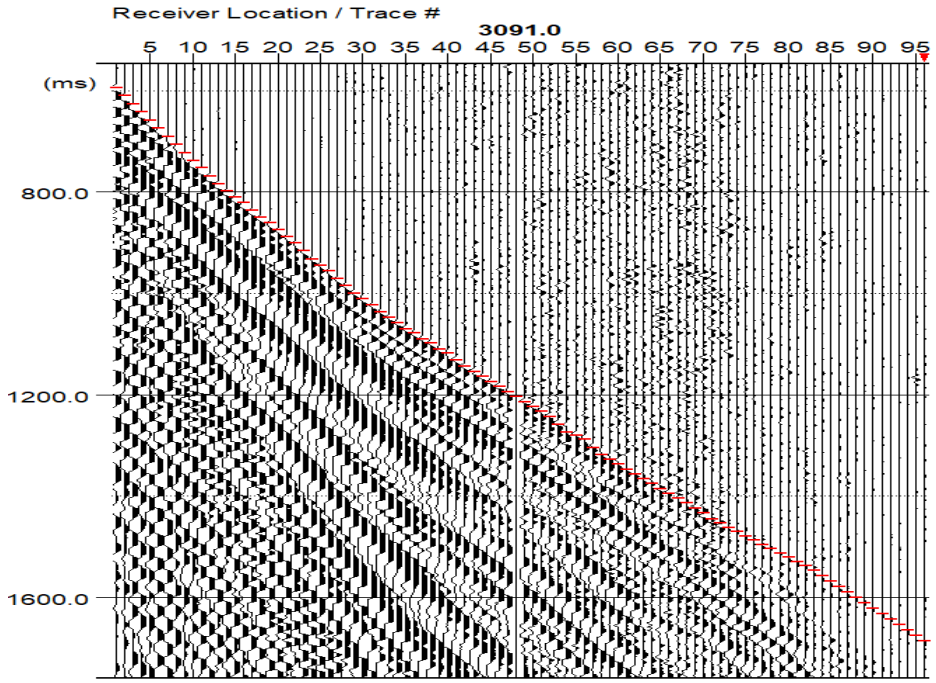

Figure 6.8: First-arrival times picked on one receiver gather (CRG 16) from the TZ-seismic data.

2. The depth origin of the initial P-wave velocity model was set to zero, excluding the elevation. Subsequently, the model was converted to a sheared grid (section 4.5) and smoothed (0.3 km and 3.0 km in the vertical and horizontal direction, respectively).

3. Using the same source and receiver positions applied to the real TZ-seismic data, traveltimes and rays were computed through the sheared and smoothed model.

4. The traveltimes picked from the observed TZ-seismic data in step one are iteratively compared to the computed traveltimes in step three. After each iteration, the traveltime residuals between the observed and modelled traveltimes were used to update the preceding P-wave velocity model. As a result, the match between the modelled traveltimes and observed TZ-seismic traveltimes increases after each iteration. After the third iteration, an acceptable match was achieved between both traveltime sets and a final P-wave velocity model was generated via inversion.

The P-wave velocity model is shown in Figure 6.9 (top). It is important to note that the traveltime tomography was performed only within the area of the initial P-wave velocity model with ray coverage as shown in Figure 6.9 (bottom). The P-wave velocities outside this area is unaffected by the process and will remain mostly unchanged except for some insignificant changes that may have occurred due to the smoothing performed in step 2.

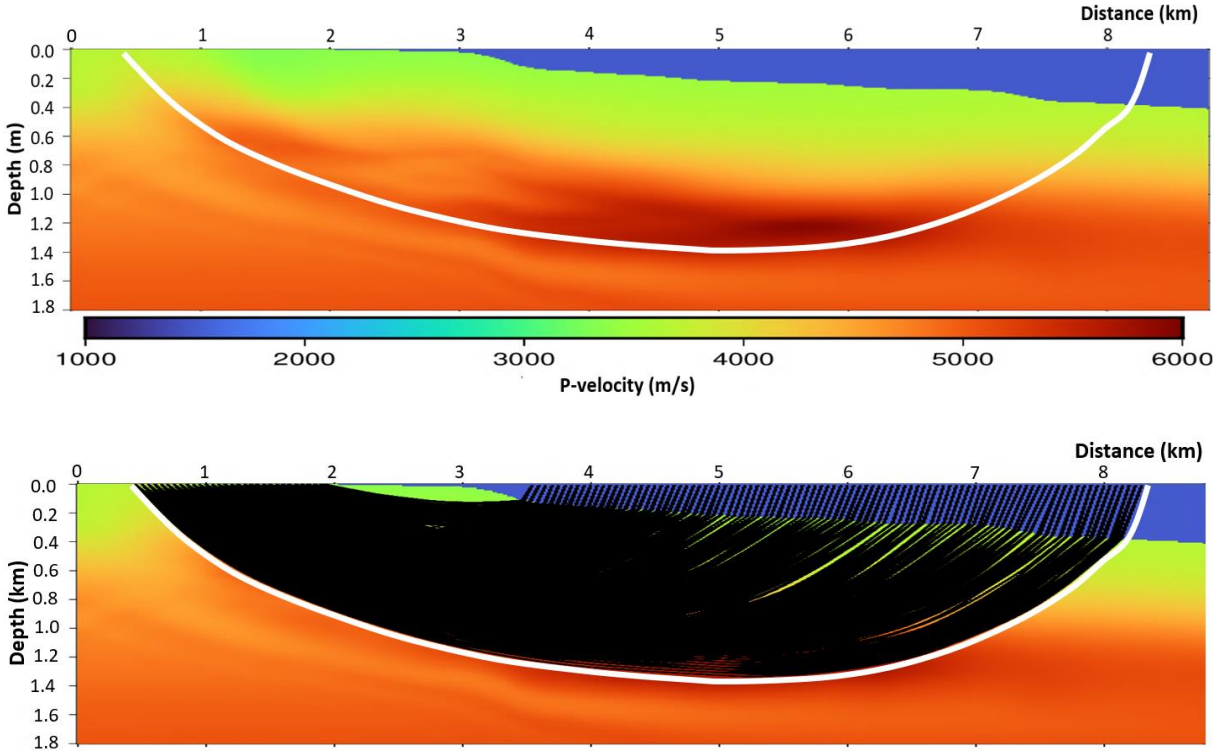

Figure 6.9: P-wave velocity model obtained via traveltime tomography (top), and raypaths across the model indicating where the traveltimes were computed. The area below the thick white line was not included in the traveltime tomography.

6.6.2 S-wave velocity

The S-wave velocities in all the models used for FD and RT modelling were based on an assumed P/S-ratio (i.e., 1.73). S-wave velocities were assigned to all the blocks except blocks 1 and 3 (air and water layer, respectively).

6.6.3 Density

Density is one of the properties required for seismic modelling. The final density values assigned to the blocks were based on average density values obtained from the Norminol well cores (Figure 5.5). The density model is represented in Figure 6.10 The actual values assigned to the models are listed in Table 6.3.

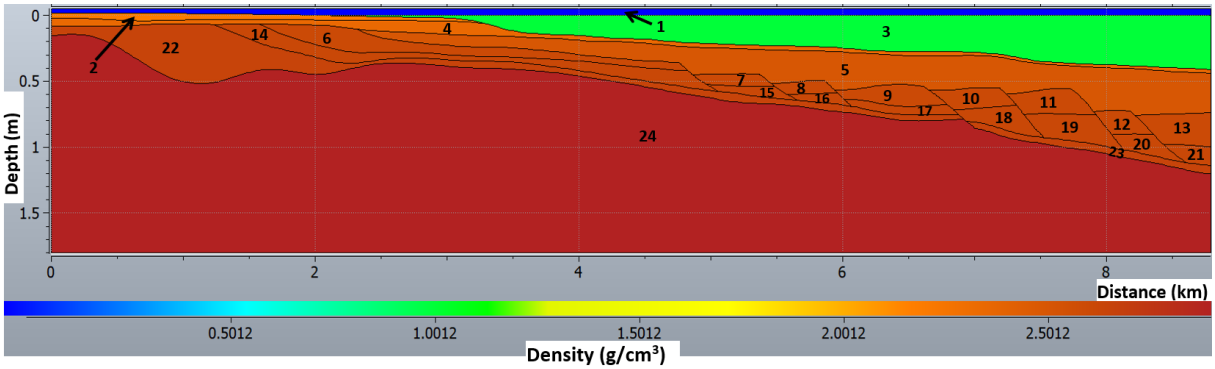

Figure 6.10: Final density model. Lower property mapping value clipped to 1 g/cm^3.

Table 6.3: Density values assigned to models used for RT and FD modelling.

Blocks (layers)	Density (g/cm^3)
1	0.0012
2	2.20
3	1.03
4	2.35
5	2.5
6 - 13	2.6
14 - 21	2.65
22 and 23	2.45
24	2.9

6.7 Survey definition

The survey used in the FD and RT simulations is based on the TZ-seismic acquisition geometry that was used in the field. The acquisition parameters are shown in Table 6.4. The source and receiver spread were not exactly along a straight line. Given that the model is restricted to 2-D, a linear best-fit line (trendline) along the spread was computed using the source and receiver positions (Figure 6.11). Subsequently, the sources and receivers were projected unto the line where they were defined with the same spatial distance and interval used in the field.

Table 6.4: Acquisition parameters for TZ-seismic line 3.

	TZ-seismic line 3
Source depth	8 m
No. of shots	98
Shot interval	50 m
Receiver depth	GL
No. of receiver groups	120
Receiver group interval	12.5 m

Figure 6.12 represents the survey as defined in the RT-modelling software. The source depth is 8 m below MSL and the receivers were placed on land (ground level). There is a total of 98 shots at mostly 50-m intervals and the shooting direction is from north-east to south-west. The last two shots were excluded from the modelling because they were more than 100-m off the best-fit line (Figure 6.11). There is a total of 120 receivers at 12.5 m intervals. The shortest and longest source–receiver offsets are approximately 1.50 km and 7.85 km, respectively.

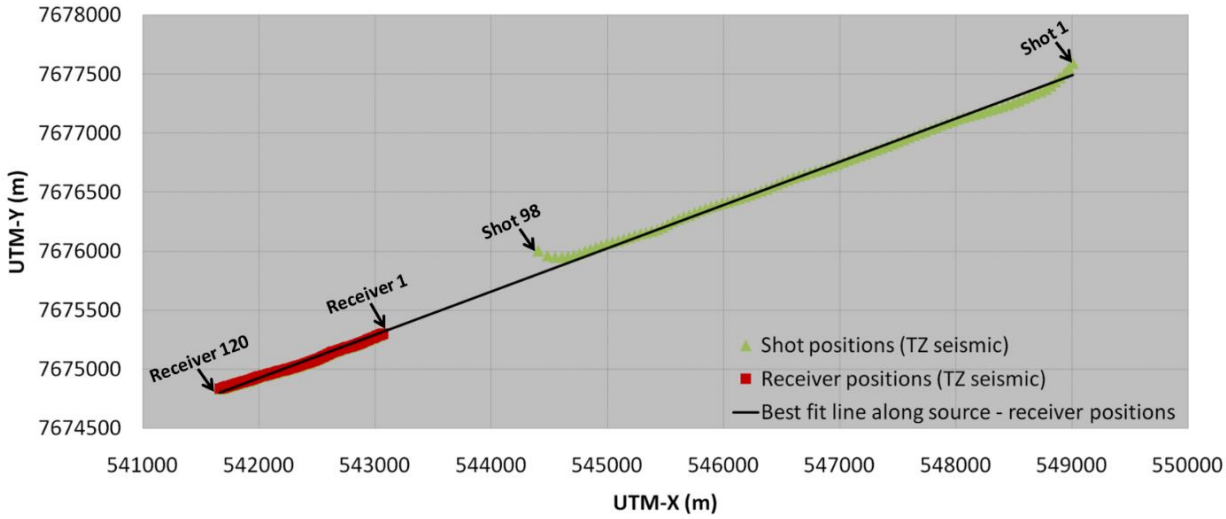

Figure 6.11: Survey geometry for TZ-seismic line 3, including the computed best-fit line along the source-receiver spread.

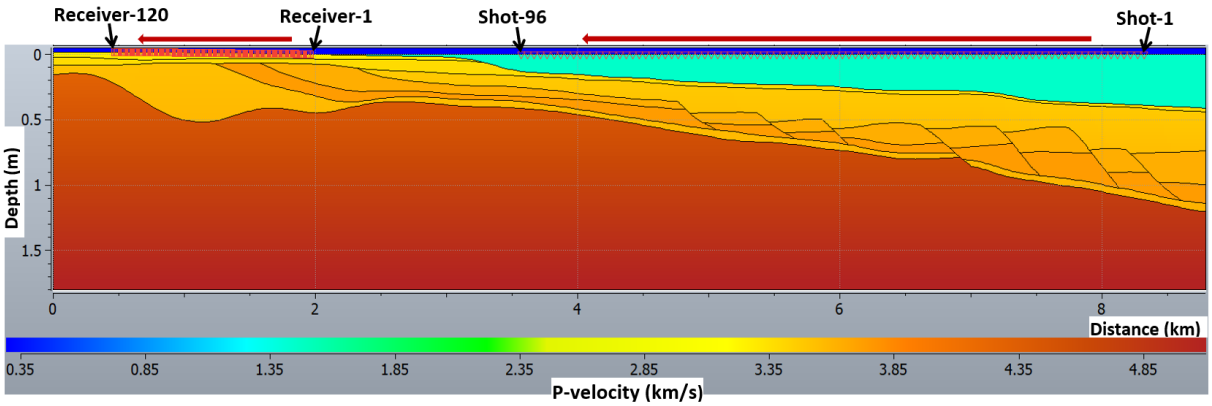

Figure 6.12: Survey definition using the initial P-wave velocity model. The shots (right) are fired from the sea and recorded by the receivers (left) positioned on land. The red arrow to the right indicates the shooting direction, while the red arrow to the left indicates the direction in which the receivers were numbered.

6.8 RT modelling

When all the essential model elements (interfaces, elastic properties, and survey) are defined, the model is ready for RT modelling based on the PRM (section 4.3.1.2). The RT parameters were defined by setting the departure angle range of the initial rays or fan of rays from the source (i.e., the search angle) from -90° to 90° with a ray increment of 0.02°. The specified search angle range implies a downward search coverage following a counterclockwise direction. A dense ray increment of 0.02° was chosen to increase the chances of generating as

many rays as possible ending up at the receivers (within a 10-cm radius); this is a key technical parameter of PRM.

Various wave modes were modelled including direct arrival, primaries, and multiples. The modelling results were stored as event sets from which attributes like traveltimes, incident/reflection angles and amplitude coefficients were extracted for data analysis.

6.9 FD simulation

The elastic properties (P-wave velocity, S-wave velocity and density) were gridded prior to FD simulation. The lateral (distance) and vertical (depth) sampling increments were set to 4 m. The vertical grid origin was adjusted to 1 m in depth, thus excluding the ground elevations which have negative depth values. The receivers were then positioned at the top of the model with the same spatial distance and interval used in the field. The exclusion of the elevation will not affect the results significantly. The ground elevation along the location where the receivers are positioned is relatively flat. With an average elevation of about 17 m and an average velocity of 3.1 km/s, the error will be 5.5 ms for a vertical ray; but in reality, the error will be lesser than 5.5 ms since the rays are not vertical. Therefore, the error may not make any significant impact on the results.

An elastic 2-D FD modelling type was chosen with an assumed isotropic medium. A coarse grid resolution was specified in the modelling. The grid resolution determines the spatial operator-length that will be automatically applied during modelling. Basically, the coarser the grid resolution, the longer the operator-length. A longer operator-length will reduce the effect from numerical dispersion, thereby enabling higher frequencies to be simulated more correctly. If a fine grid resolution were to be chosen (if the grid size were smaller), a shorter operator-length would be required to avoid numerical dispersion, and this comes at the cost of a longer computation time. Therefore, long operators are often chosen to avoid using small grid sampling and reduce the computational cost (while increasing accuracy). However, the drawback of long operators, hence coarse grid is that it impacts on the level of details that can be modelled.

The stability limit was set to one. A smaller limit will lead to a smaller time increment during the FD simulation. Although a smaller limit can lessen temporal dispersion, but the consequence is a longer computation time. In the FD package used for the modelling, the user

can specify if a temporal dispersion correction should be applied. The model buffer size is calculated and adjusted automatically. Table 6.5 represents the main parameters used in the FD modelling.

Table 6.5: Main FD modelling parameters.

Modelling type	Elastic variable density
Type of medium	Isotropic
Model grid resolution	Coarse
Absorbing boundary type	PML
Surface multiples	Included
Stability limit	1
Source type	Pressure

Synthetic seismograms containing the vertical component of particle velocity, and the pressure wavefield were generated as SEG-Y files. The modelling results also include snapshot movies which were generated with a snapshot interval of 100 ms. The FD-based synthetic records are shown in chapter Chapter 7:.

Chapter 7: Results

The seismic modelling results will be presented in this chapter. Firstly, FD-based synthetic datasets computed with three of the most relevant models distinguished by their P-wave velocities will be presented and compared with the real TZ-seismic data. The P-wave velocities contained in the three different models consist of the initial P-wave velocity (input velocity model to traveltime tomography), P-wave velocity derived via traveltime tomography, and P-wave velocity optimised for RT by updating the model on a block-by-block basis (according to the geological units) with average velocities taken from the P-wave velocity derived via traveltime tomography. Lastly, the RT modelling results will be presented and examined, followed by comparisons between the RT-based traveltimes and events on the real TZ-seismic data and FD-based synthetic datasets.

To make it easier for the reader to differentiate between the models and their respective P-wave velocities, a description of the P-wave velocities associated with each model and their corresponding names are represented in Table 7.1. Henceforth, the models and P-wave velocities will be referred to by their respective names.

Table 7.1: Names and description of the relevant models based on their P-wave velocities.

MODEL NAME	P-WAVE VELOCITY NAME	MODEL DESCRIPTION
M1	P-wave velocity 1	Initial P-wave velocity (i.e., input velocity model to traveltime tomography). See Figure 6.7
M2	P-wave velocity 2	Inverted P-wave velocity derived via traveltime tomography. See Figure 6.9 (top)
M3	P-wave velocity 3	P-wave velocity optimised for RT by updating the model on a block-by-block basis (according to the geological units) with average velocities taken from the P-wave velocity derived via traveltime tomography. See Figure 7.3 (bottom)

7.1 FD-based synthetics and comparison with observed TZ-seismic data

2-D FD elastic modelling was performed using the subsurface models constructed with varying P-wave velocity fields. The synthetic datasets generated for each model were compared with the real TZ-seismic data. The purpose was to validate the model after each model iteration by comparing the seismic events in the synthetic datasets with the seismic events observed in the TZ-seismic data until a relatively good match is established between them.

Considering that the FD modelling was performed in 2-D, the geometrical spreading factor is also 2-D (line source) which implies weaker amplitude decay due to geometrical spreading in comparison to 3-D (point source). Line-source based geometrical spreading compensation is not applied in the current version of the package used for the FD modelling. Therefore, an amplitude scaling function inversely proportional to the square root of time was applied as an approximate compensation for the difference between 2D and 3D geometrical spreading.

The TZ-seismic data, as well as the synthetic datasets are better visualized by displaying the datasets in CRGs. An example of the TZ-seismic data from a single shot displayed in CSG is represented in Figure 3.4. The reason why the CRGs looks better is because the offset range is much larger for the CRGs than for the CSGs (the shot line is 4.8 km while the receiver line is only 1.5 km) and because the ground coupling of the geophones is very variable, which would be very visible in the CSGs.

7.1.1 Model based on P-wave velocity 1 (M1)

P-wave velocity 1 was based on available data (section 6.6.1). The P-wave velocity field is represented in Figure 6.7 and the values assigned to the layers are listed in Table 6.1 and Table 6.2. FD-based synthetic datasets were computed using model M1. Figure 7.1 represents how the synthetic data compares to the real TZ-seismic data using data recorded by a receiver in the middle of the receiver spread (CRG 60) as an example. Generally, at near source-receiver offsets, there appears to be a close fit between the first-arrivals in the synthetic and observed TZ-seismic datasets, but the fit between them reduces with offset distance. It is challenging to compare individual events after the first-arrivals, given that the events in the real TZ-seismic data appear not to be continuous. However, the moveout of most of the events

after the first-arrivals in the synthetic data approximately fits the moveout of the events in the observed TZ-seismic data. Comparisons using the first receiver (CRG 1) and last receiver (CRG 120) can be seen in appendix A.

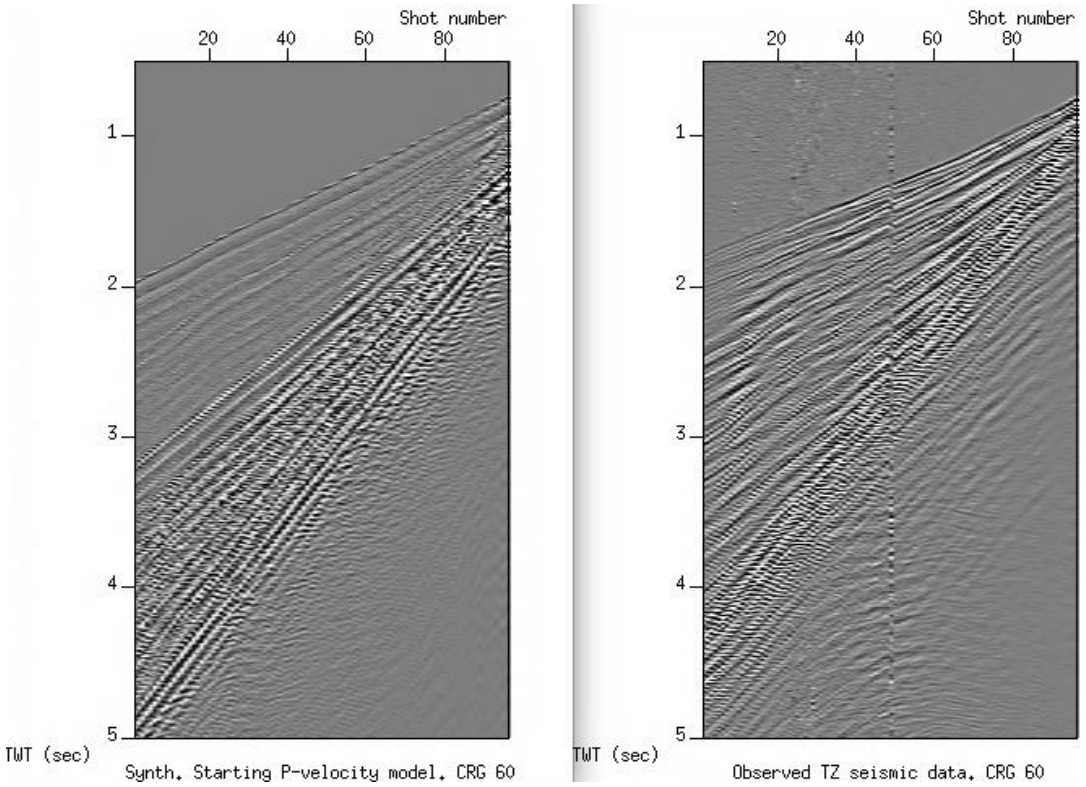

Figure 7.1: Comparison between synthetic data based on the model M1 (left) and observed TZ-seismic data (right).

7.1.2 Model based on P-wave velocity 2 (M2)

Seismic traveltime tomography was used to compute a P-wave velocity model (P-wave velocity 2) in an attempt to derive a better representation of the subsurface velocity structure along the area from which the TZ-seismic data were acquired. P-wave velocity 1 served as the initial P-wave velocity model used in the process. P-wave velocity 2 is represented in Figure 6.9. FD modelling was performed using model M2, and synthetic datasets were generated. The P-wave velocity field in the model (P-wave velocity 2) is very smooth in comparison to P-wave velocity 1; hence limiting the possibility for modelling of detailed subsurface structures. However, the traveltime of the first-arrivals can be modelled.

A comparison of CRG 60 between the synthetic data computed with model M2 and the observed TZ-seismic data are displayed in Figure 7.2. The modelled first-arrivals fit the first-arrivals observed in the TZ-seismic data as expected, since it was the first-arrivals of the observed TZ-seismic data that were used in the traveltime tomography computation. Generally, the moveout of the events after the first-arrivals in the synthetic datasets do not deviate significantly from the synthetics based on model M1. At far-offsets the amplitudes of the synthetic data based on model M2 appears weaker than the synthetics based on model M1. This is probably because the former is smoother than the latter. Comparisons using the first receiver (CRG 1) and last receiver (CRG 120) can be seen in appendix A.

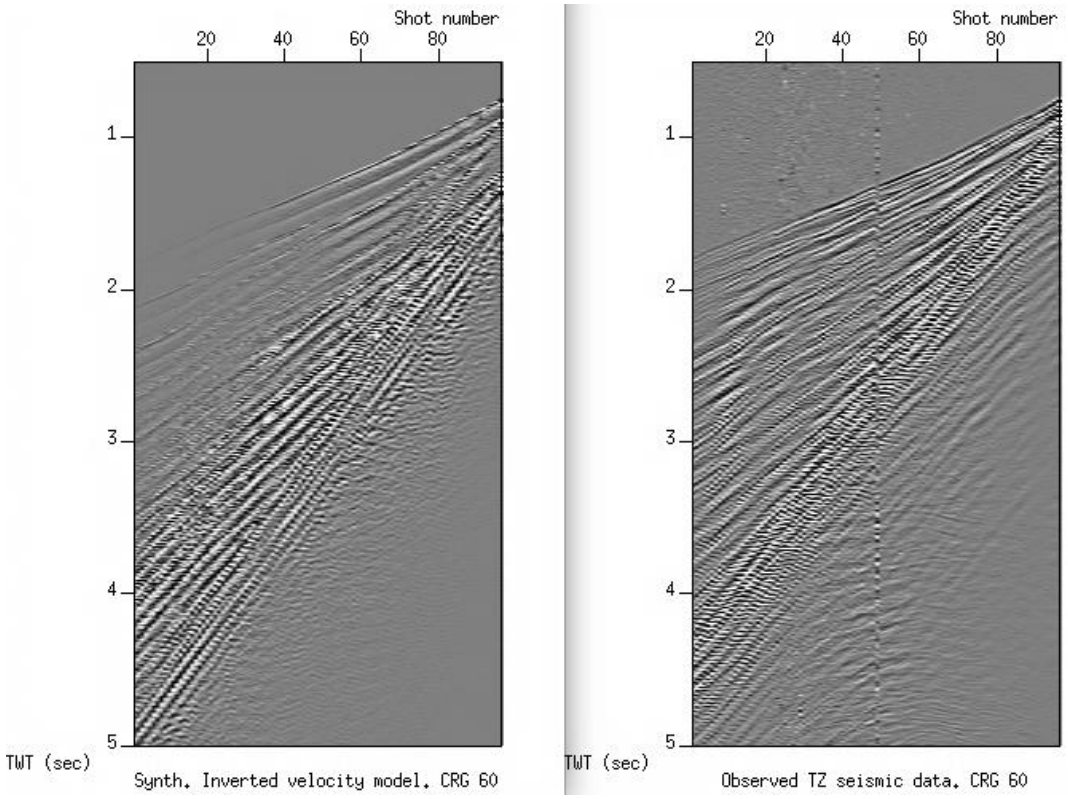

Figure 7.2: Comparison between synthetic data based on the model M2 (left) and observed TZ-seismic data (right).

7.1.3 Model based on P-wave velocity 3 (M3)

The traveltimes of the first-arrivals in the synthetic data based on model M2 fits the first-arrivals in the observed TZ-seismic data. However, the model is very smooth, and the velocity contrasts in the model no longer coincide with the interfaces used for constructing the model

(Figure 7.3, top). For this reason, the layers in the model were updated with gradient velocity functions based on estimations of average (or approximate) P-wave velocities derived from P-wave velocity 2. The layers were updated such that interfaces will correspond to boundaries representing changes in elastic impedance. The updated P-wave velocity model is represented in Figure 7.3 (bottom). The blocks updated are block 5 (between Base Quaternary and near Base Aptian), blocks 6 to 13 (between near Base Aptian to near Base Barremian), blocks 14 to 21 (between near Base Barremian to near BCU), blocks 22 and 23 (between near BCU and near top Basement), and block 24 (below near Basement). A description of the gradient velocity functions is given in Table 7.2. Block 2 (between ground elevation and first reflector on land) and block 4 (between first reflector on land / bathymetry and Base Quaternary) retained the same constant velocities of 3.1 km/s and 3.4 km/s, respectively, as assigned to P-wave velocity 1.

FD modelling was performed with the updated model (M3), and synthetic datasets were generated. To validate the model before using it for RT modelling, the synthetic datasets were compared with the synthetic datasets based on the inverted P-wave velocity model, and the observed TZ-seismic data. An example of how the three datasets compare to each other using CRG 60 is represented in Figure 7.4. The first-arrivals in the three datasets fit approximately, especially for the far-offset arrivals, and the moveout of the events after the first-arrivals fit approximately as observed in the synthetic data based on the initial model and the inverted model.

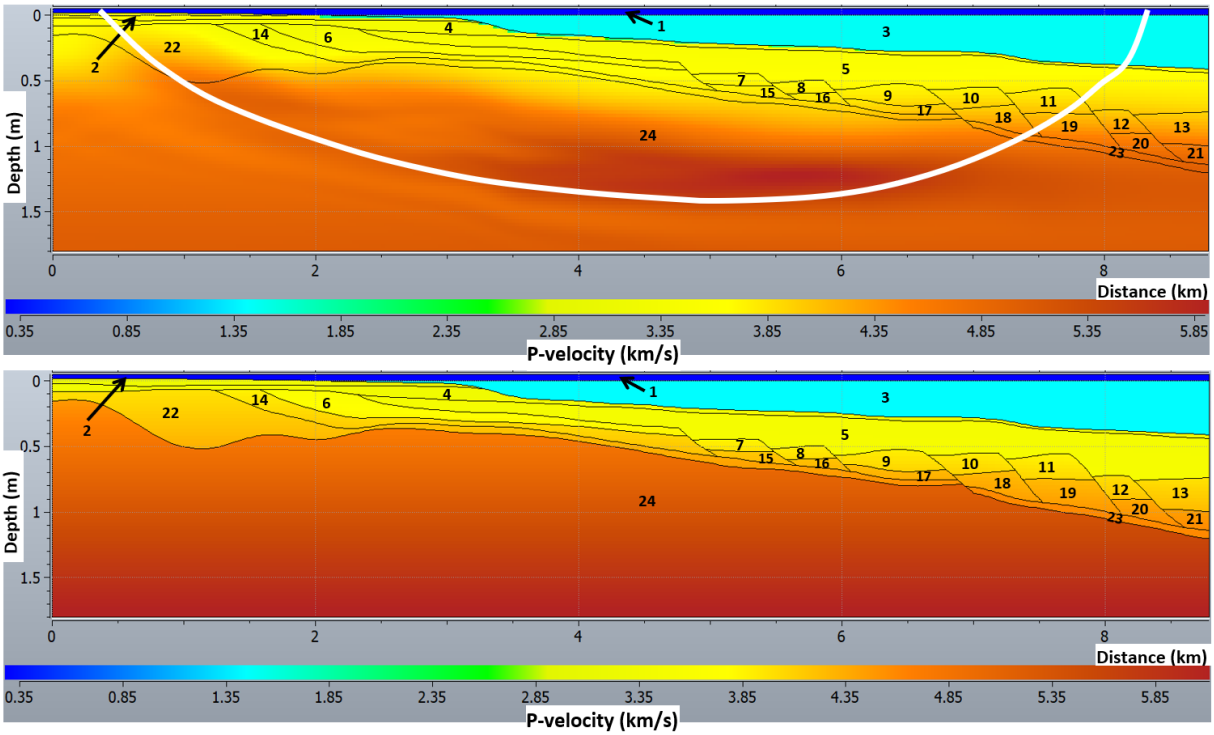

Figure 7.3: Model M2 (top), and model M3 (bottom). The area below the thick white line was not included in the traveltime tomography.

Table 7.2: Description of gradient velocity functions assigned to the P-wave velocity model updated for RT.

	Blocks (layers)					
	5	**6 - 13**	**14 - 21**	**22**	**23**	**24**
Reference horizon / constant depth (km)	Base Quaternary	Base Quaternary	Base Quaternary	0.062	Near BCU	0.14
Property along interface (km/s)	3.5	3.7	3.9	4.0	4.6	4.5
Constant gradient (km/s /km)	0.2	1.0	1.0	00.75	0.1	1.0
Sampling increment (km)	0.05	0.05	0.05	0.05	0.05	0.05

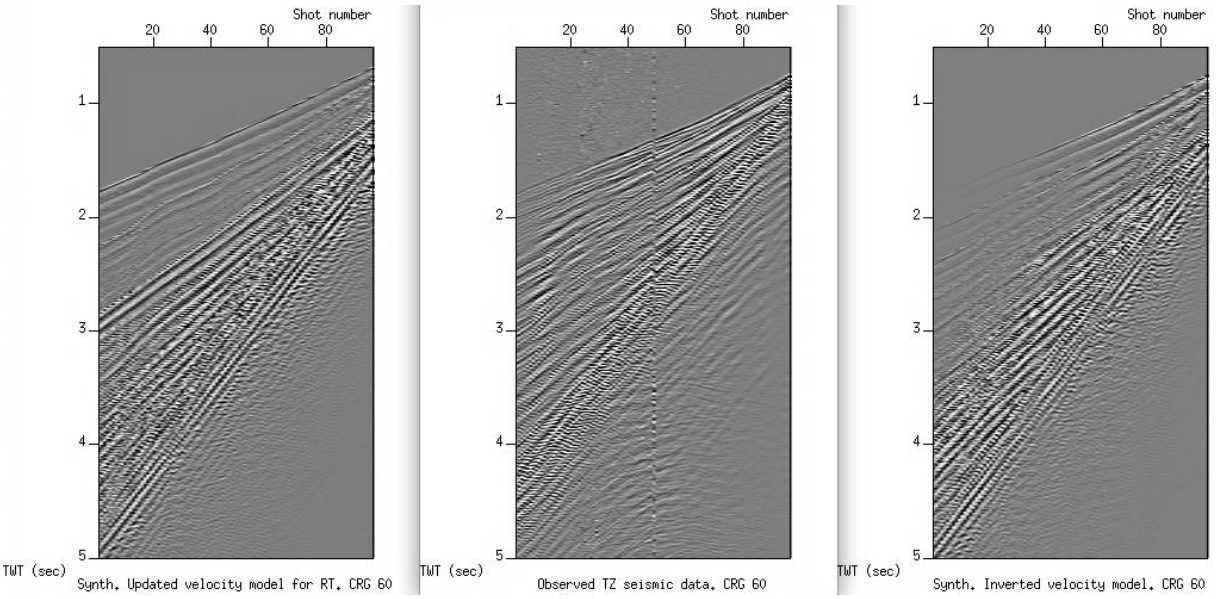

Figure 7.4: Comparison between synthetic data based on model M3 (left), observed TZ-seismic data (middle) and synthetic data based on the model Model M2 (right).

7.2 RT-based traveltimes

Having established an approximate match between the observed TZ-seismic data and the synthetic data generated by model M3, the model was utilized for RT modelling. Direct arrivals, P-wave reflections, converted S-wave reflections and multiple reflections were modelled and traveltimes of the various wave modes were generated. The most relevant results for each wave mode modelled is presented in the following sub sections.

The type of wave and how transmission / reflection occurs at interfaces is specified as ray codes by the user.

7.2.1 Direct arrivals (transmitted rays)

Direct arrivals in the context of RT refers to all rays that are transmitted at all interfaces they may encounter as they propagate through the subsurface. Direct P-wave arrivals were modelled to obtain traveltimes, study the raypaths, and determine the depth limit of the model by inspecting the extent to which rays propagate through the high velocity basement layer (Figure 7.5). Almost all the rays propagated through the Basement layer, except for a few rays from the near source-receiver offset which split into parts, and some part of the rays propagated through the sedimentary layers.

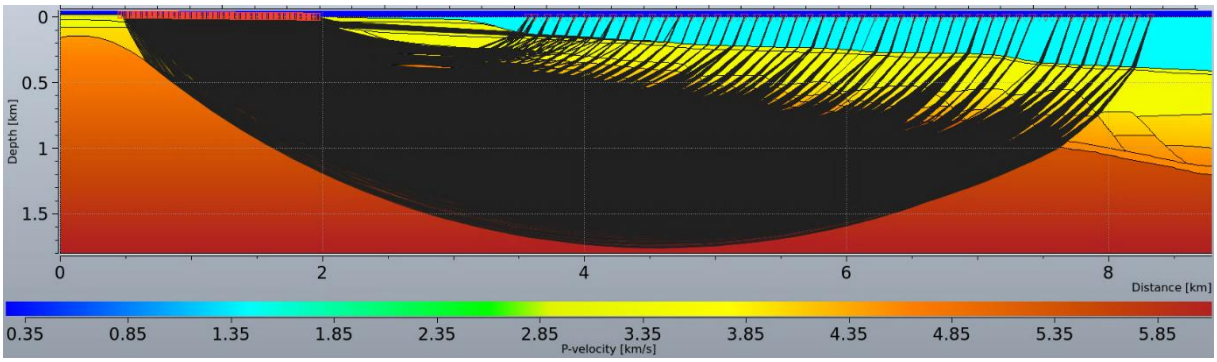

Figure 7.5: Raypath for direct P-wave arrivals.

7.2.2 Primary P-wave reflections

Primary P-wave reflections at all the interfaces were simulated to obtain traveltimes. Relevant results from the simulation will be presented in this section. It is important to note that head waves are not modelled in RT methods, hence the missing data (or gap) in the images presented in this section are due to incident rays reaching the critical angle but did not propagate further due to the limitation. The critical angle at each interface was calculated using Snell's law (equation (4.2). The critical angles are listed in Table 7.3; the velocities used in the calculation are average values obtained near the layer boundaries between 3.0 km to 5.5 km in the model. Note that the critical angles shown here are for normal-incident rays, and the values will vary with change in incident angle (section 8.3.1). Furthermore, the velocities are not constant in most of the layers, hence the critical angles at normal incidence will not be the same along the interfaces in the model.

Table 7.3: Critical angle at each interface computed with average velocity values obtained between 3.0 km to 5.5 km in the model.

INTERFACES	AVERAGE VELOCITY ABOVE (km/s)	AVERAGE VELOCITY BELOW (km/s)	CRITICAL ANGLE (°)
Seabed	1.5	3.4	26
Base Quaternary	3.4	3.5	76
Base Aptian	3.55	3.96	64
Base Barremian	4.02	4.23	72
BCU	4.26	4.43	74
Top Basement	4.46	5.04	62

1. Top Basement

Primary P-wave reflections from top Basement were simulated, however only about 31 % of the total shots consisting of some near- and far-offsets were recorded (Figure 7.6). The gap or missing data is due to the aforementioned limitation. Nevertheless, in some cases where velocity gradients are assigned to a given layer, with the overlying layer velocity lower than the velocity in the given layer, and both layers are separated by a flat (or relatively flat) interface, one can observe strongly refracted rays in the given layer. This is the case for the far-offset shots that successfully propagated through the top Basement interface where it is relatively flat, but this kind of refraction may not occur where the interface is dipping as applicable to top Basement interface at the mid-section area where the gap exists.

The rays from the far-offset shots exhibit a rather complex raypath. The rays appear to have refracted through the top Basement interface mimicking head waves, and then reflected from underneath top Basement. Figure 7.7 is an example of the complex raypath tracked from the farthest shot to their reflection points, and to the receivers. The rays from the near-offset shots are rays whose incident angles at top Basement interface exceeded the critical angle and were totally reflected. The traveltimes and incident angles for the successful P-wave reflections at top Basement interface are represented in Figure 7.8 and Figure 7.9, respectively. Note that the incident angles for the far-offset shots are incident angles at which the refracted rays hit the top Basement interface from underneath the interface. Usually, energy reduces with

propagation distance, hence the far-offset events will have low amplitudes relative to other reflections with shorter propagation distance as exemplified in Figure 7.10.

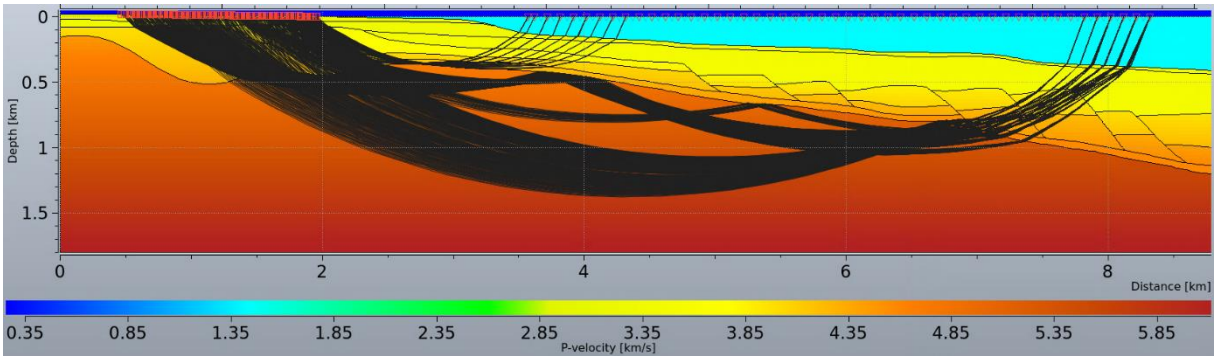

Figure 7.6: Raypaths for primary P-wave reflections from top Basement interface.

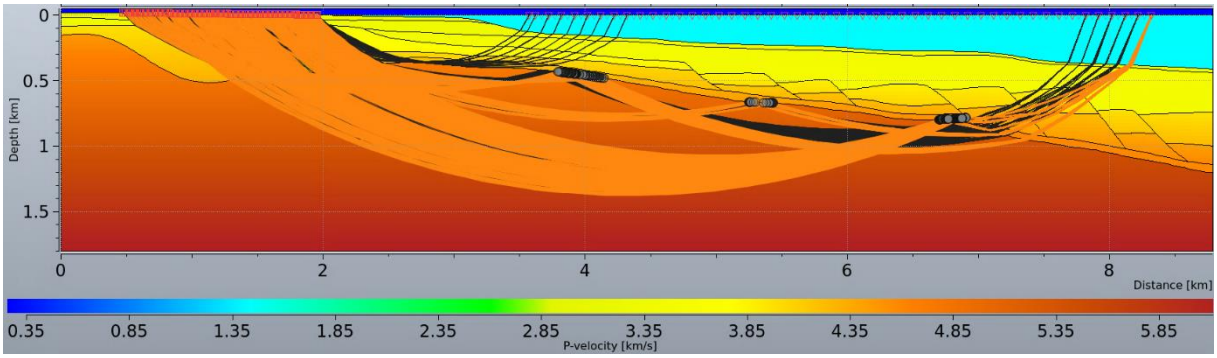

Figure 7.7: Raypath for primary P-wave reflection at top Basement for the farthest shot (highlighted in orange) to distinguish it from other raypaths (in black). Rays coming from the source splits into three parts and refracts through the Basement from where it then reflects from underneath the Basement at three separate areas. The reflection points are indicated by black circles.

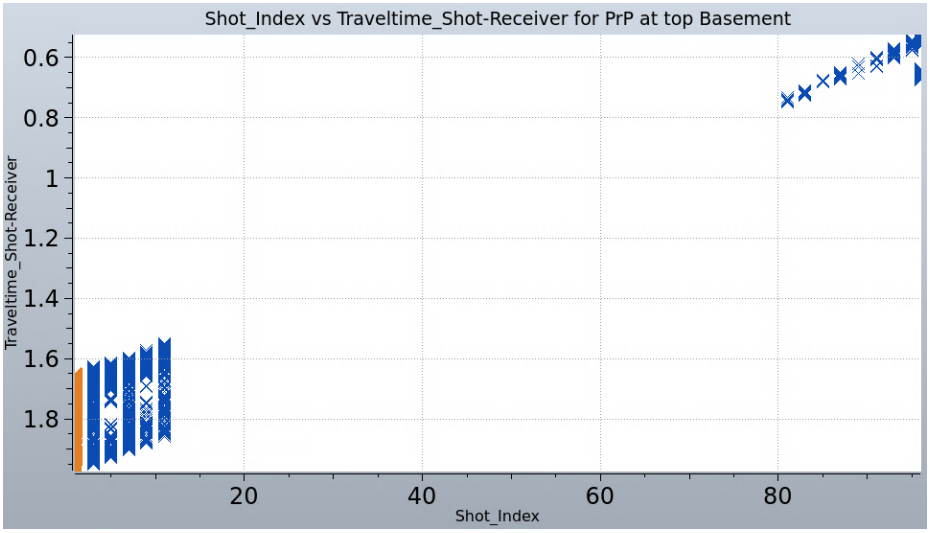

Figure 7.8: Traveltimes for primary P-wave reflections from top Basement. The highlighted points in orange represent the traveltimes for the farthest shot (raypath highlighted in orange in Figure 7.7).

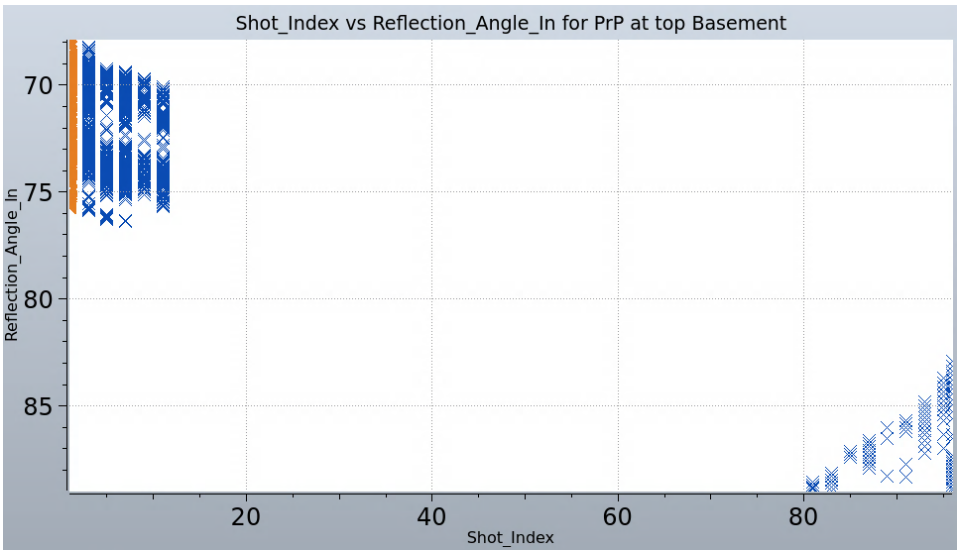

Figure 7.9: Incident angles for primary P-wave reflection at top Basement interface. The highlighted points in orange represent the incident angles for the farthest shot (raypath highlighted in orange in Figure 7.7). On the title, Reflection_Angle_in implies incident angle at reflection point.

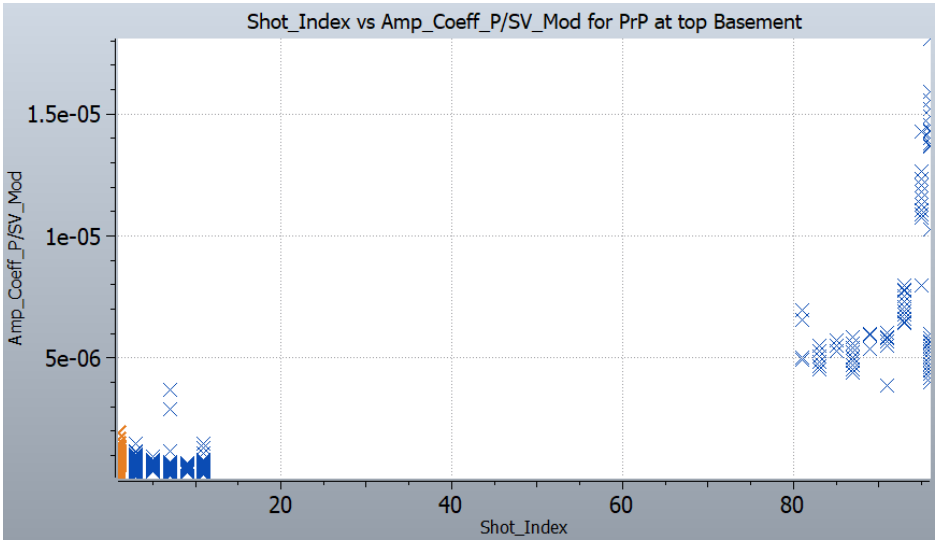

Figure 7.10: Amplitudes for reflected arrivals from top Basement. The highlighted points in orange represent the amplitudes for the farthest shot (raypath highlighted in orange in Figure 7.7).

2. BCU

Primary P-wave reflections from BCU were simulated and, however only about 27% of the shots were recorded. The characteristics of the P-wave reflections are similar to the P-wave reflections from top Basement. The two interfaces have almost similar dips except at the westernmost part of the model where the BCU interface is steeper than the underlying top Basement interface. The raypaths for the recorded primary P-wave reflections from BCU is represented in Figure 7.11. As is the case with top Basement, the gap in the middle is also associated with rays reaching the critical angle but unable to propagate as head waves. In addition, the area on BCU interface where rays coming from the far-offset shots propagated through and were strongly refracted is also relatively flat; the refracted rays also reflected from the underside of the BCU interface before arriving to the receivers. Only few near-offset shots were recorded, and the reason is also related to rays reaching the critical angle.

The traveltimes for primary P-wave reflection from BCU is represented in Figure 7.12. Given how close the top Basement and BCU interfaces are to each other in most part of the model, their traveltime range is almost the same and may be difficult to distinguish in the real TZ-seismic data.

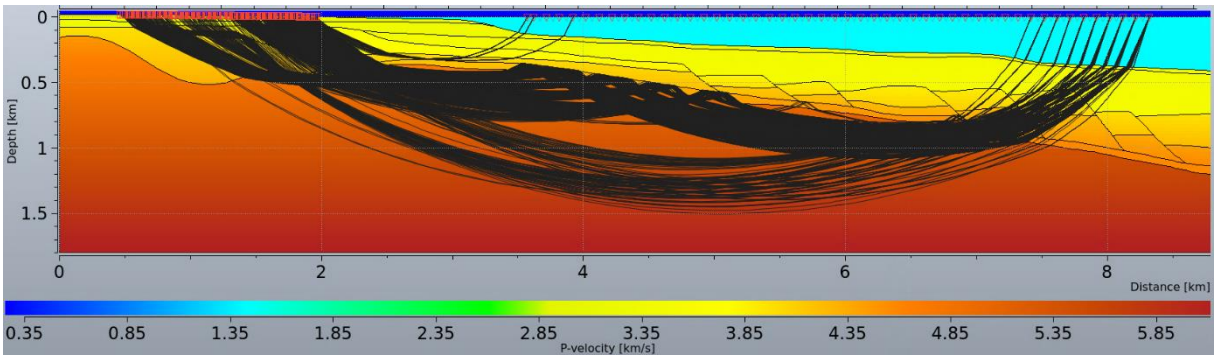

Figure 7.11: Raypaths for primary P-wave reflection from BCU.

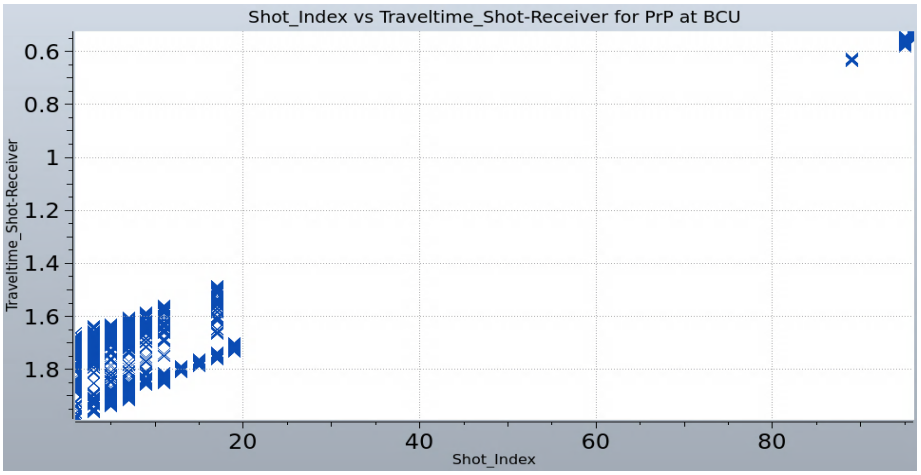

Figure 7.12: Traveltimes for primary P-wave reflections from BCU.

The few reflections from the near-offset shots have very high incident angles (close to 90°) as also observed with top Basement and they were all totally reflected, having exceeded the θ_c. There are two different raypaths from the far-offset arrivals characterized by different set of angles. The lower set of angles (53° – 60°) are from arrivals that reflected from the underside of the BCU interface, and the higher set of angles (67° – 70°) are from arrivals that reflected from the underside of the western flank of the BCU interface (Figure 7.13). The angles are shown in Figure 7.14.

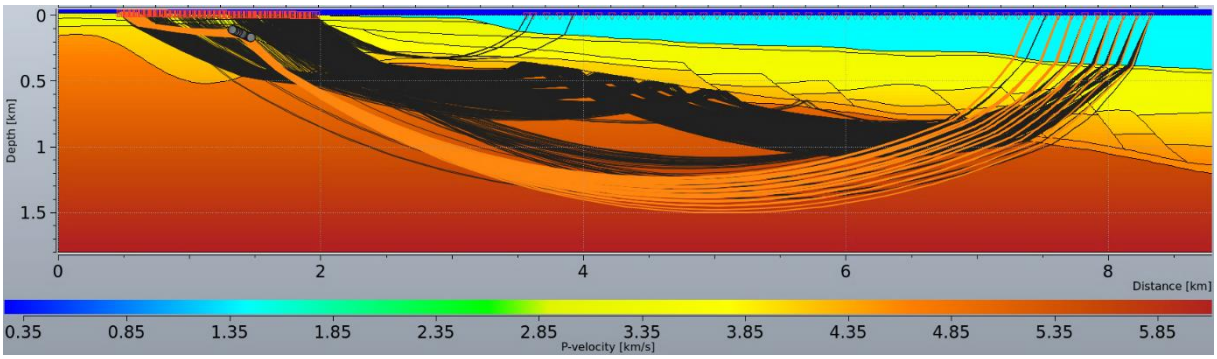

Figure 7.13: Raypaths for primary P-wave reflection from BCU, with raypaths from contributing source – receiver pairs (highlighted in orange) responsible for the reflection (black circles) at the western flank of the BCU.

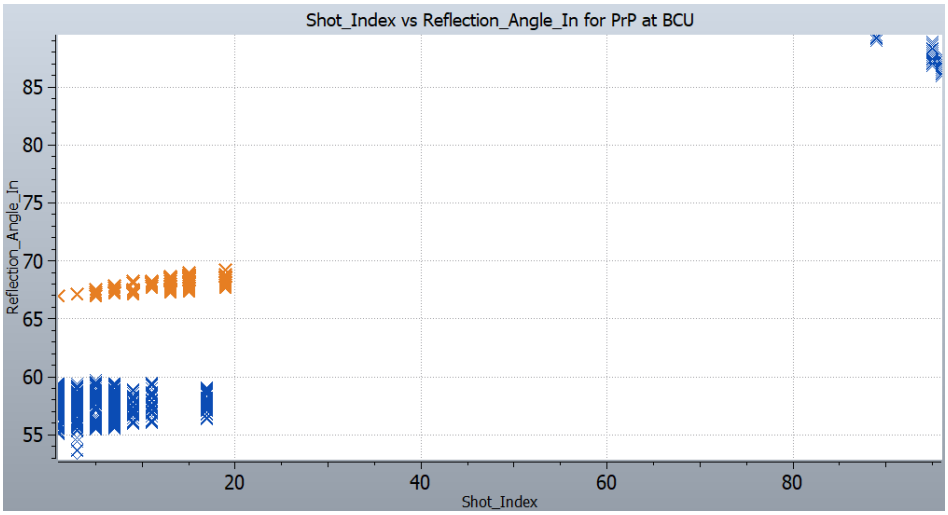

Figure 7.14: Incident angles for primary P-wave reflections at BCU interface. The highlighted points in orange represent the incident angles for reflections arriving from the eastern flank of BCU where the interface is steep (see Figure 7.13 for the raypaths). Reflection_Angle_in implies incident angle at reflection point.

3. Base Barremian

About 75% of the total shots were recorded for primary P-wave reflections from base Barremian. The base Barremian interface is relatively flat especially in the faulted area within the marine segment. These relatively flat area allowed more rays reaching the critical angle to be strongly refracted and generally followed the same complex reflection raypath observed in top Basement and BCU (Figure 7.15). However, between 1.6 km to 4.8 km, the interface has almost the same dip as BCU, hence the gap within this area can also be attributed to incident

rays impinging on the dipping part of the interface at critical angle. The near-offset incident ray angles are greater than the critical angle and thereby totally reflected as also observed in the underlying interfaces.

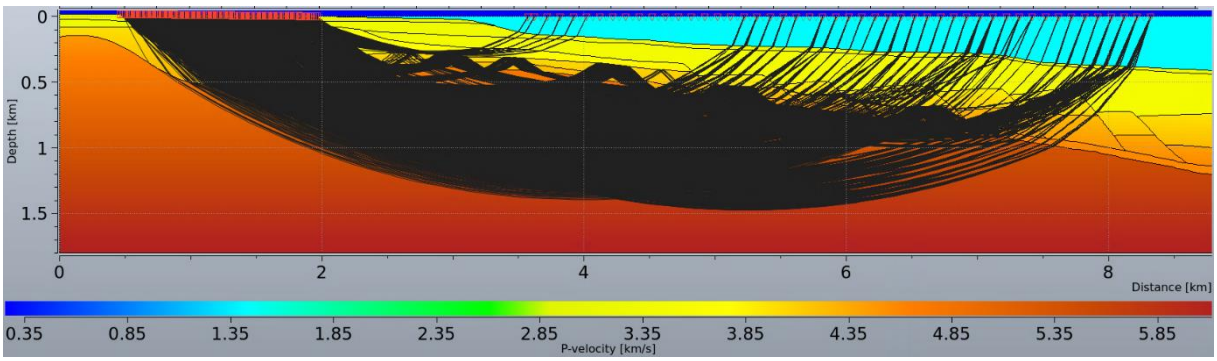

Figure 7.15: Raypaths for primary P-wave reflection from Base Barremian.

4. Base Aptian

For primary P-wave reflection from base Aptian, about 65% were recorded by the receivers. The raypaths show similar raypaths observed in the underlying interfaces (Figure 7.16). However, base Aptian is steeper than base Barremian at the near-offset area (between 2.4 km and 3.0 km) which corresponds to the nearly flat area on base Barremian interface where rays were totally reflected. Hence, the reason for the missing rays is connected to rays reaching the critical angle but unable to be transmitted as refracted waves within the dipping area, or incident ray angles at the reflector not exceeding the critical angle to be totally reflected as observed in the previous results.

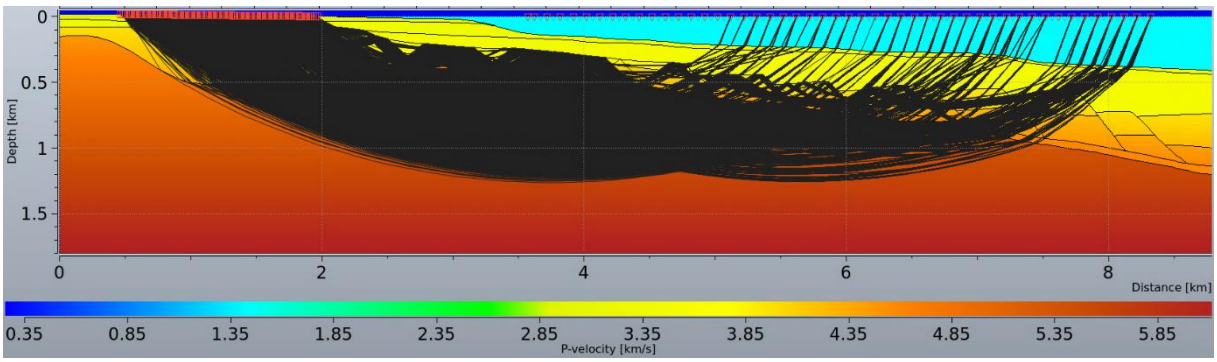

Figure 7.16: Raypaths for primary P-wave reflection from base Aptian.

5. Base Quaternary

Only very few shots (about 31%) were recorded for primary P-wave reflections at base Quaternary, and nearly half of the receivers at the western part of the receiver spread recorded no events Figure 7.17 (top). The same reason for the gap for the missing rays in for the underlying interfaces applies here.

The rays recorded by the receiver consist of only incident rays which impinged on the base Quaternary interface at angles which exceeded the critical angle and were thus totally reflected. Figure 7.17 (bottom) shows an example raypath for primary P-wave reflection from base Quaternary: because of the high velocity contrast between the water layer and the seabed, the ray is strongly refracted as it transmits through the seabed interface and hits the base Quaternary interface at a very high incident angle which exceeds the critical angle and total reflection occured. Figure 7.18 represents the incident angles for primary P-wave reflections at base Quaternary.

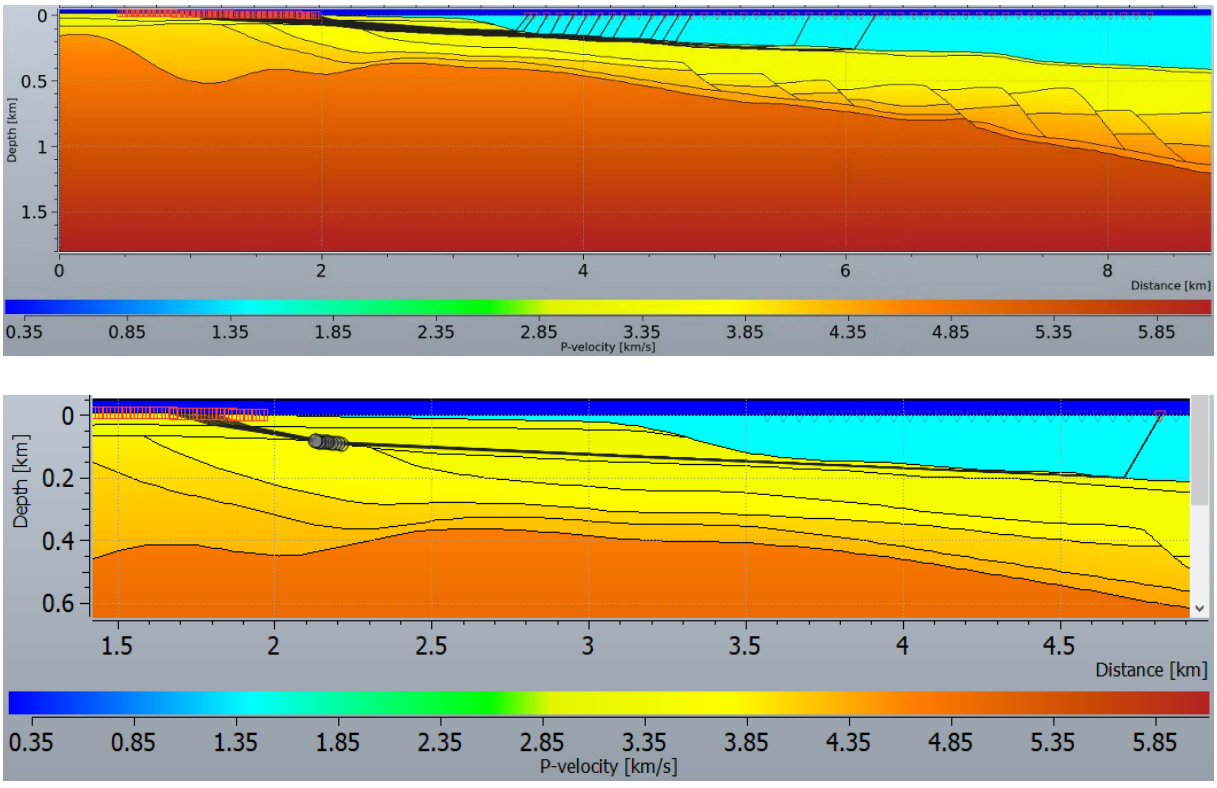

Figure 7.17: Raypaths for primary P-wave reflection from base Quaternary (top). Example raypath from a single shot showing strongly refracted rays at the water – seabed interface before reflecting at base Quaternary interface (bottom); the black circles represent the reflection points.

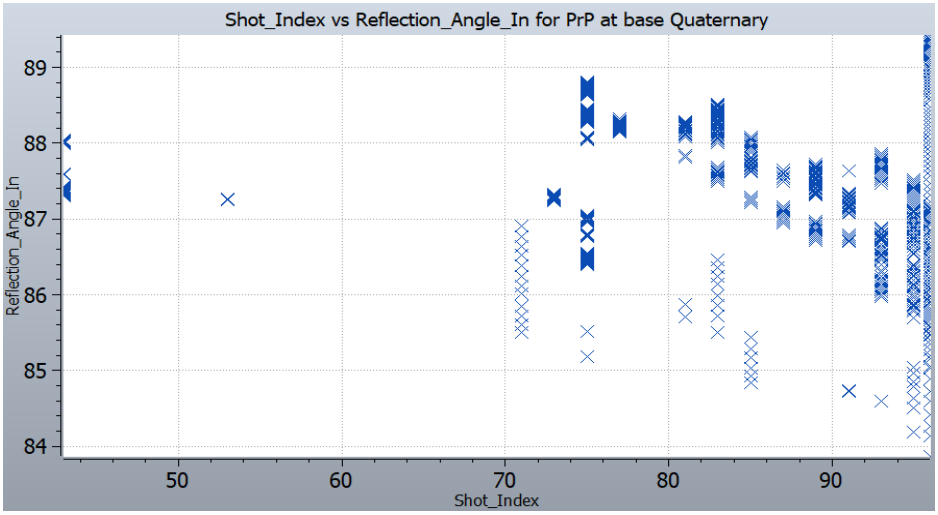

Figure 7.18: Incident angles for primary P-wave reflections at base Quaternary interface.

7.2.3 Converted S-wave reflections

Attempts were made to simulate mode-converted S-wave reflections, however only very few events from base Barremian and base Aptian were recorded. The number of arrivals is too low to make any significant input to the interpretation of the TZ-seismic data. The raypaths for the modelled converted S-wave reflections from base Barremian and base Aptian are shown in Figure 7.19. Mode-converted S-waves at the seabed were also modelled (i.e., P-waves transmitted as S-waves at the seabed). Events were recorded in this case because rays were defined to transmit only, and the receivers are on land, hence receiving S-waves (Figure 7.20).

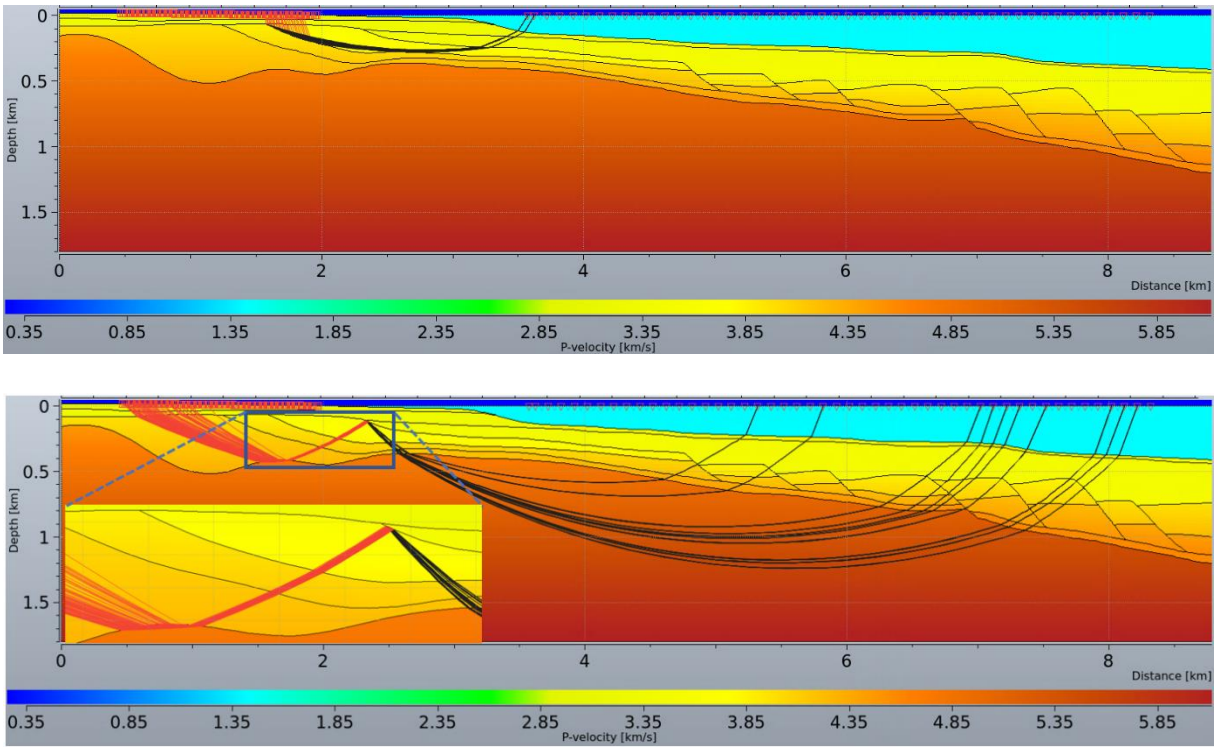

Figure 7.19: Raypaths for converted S-waves at base Barremian interface (top) and base Aptian interface; with magnified area of the model showing the P-wave (black lines) to S-wave (red lines) conversion point from underneath base Aptian and the propagation path along the top Basement interface before proceeding to the receiver (bottom).

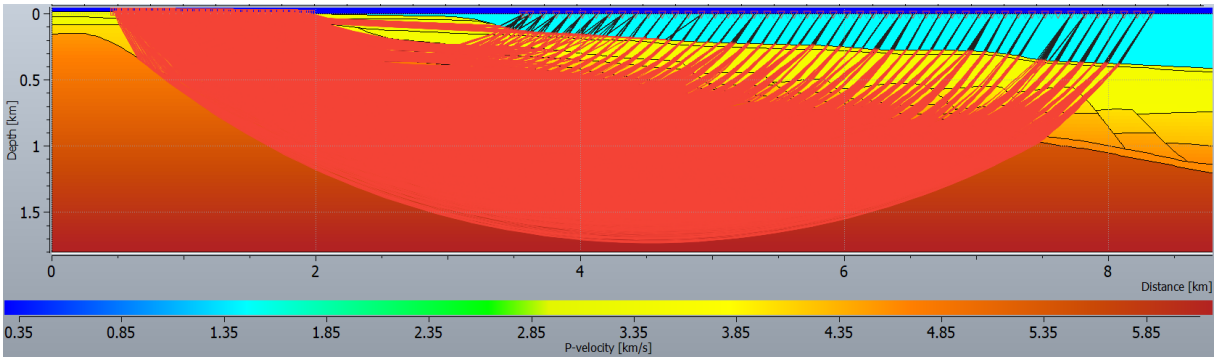

Figure 7.20: Converted S-wave transmission (direct converted S-wave arrival). The intersection points between the black and red lines indicate the conversion point from P- to S-waves at the seabed interface.

7.2.4 Multiple reflections

Multiple reflections are seismic events that have undergone more than one reflection (Sheriff and Geldart, 1995). Given the geometry and velocity structure of the study area, strong multiple reflections are expected; especially between interfaces where strong *Impedance constrast* exist (i.e., MSL, seabed and top Basement). Therefore, multiple reflections between these interfaces with strong *Impedance constrast* were simulated.

1. **Multiple P-wave reflection (seabed – MSL)**

Multiple P-wave reflections from the seabed were simulated. The raycode was defined for reflections to occur in the following order: seabed - sea surface – seabed. In the examples represented in Figure 7.21, the multiple reflection raypaths are between the seabed and MSL; with the top figure representing rays that reflected twice from the seabed and the bottom figure representing rays that reflected three times from the seabed. In both simulations, the final reflection raypaths for far- to mid-offsets; having reached the critical angle (26°), refracted through the seabed and followed the shortest raypath (i.e., through the basement) to the receivers. However, this is not the case for the near offsets where the final incident rays on the seabed have exceeded the critical angle and were totally reflected.

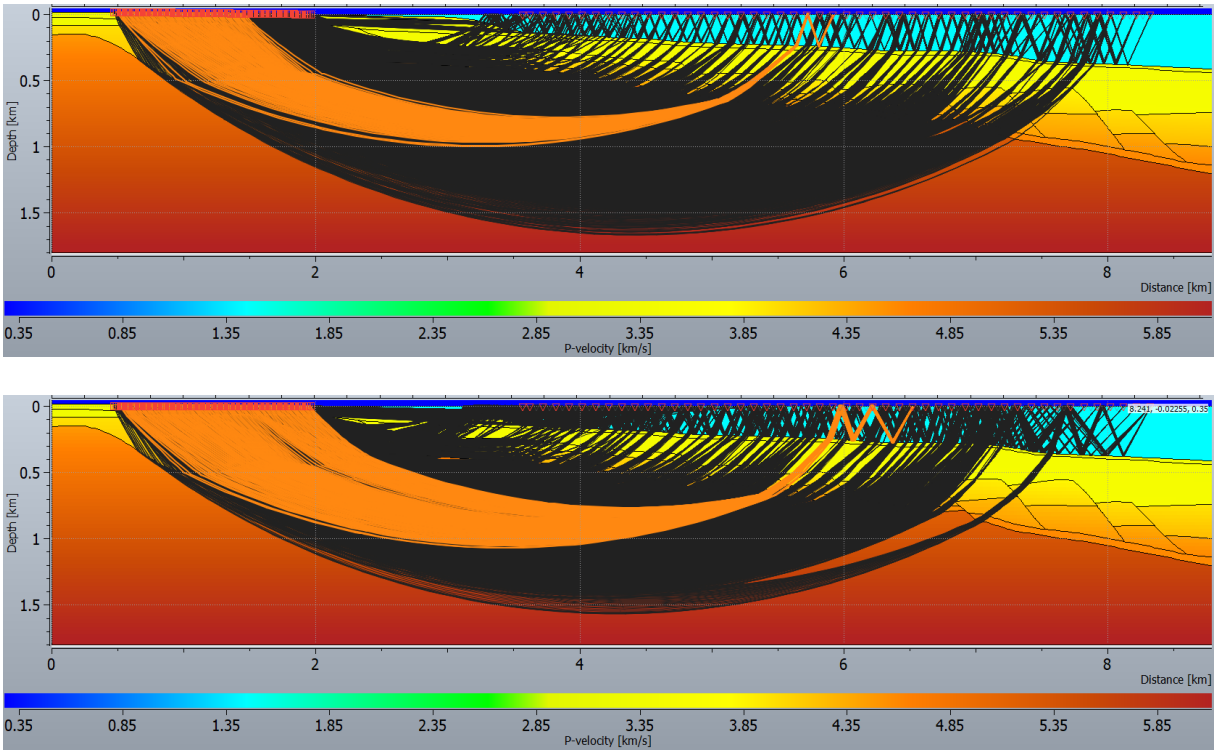

Figure 7.21: Raypaths for multiple P-wave reflections showing rays that have reflected two twice from the seabed (top) and rays that have reflected three times from the seabed (bottom). Highlighted in orange are the raypaths tracked from a single shot to the receivers.

2. Multiple P-wave reflection (top Basement - MSL)

Multiple P-wave reflections from top Basement (i.e., between top Basement and MSL) were simulated. The raypaths are represented in Figure 7.22. The top figure represents rays that reflected twice from top Basement and the bottom figure represents rays that reflected three times from top Basement. In both simulations, the same complex raypath observed in the primary P-wave reflections is also observed for the first set of reflections here. Similarly, the gap in the middle is also related to rays reaching the critical angle but unable to propagate as head waves. It is noteworthy that there are several multiple reflection points concentrated along the TZ.

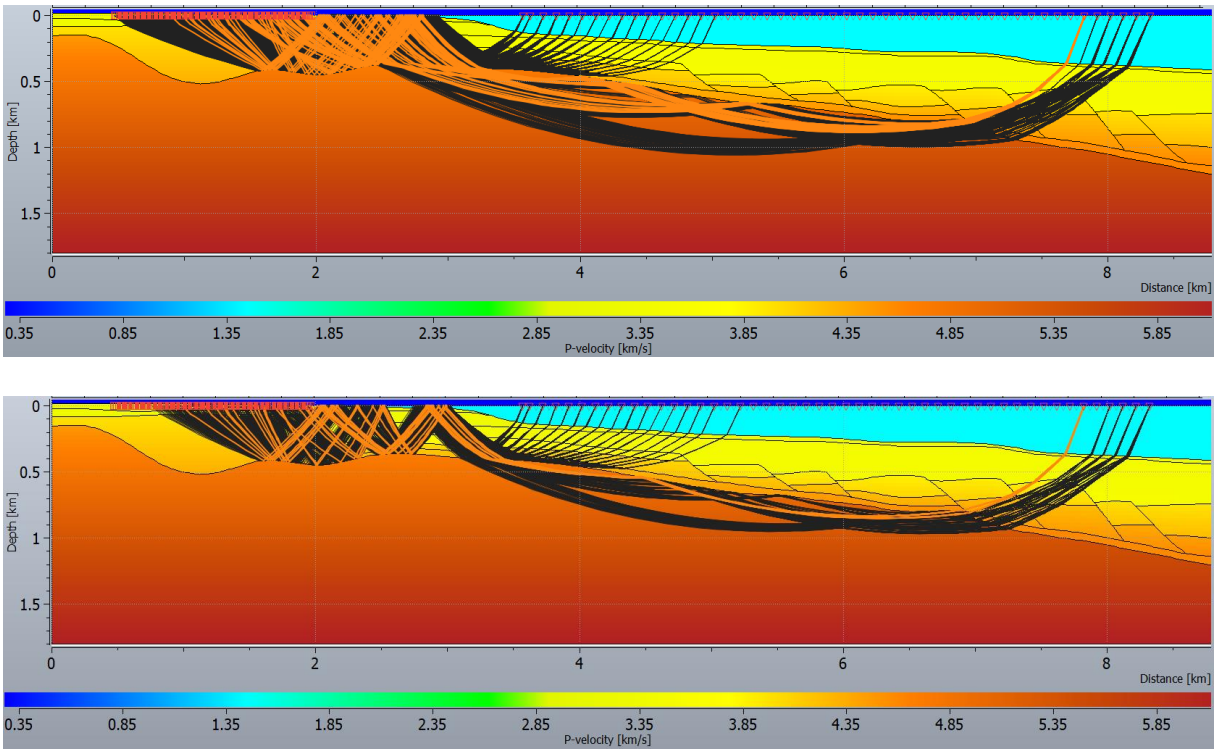

Figure 7.22: Raypaths for multiple P-wave reflections showing rays that have reflected twice from top Basement (top) and rays that have reflected three times from top Basement (bottom). Highlighted in orange are the raypaths tracked from a single shot to the receivers.

3. Multiple P-wave reflections (seabed – MSL) transmitted as converted S-waves

Converted S-waves were not left out in the multiple simulation. Figure 7.23 represent raypaths for multiple P-wave reflections from the seabed which converted to S-waves in the final phase of incidence at the seabed and propagated as S-waves through the seabed interface as a result of the incident rays reaching the critical angle.

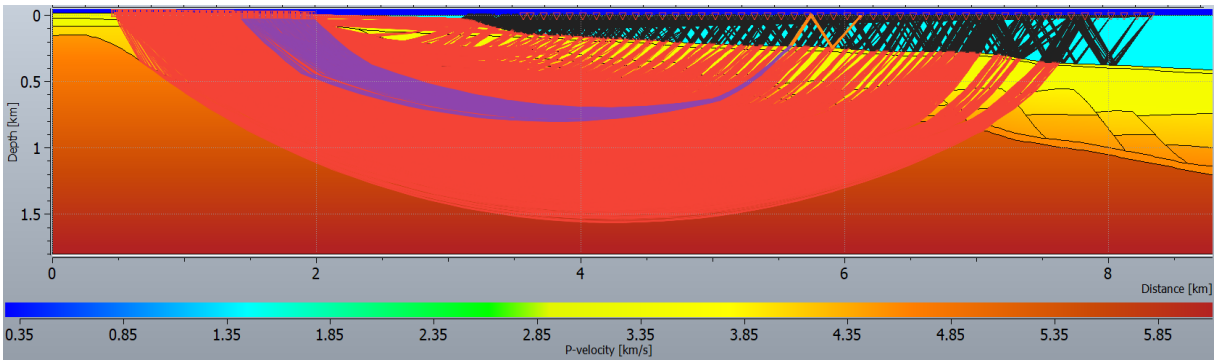

Figure 7.23: Raypaths for multiple P-wave reflections from seabed which finally converted to S-waves before propagating to the receivers.

7.3 RT-based traveltimes on observed TZ-seismic data and synthetic data

RT-based traveltimes for the various wave modes simulated were extracted and superimposed on the TZ-seismic data and FD-based synthetic datasets in an effort to identify the events observed in the TZ-seismic data. It is important to state that the gaps in the traveltime curves are mostly related to incident rays which have reached the critical angle but did not propagate as head waves, given that the latter are not modelled in RT methods (Gjøystdal et al., 2002).

1. Primary P-wave reflections

Primary P-wave reflections at the interfaces in the model were simulated. Traveltimes were extracted and superimposed on the observed TZ-seismic data and synthetic datasets for possible event identification. Figure 7.24 shows an example using CRG 1. It is difficult to confidently match the RT-based P-wave reflection traveltimes with any event in the observed TZ-seismic data and the synthetics computed with model M2. The events are also very close to each other except for base Quaternary which separates from the other events with offset distance. It can also be observed that the reflection traveltimes from shallower interfaces in the model appear as later events in time than deeper interfaces.

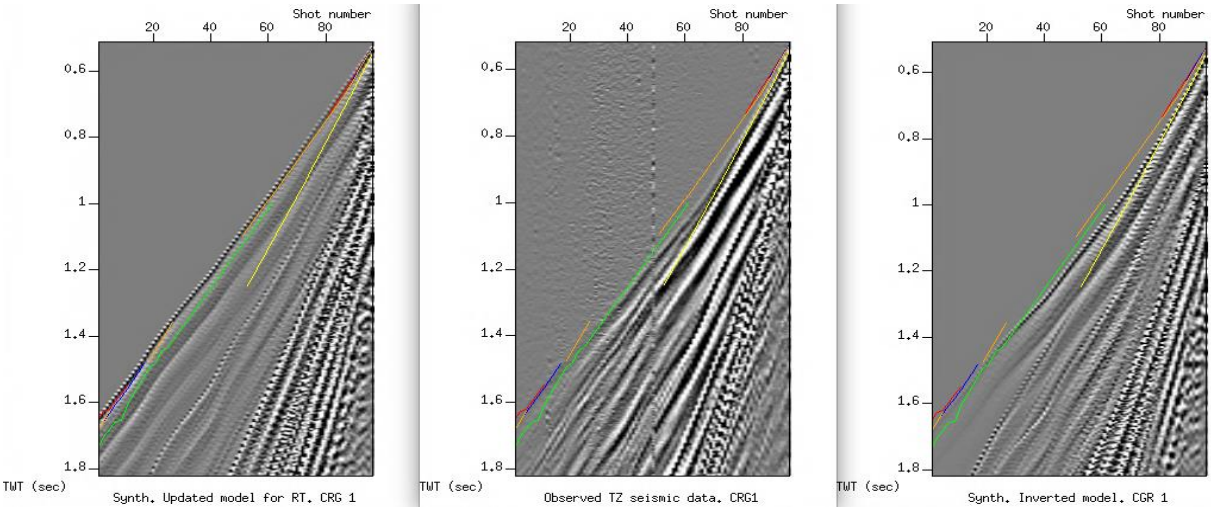

Figure 7.24: Primary P-wave reflection traveltimes superimposed on the synthetics computed with model M3 (left), observed TZ-seismic data (middle) and the synthetics computed with model M2 (right). The primary P-wave reflection traveltime curves are from top Basement (red), BCU (blue), base Barremian (orange), base Aptian (green) and base Quaternary (yellow).

2. Converted S-waves at the seabed

Traveltimes for P-waves converted as S-waves at the seabed interface before propagating to the receivers were extracted. The raypath for the converted S-waves is represented in Figure 7.20. An example of the converted S-wave traveltimes overlain on the observed TZ-seismic data and synthetic datasets using CRG 1 is represented in Figure 7.25. The converted S-wave curve fits an event perfectly in the synthetics computed with model M3 as expected; however, the event is missing in the synthetics computed with model M2. In the observed TZ-seismic data, there appears to be a relatively strong event that closely follows the converted S-wave curve from about 0.8 s to about 1.65 s, but beyond this interval, the event deviated slightly from the curve but generally maintained the same moveout. It is challenging to identify the converted S-wave in the TZ-seismic data with absolute certainty, given how close the events are to each other. However, converted S-waves in the observed TZ-seismic data are expected along or close to the RT-based converted S-wave curve.

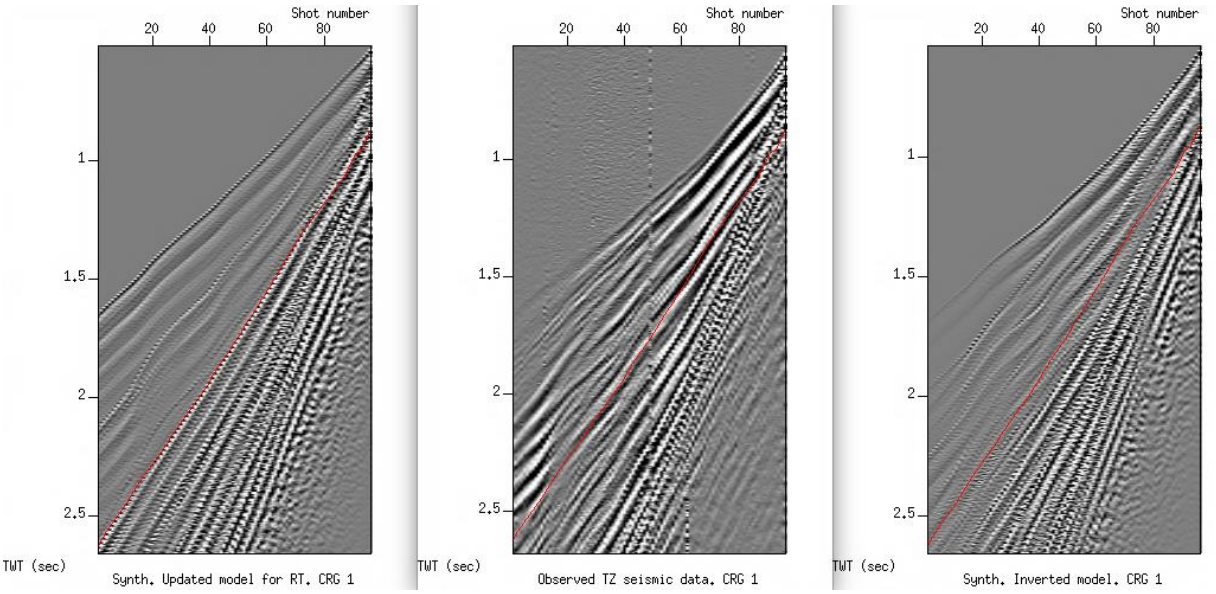

Figure 7.25: Traveltimes for P-waves converted to S-waves at the seabed interface (red line) overlain on the synthetics computed with model M3 (left), observed TZ-seismic data (middle) and the synthetics computed with model M2 (right).

3. Multiple reflection (seabed – MSL)

Given the strong impedance constrast at the water - seabed interface, strong multiples are expected in the observed data. Traveltimes for multiple P-wave reflections at the seabed were simulated and extracted for identification in the real and synthetic datasets. The ray code for the two traveltime sets presented here consists of P-wave energy which reflected in the following order before recorded by the receiver: seabed – MSL – seabed, and seabed – MSL – seabed -MSL - seabed (see Figure 7.21 for example raypath). Figure 7.26 displays a plot of the multiple P-wave reflection overlain on the observed TZ-seismic data and synthetic datasets using CRG 1 as an example. The two set of seabed multiple reflection traveltimes appears to fit perfectly with two events in the synthetics computed with model M3 as expected. In the TZ-seismic data, the traveltimes of the multiple reflection which reflected twice from the seabed (red curve in Figure 7.26) fits perfectly with a strong event with a polarity reversal about 20 ms below the curve. On the other hand, the traveltimes for the multiple reflection which reflected three times at the seabed as described above (green curve in Figure 7.26) appears to fit a continuous event between 1 s to 2.1 s and therefrom, approximately follows the moveout of the discontinuous events. In the synthetics computed with model M2, the events within the time window of the traveltime curves are weak, but similar moveout of events near the traveltime curves can be observed.

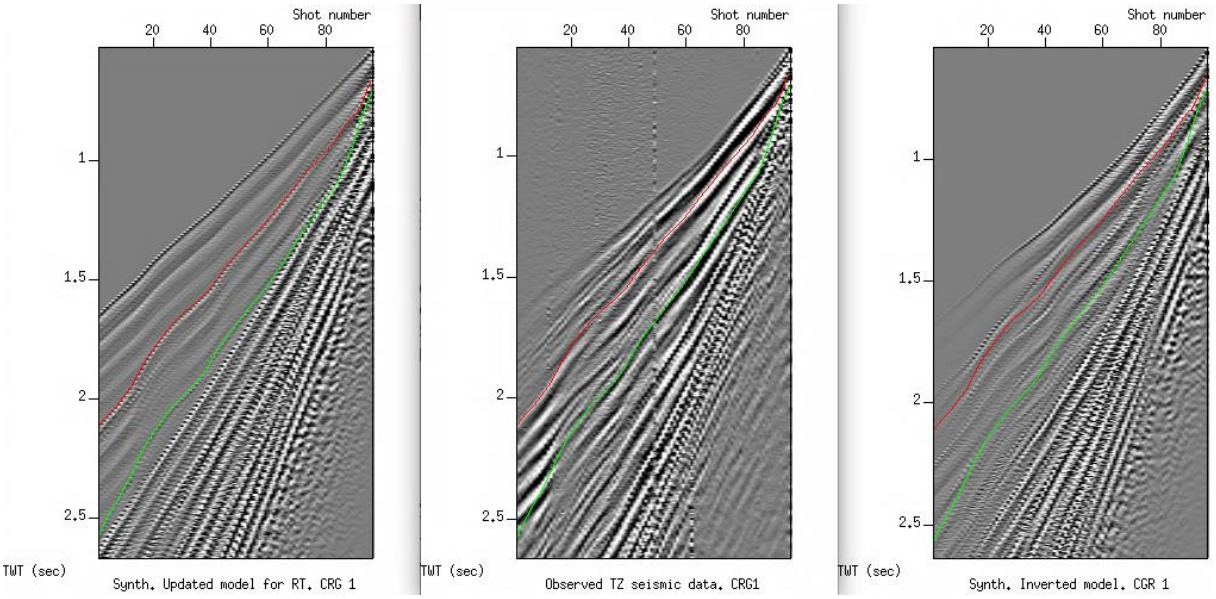

Figure 7.26: Traveltimes for multiple P-wave reflections which reflected in the following order: seabed – MSL – seabed (red), and seabed – MSL – seabed – MSL - seabed (green) superimposed on model M3 (left), observed TZ-seismic data (middle) and model M2 (right).

4. Multiple reflection (top Basement – seabed)

The traveltimes for multiple reflections at top Basement interface were also simulated. The simulation was performed for P-wave energy which have reflected in the following order: top Basement – seabed – top Basement, and top Basement – seabed – top Basement, seabed – top Basement. Figure 7.27 displays a plot of the top Basement multiple traveltimes overlain on the TZ-seismic data and synthetic datasets using CRG 1 as an example. As explained in the previous sections, the gap in the traveltime curves is due to missing data associated with rays reaching the critical angle at the top Basement interface but unable to transmit due to the aforementioned limitation.. The two traveltime curves appear to fit with two events in the synthetics computed with model M3 as expected, although the events appear weak. In the TZ-seismic data and the synthetics computed with model M2, the traveltime curves seem to fit approximately with two strong events; especially in the TZ-seismic data. Note that the raypath for the first-arrival traveltimes is different from the raypath of the multiples, hence the obvious difference in first-arrival traveltimes at near- to mid-offsets between the synthetics computed with model M3 and the TZ-seismic data may not maatter in evaluating the multiple events.

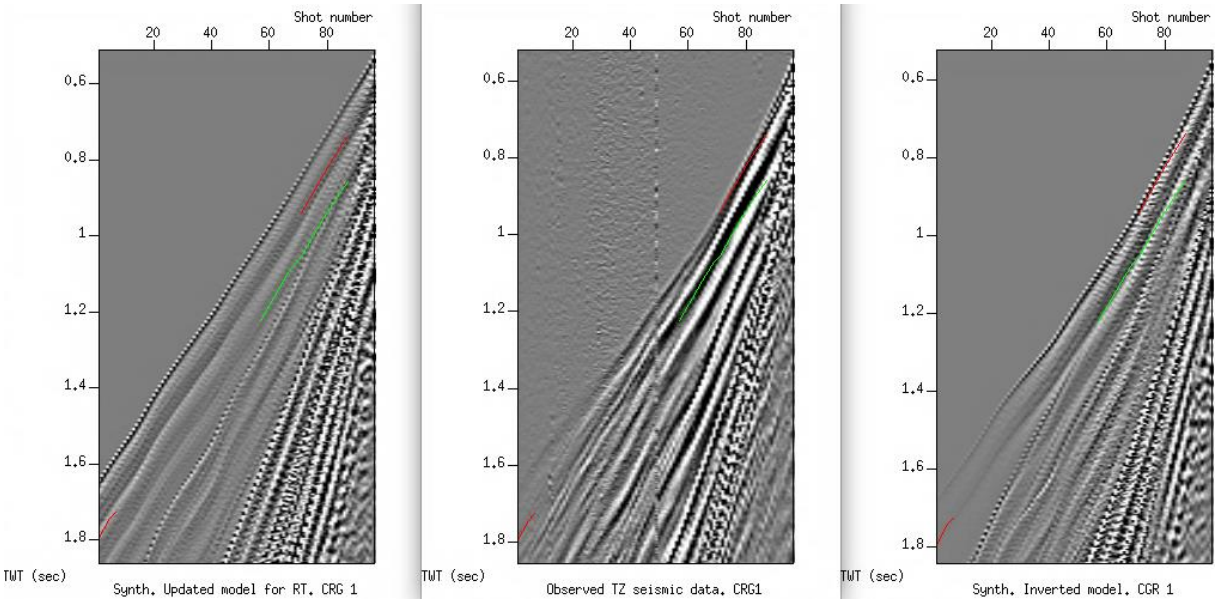

Figure 7.27: Traveltimes for multiple P-wave reflections which have reflected in the following order: top Basement – seabed – top Basement (red), and top Basement – seabed – top Basement, seabed – top Basement (green) overlain on the synthetics computed with model M3 (left), observed TZ-seismic data (middle) and the synthetics computed with model M2 (right).

5. Multiple reflection (top Basement – MSL)

The traveltimes for multiple reflections at top Basement interface (from MSL) were simulated. Ray codes were defined for two sets of multiples which reflected in the following order before recorded by the receivers: top Basement – MSL – top Basement, and top Basement – MSL – top Basement - MSL – top Basement. Figure 7.28 displays a plot of the traveltime curves overlain on the TZ-seismic data and synthetic datasets using CRG 1 as an example. The traveltime curves do not exactly fit any event in the synthetics computed with model M3, although the red curve closely follows an event which is most likely related the top Basement – seabed multiple presented in the previous section. In the TZ-seismic data and the synthetics computed with model M2, the traveltime curves appear to fit some strong events. However, the traveltime curves may not be ascribed to these events, given that in real data this type of multiple will have lower amplitudes in comparison to other multiples due to its longer raypath.

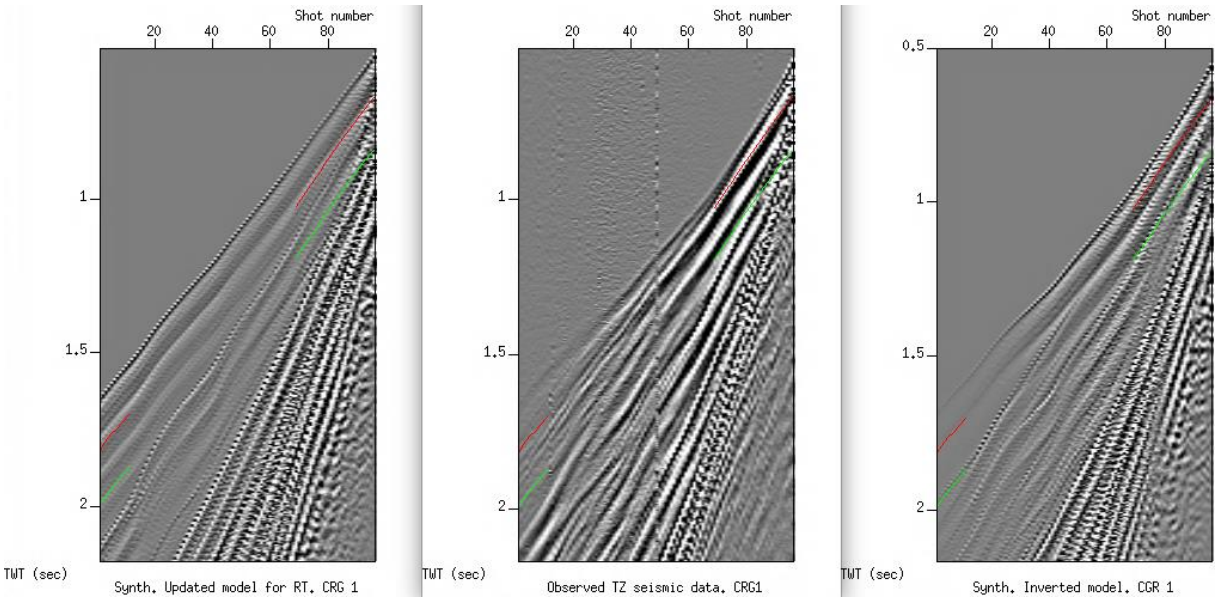

Figure 7.28: Traveltimes for P-wave multiple reflections which have reflected in the following order: top Basement – MSL – top Basement (red) and top Basement – MSL – top Basement - MSL – top Basement (green) overlain on the synthetics computed with model M3 (left), observed TZ-seismic data (middle) and the synthetics computed with model M2 (right).

6. Multiple P-wave reflection (seabed– MSL) converted to S-waves

Traveltimes for P-wave multiple reflections at the seabed (seabed – MSL – seabed, and seabed – MSL – seabed - MSL - seabed) which converted to S-waves were simulated. Figure 7.29 displays a plot of the traveltime curves overlain on the TZ-seismic data and synthetic datasets using CRG 1 as an example. The two traveltime curves appear to fit two events in the synthetics computed with model M3. In the TZ-seismic data and the synthetics computed with model M2, the traveltime curves appears to approximately fit two events and generally follows the moveout of events.

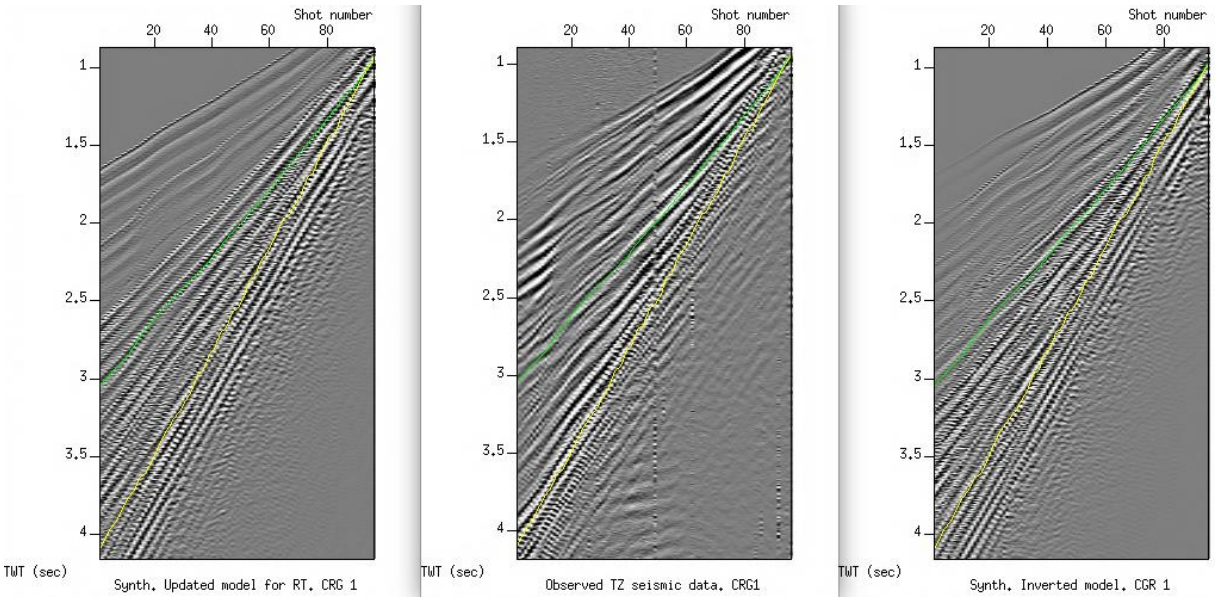

Figure 7.29: Traveltimes for P-wave multiple reflections which converted to S-waves after reflecting in the following order: seabed – MSL - seabed (green) and seabed – MSL – seabed - MSL - seabed (yellow) are superimposed in the synthetics computed with model M3 (left), TZ-seismic data (middle) and the synthetics computed with model M2 (right).

7.4 Experimental survey geometry

An experimental survey geometry was tested to evaluate the feasibility of improving the subsurface mapping of top Basement along the TZ. In this experimental survey setup, the shots were left as it was in the original survey, but the receivers were extended eastwards, including along the TZ on the seabed (Figure 7.30). The receivers were extended such that the minimum source-receiver offset is about 70 m. The receiver interval of 12.5 m was maintained as it was in the original survey.

Primary P-wave reflection from top Basement was simulated using the experimental survey. The reflection point coverage at top Basement using the experimental survey and the original survey were compared. The reflection coverage at top Basement seems to be improved with the experimental survey, especially along the TZ (Figure 7.31), and most of the gaps in reflection coverage observed with the original survey appears to be filled with the experimental survey. Additionally, by extending the receivers eastwards and slightly into the shallow marine segment (on the seabed) as was done in the experimental survey; only few near-offset shots may be necessary to map top Basement along the TZ (Figure 7.32). Furthermore, converted S-wave reflections from top Basement along the TZ can also be acquired (Figure 7.33) and only few near-offset shots are required as well.

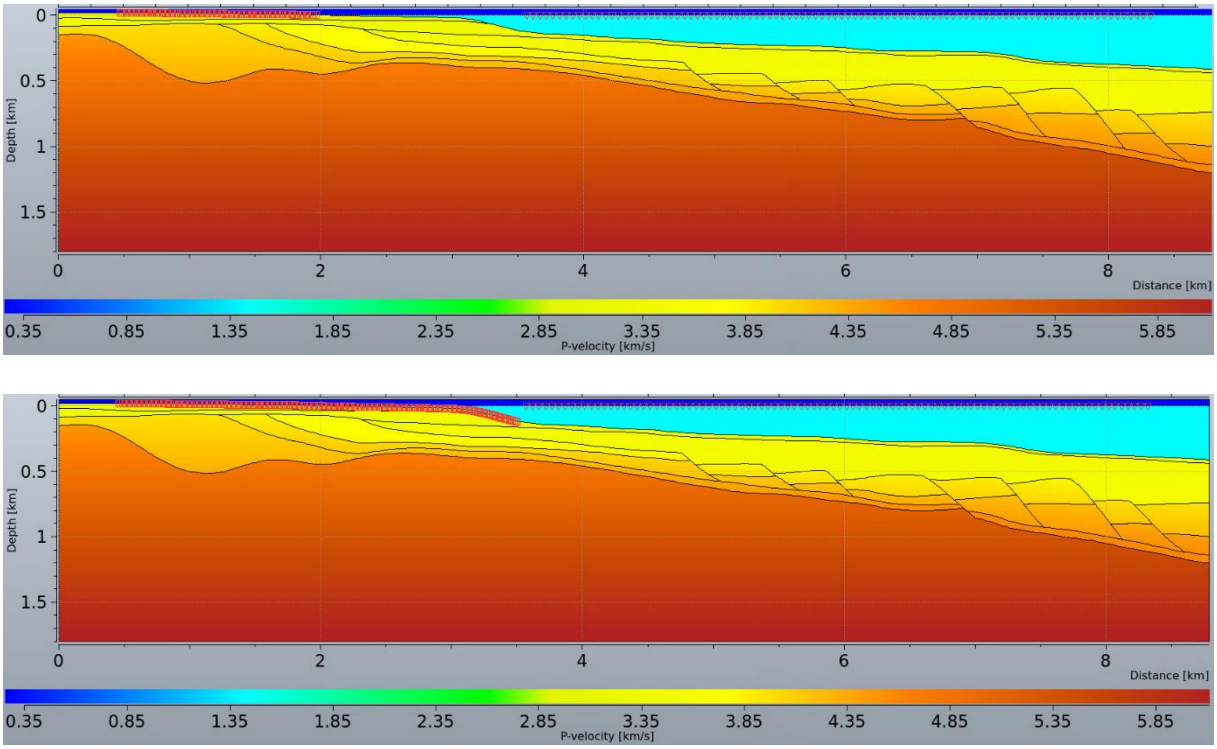

Figure 7.30: Original survey (top), and experimental survey (bottom) as defined in NSS. The receivers are to the top left and the shots are to the top right.

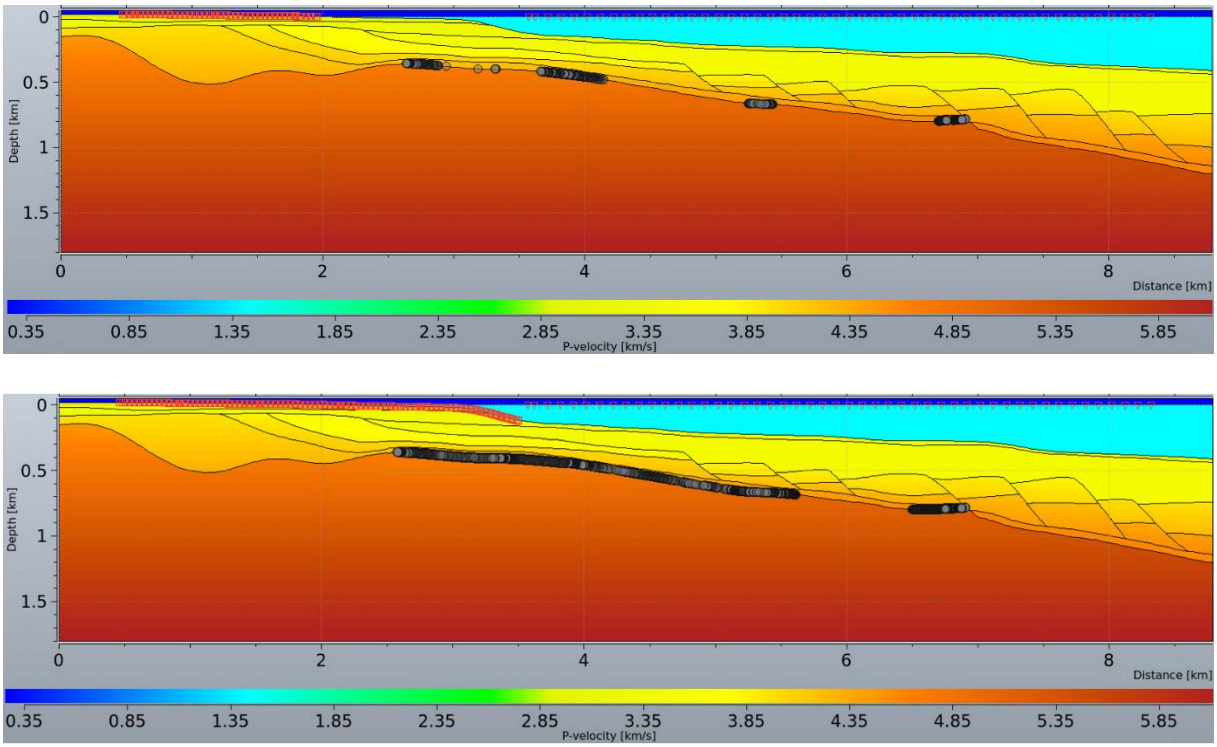

Figure 7.31: Reflection coverage of original survey (top) and experimental survey (bottom). The black circles represent the reflection coverage.

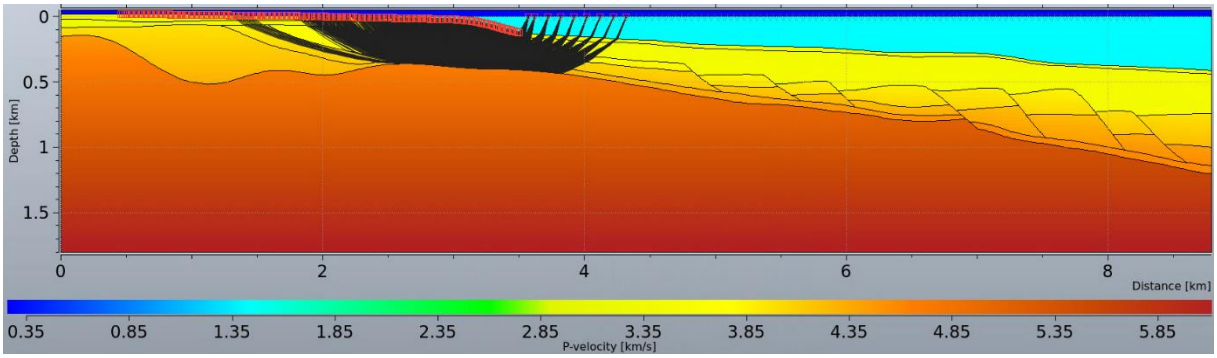

Figure 7.32: Near-offset shots contributing to most of the reflections at top Basement along the TZ.

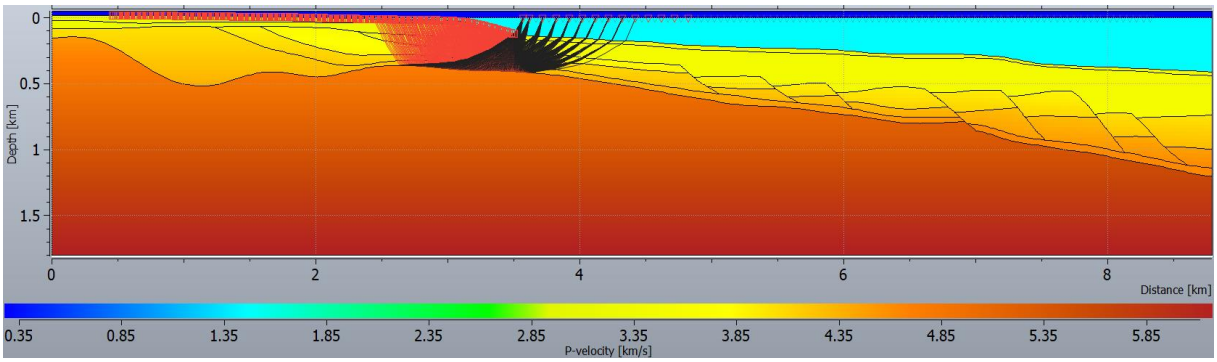

Figure 7.33: Converted S-waves upon reflection at top Basement.

Chapter 8: Discussion

The main aim of this present work is to use seismic modelling to analyse a TZ-seismic data acquired from Ramså Basin, and to propose other acquisition alternatives for better imaging of the subsurface target. Two different modelling approaches (RT and FD) were employed for this purpose. This chapter presents a general evaluation of the TZ-seismic data based on the modelling results. It begins with a brief overview of previous works and how it relates with this present study. Secondly, some key concepts associated with the seismic method applicable to this study will be introduced. Thirdly, the TZ-seismic data itself will be evaluated based on their first-arrivals. This will be followed by a brief assessment of the velocity models and a critical evaluation of the TZ-seismic data based on the modelling results. Lastly, the limitations of this present study will be discussed.

8.1 Comparison to previous work

Most TZ-seismic data have been acquired using various survey configurations to achieve objectives related to one or several of the following: bridge the gap between marine and land seismic data, geotechnical investigation of basement rocks, oil exploration, and reservoir characterization (Stucchi et al., 2003; Aouad et al., 2012; Wyman and Ahmad, 2013; Roberts and FitzPatrick, 2015; Brönner et al., 2017; Masoli et al., 2020). The TZ-seismic survey geometry in this present study falls into the category of the seismic method known as wide aperture reflection and refraction profiling (WARRP) which utilizes the information of both wide-angle reflected waves and refracted or diving waves (Makris et al., 1999). Diving waves are waves whose raypaths are curved due to a linear increase in velocity with depth (Levin, 1996). Basically, the term wide-angle refers to arrivals from far source-receiver offsets capable of generating diving waves, or arrivals from wide-angle reflections approaching or beyond the critical angle (White, 2012).

The WARRP method is utilized for general crustal studies in many locations and along TZs (e.g., Mjelde et al., 1993; Raum et al., 2002; Ruiz et al., 2017; Liu et al., 2015; 2017; Shulgin et al., 2018) primarily to obtain subsurface velocity information using refracted or diving waves (Mjelde et al., 1993; White, 2012; Chowdhury, 2020). The seismic sources commonly used in WARRP are airguns for offshore operations and explosives or vibroseis for onshore operations. For whole crustal studies, ultralong seismic recording units which consists mostly of geophones onshore and three-component ocean bottom seismographs (OBS) offshore are

common (Makris et al., 1999; e.g., Mjelde et al., 1993; Raum et al., 2002; Ruiz et al., 2017; Liu et al., 2015; and Shulgin et al., 2018). The advantage of using a seabed receiver such as OBS is that S-waves can be recorded on the horizontal component of the seismometer in addition to P-waves (White, 2012). The profile can be several hundred kilometres long (including along TZs) with ample spacing between the OBS / onshore geophones (e.g., Shulgin et al., 2018).

The TZ seismic data in this present study was acquired with geophones positioned on land and airguns firing from the sea (OBS data were not acquired). Although the source – receiver offset of the TZ-seismic data is in the range of 1.5 to 7.8 km, it is sufficient to generate wide-angle reflections and refracted or diving waves given that the depth of investigation is relatively shallow. A crude rule-of-thumb is that offsets of four to five times the target depth are required to record diving waves from the target (White, 2012).

As is the case in this present work, most wide-angle data requires seismic modelling for better understanding of the data. The subsurface structure used in the modelling is usually obtained from reflection seismic data where they exist, and velocities are estimated from the wide-angle refraction seismic data. The validity of the velocity model is then checked by comparing synthetic seismograms based on the velocity model with the real data. In many cases, as applied in this present work, seismic traveltime tomography may be required to obtain a better velocity model (e.g., Raum et al., 2002; Liu et al., 2015; Ruiz et al., 2017; Shulgin et al., 2018). If a reasonable match is established between the modelled synthetic data and real data, the model can be assumed to be a representation of the subsurface velocity structure in the area and can then be used for seismic modelling targeted at understanding the real data. The result of the seismic modelling is usually in the form of RT-based traveltime curves of various wave modes superimposed on the real data for identification of events therein. RT-based modelling is often used because it offers the possibility to choose the type of waves to be modelled, including how the waves are to be transmitted / reflected at interfaces. This flexibility makes RT modelling a useful tool for analysis of wave propagation and identification of arrivals (Gjøystdal et al., 2002; Lecomte et al., 2015).

8.2 Basic concepts and definitions in refraction seismic

Some key definitions and terminologies typically used in a seismic survey experiment where refracted signals are recorded in addition to other wave modes are illustrated in Figure 8.1.

The illustration shows a simple subsurface model, survey configuration, and raypaths (direct, refracted, and reflected rays) in the lower part of the diagram. A plot of two traces recorded by a near- and mid-offset receiver shows recognizably different moveouts for direct, refracted, and reflected waves in the time-distance plot shown in the upper part of the diagram. In practice, how early (or later) in time each wave mode appears on the time-distance plot depends on their raypath through the medium; and their amplitudes and how they vary with offsets can provide more information about the medium properties (Chowdhury, 2020).

Some key definitions and concepts based on Figure 8.1 are itemised below (Chowdhury, 2020):

- The slopes of the linear arrivals (direct and refracted waves) are inversely proportional to the corresponding velocities if V_1 and V_2 are constant. Using V_1 (determined from the slope of the direct wave), V_2 (determined from the slope of the refracted wave), the critical angle (calculated using V_1 and V_2), and the intercept time (t_{int}) of the refracted arrival (Figure 8.1), the layer thickness (d) can be calculated.
- The critical distance is the minimum distance at which the refracted arrival is observed in the time-distance plot.
- The crossover distance is the distance at which the refracted arrival overtakes the direct wave and becomes the first arrival. In a layered
  subsurface setting where velocities are increasing with depth, refracted arrivals from deeper interfaces become the first arrival after their corresponding crossover distances.
- Reflected arrivals are hyperbolic in shape (for common depth reflection points) with t_0 representing the zero-offset TWT.
- As the source-receiver offset increases relative to the target depth, supercritical incidence occurs (for e.g., at point W in Figure 8.1), leading to a sharp increase in reflection coefficient which allows the possibility of mapping deep crustal boundaries with small impedance contrasts.

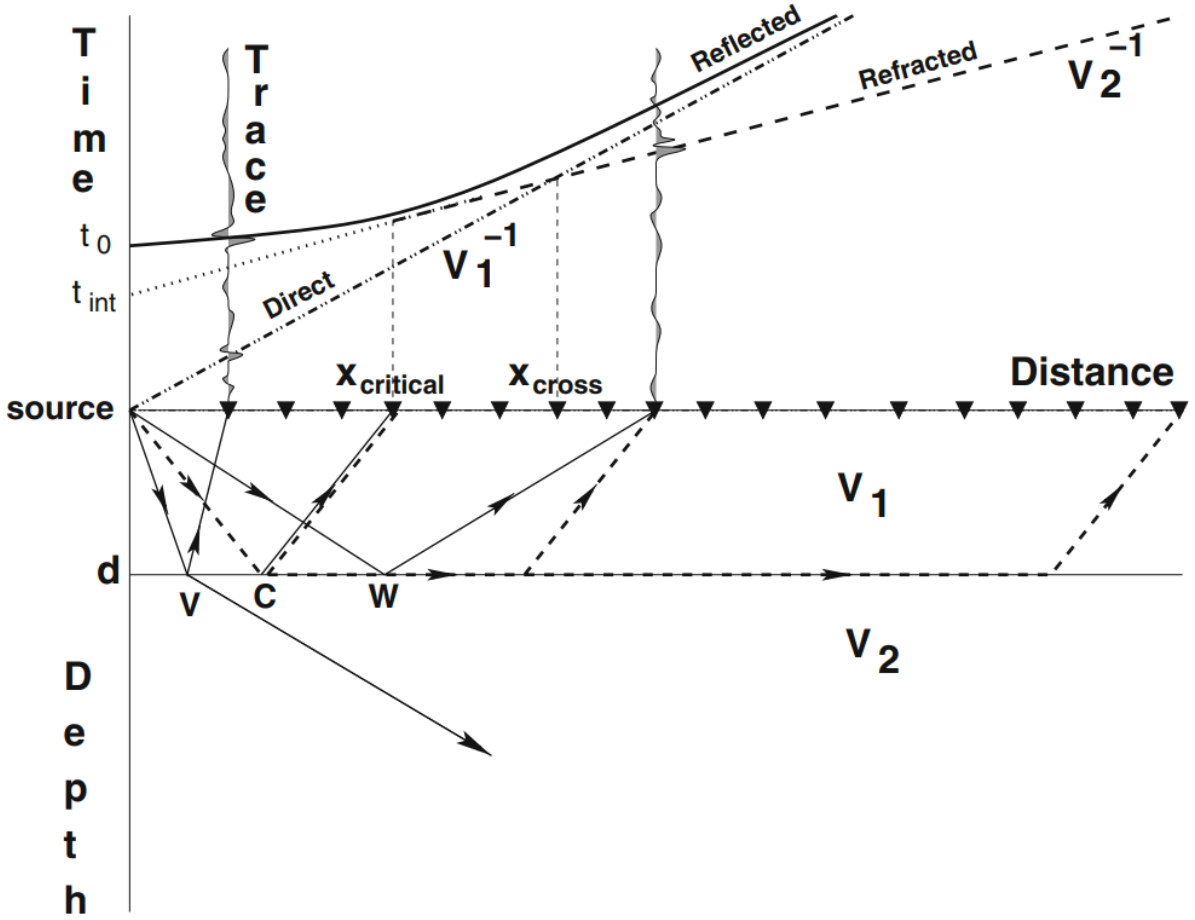

Figure 8.1: Diagram of a multichannel seismic survey to map a simplified subsurface model with layer velocities (V_1 and V_2); where $V_2 > V_1$. Elastic waves initiated by the source propagates through the subsurface and is recorded by the receivers (overturned black triangles) located at the surface as seismic traces. The dash-dots are the direct arrivals (energy directly traveling from the source to the receives along the surface), the continuous lines are reflections from the interface separating the two layers, and the dashed-lines represent critically refracted energy along the interface separating the two layers. The corresponding traveltime curves of the three wave modes are shown in the upper part of the diagram. Near vertical (V), Critical (C), and wide-angle (W) incident energy at the interface separating the two layers are also shown in the diagram. t_0 is the reflection time at zero-offset, t_{int} is the intercept time of the refracted arrival, d is the thickness of the first layer, $X_{critical}$ is the critical distance and X_{cross} is the crossover distance. From Chowdhury. (2020).

It is important to note that for dipping subsurface layers as applicable in the present work, shots from both sides of the area of interest are required to calculate the thickness of the layers (Dentith and Mudge, 2014). In the present work, shots were fired only from the sea and recorded on land.

8.3 Definition of first-arrival branches in the TZ-seismic data

The traveltimes of the first arrivals in the TZ-seismic data were examined to determine the apparent velocities associated with the different traveltime branches observed in the data and relate them to the medium of propagation. In order to do that, the TZ-seismic data were displayed in reduced traveltimes as a function of offset distance. Reduced traveltime displays is a common way of plotting WARRP data (e.g., Mjelde et al., 1993; Raum et al., 2002; Ruiz et al., 2017). When data are displayed in reduced traveltime with a given reduction velocity (V_{red}), it implies that the data are displayed with offset (d) / V_{red} subtracted from the traveltimes (t) (i.e., $t - d/ V_{red}$). The result is that events or arrivals in the data whose apparent velocities are equal to V_{red} will be aligned horizontally.

An example of the firstarrival branches using CRG60 (data recorded by the middle receiver, see Figure 6.12) is shown in Figure 8.2 (top and middle): the data at the top and middle are plotted with automatic gain control (1 s window), and displayed with traveltimes reduced by 4.8 km/s and 4 km/s, respectively. As observed from the figures, the critical offset or critical distance (section 8.2) for this data recorded by the middle receiver is about 2.6 km. The first-arrivals are colour-coded to differentiate them: the blue line is the direct arrival, the yellow line is inferred to be the refracted arrival through the sedimentary unit (reduced with a velocity of 4 km/s in the middle figure). This apparent velocity is very close to the average velocity in the sedimentary unit of the P-wave velocity models (i.e., P-wave velocity 2 and P-wave velocity 3, see Figure 7.3). The red solid line is inferred to be the near- to mid-offset refracted arrivals from the basement (reduced with a velocity of 4.8 km/s in the top figure). This apparent basement velocity is also consistent with the models. The red dotted lines are also inferred to be refracted arrivals from the basement which arrived earlier in time than adjacent arrivals (red solid line) probably due to propagation through a deeper region with higher velocities or a high velocity region within the depth range of the model (for e.g., the highlighted area in black in P-wave velocity 2 shown in the bottom figure). The highlighted high velocity region may be a continuation of the gabbro outcrop seen on land. In addition, it is also possible that the arrivals may have propagated through a shorter raypath with higher velocities outside the 2-D domain in which the modelling was restricted to.

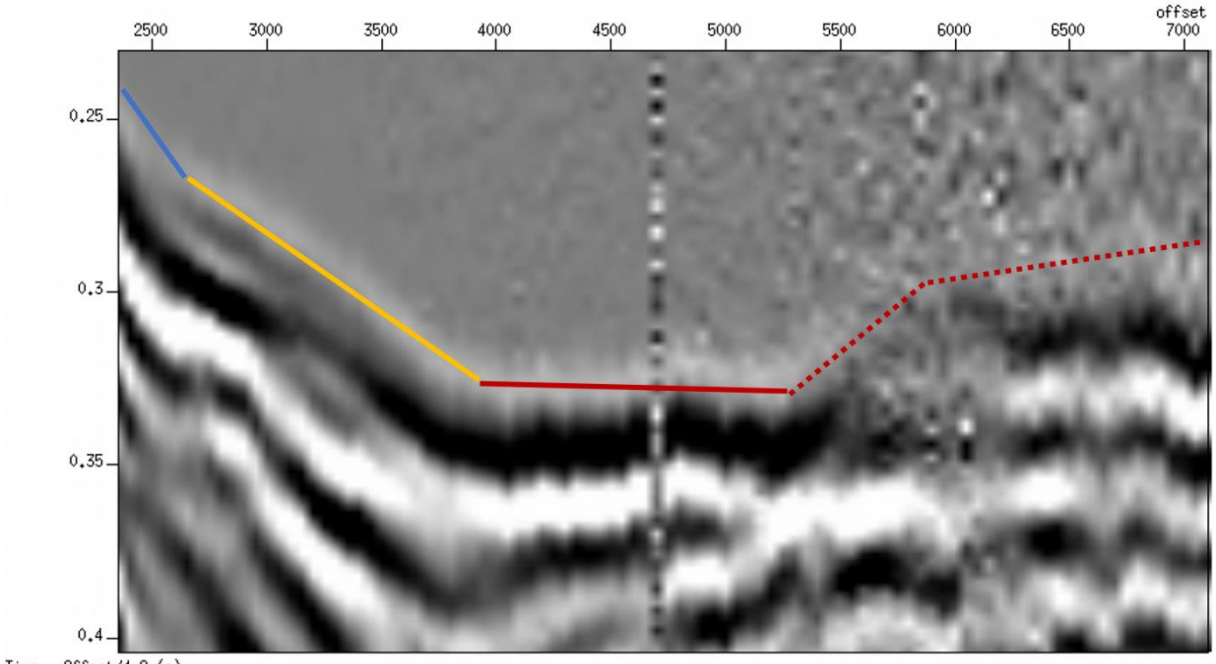

Observed TZ seismic data. CRG60

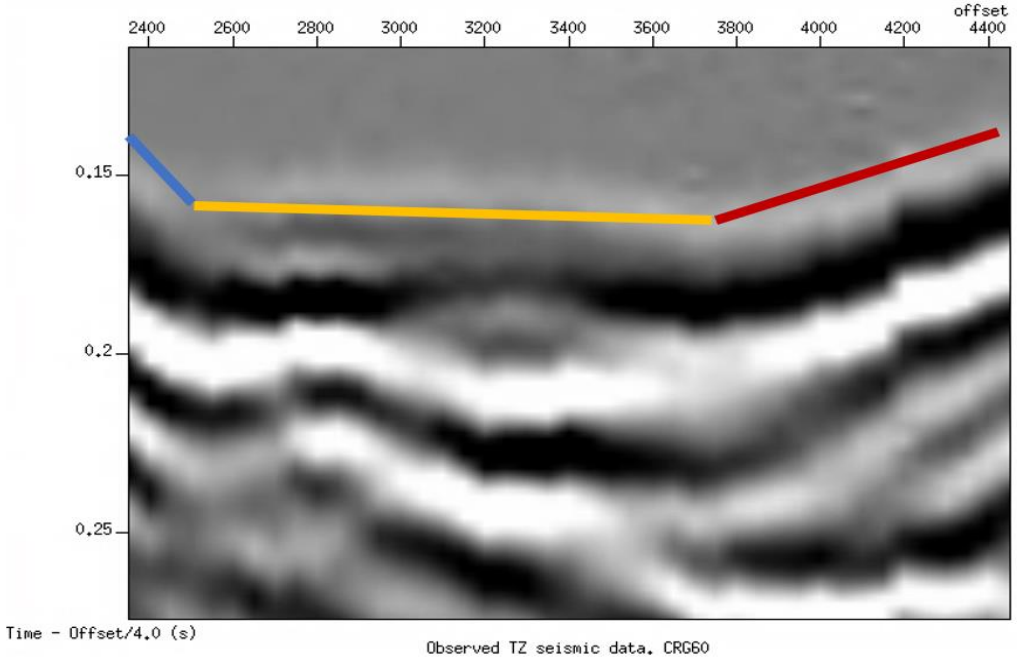

Observed TZ seismic data. CRG60

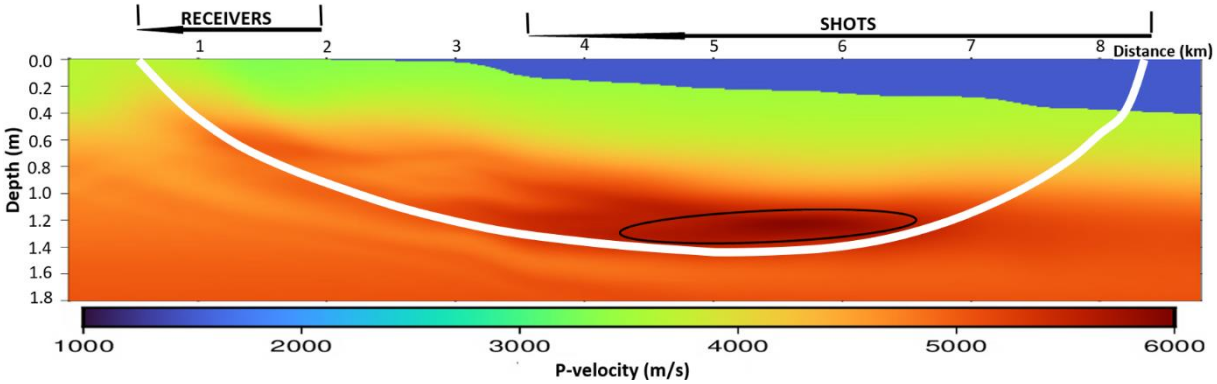

Figure 8.2: Example of the TZ-seismic data (CRG60) plotted with a reduction velocity of 4.8 km/s corresponding to the apparent basement velocity (top), and part of the near-offset data plotted with a reduction velocity of 4.0 km/s corresponding to the apparent velocity of the sedimentary unit (middle). The blue line is the direct arrival; the yellow line is the refracted arrival through the sedimentary unit, the red solid line is the near- to mid-offset refracted arrivals from the basement, and the red dotted lines are also refracted arrivals from the basement which have arrived much earlier in time. The highlighted area in black (bottom figure) is a higher velocity region in the P-wave velocity model in M2 through which the earlier refracted arrivals from the basement (red dotted lines) may have propagated. The area outside the boundary demarcated by the white line is not included in the traveltime tomography computation.

8.3.1 Reflectivity

To examine the reflectivity at some of the interfaces and how they may be influenced by increasing incident angle; the average P- and S-wave velocities, and density values close to the interfaces between the layers were used to compute theoretical reflectivity profiles as a function of incident angle. An example of the reflectivity profile computed with the impedance contrast at BCU is shown in Figure 8.3. The values used in the computation were based on density and average P- and S-wave velocities between 2.5 km and 4.5 km, corresponding to the region where wide-angle reflections are expected, but only few were found by the RT simulation (Figure 7.11).

In the reflectivity figure (Figure 8.3), the modulus (magnitude or reflection coefficient) is plotted to the left and the corresponding phase to the right. As shown in the modulus, the reflection coefficient at normal incidence is about 0.02, but the value decreases with increase in incident angle until it approaches the critical angle (76° in this case) and then, a significant increase in reflection coefficient occurs. As the angle of incidence increases just a little further (i.e., supercritical incidence), total reflection occurs. On the phase plot, it starts with zero-

phase at normal incidence and continues as such until it reaches the critical angle where it suddenly drops. With further increase in incident angle, a 180° phase shift occurs.

The characteristic increase in reflection coefficient at supercritical incidence is the reason why deep subsurface boundaries with small impedance contrasts are successfully imaged (Chowdhury, 2020). That is also the reason why some wide-angle reflections are successfully simulated in this present work, despite the very low impedance contrast, especially in the sedimentary unit. Therefore, the reason for the few wide-angle reflections at BCU and other interfaces is not related to reflectivity.

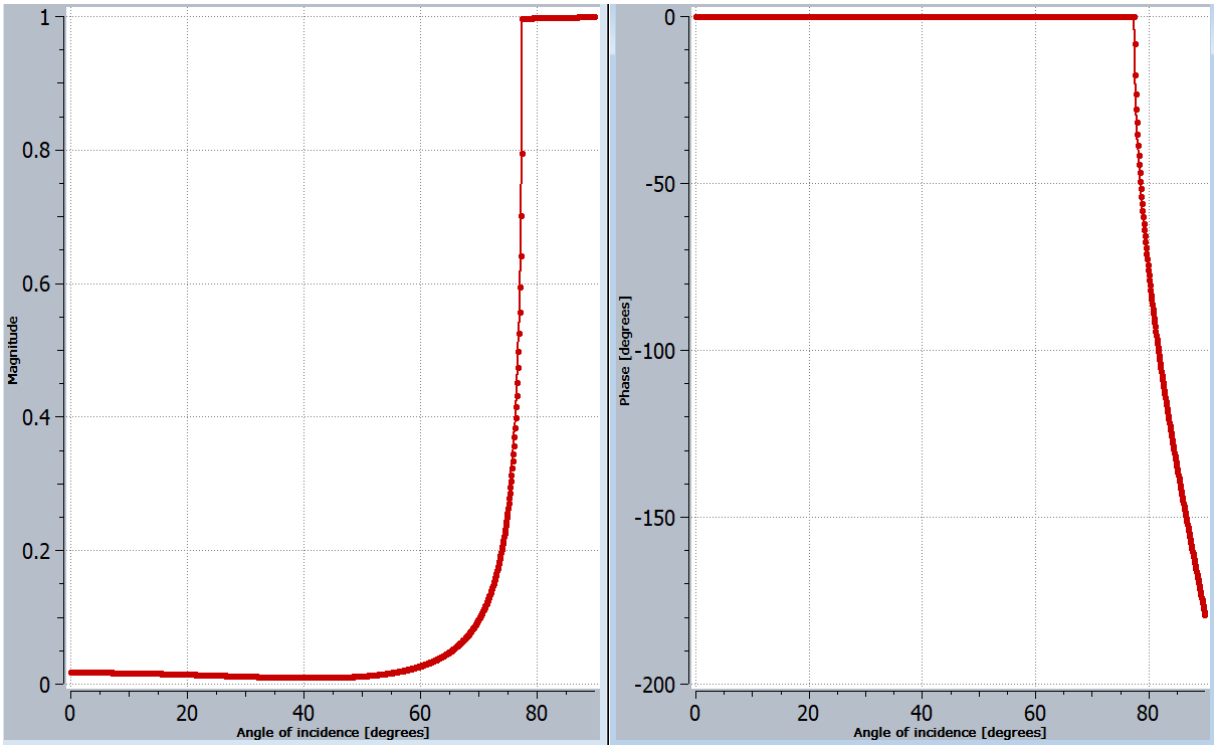

Figure 8.3: Reflectivity profile at BCU interface. The plot to the left represents the magnitude (reflection coefficient) as a function of incident angle, and the plot to the right represents the phase as a function of incident angle.

8.4 TZ-seismic events and RT-based traveltimes

This section will take a closer look at the RT-based traveltimes superimposed on the TZ-seismic data. For this purpose, the TZ-seismic data and traveltime curves are displayed with

reduced traveltimes using a reduction velocity of 4.8 km/s (apparent velocity of top Basement).

8.4.1 Primary P-wave reflections

Figure 8.4 is a display of the TZ-seismic data (CRG1, CRG60, and CRG120) with the modelled traveltime curves for primary P-wave reflections superimposed on the datasets. The modelled traveltimes at near-offsets are arrivals which impinged on the interface at supercritical incident angle (Figure 8.1), and because the angle exceeds the critical angle (Table 7.3), they were totally reflected. The far-offset arrivals consist of rays which appear to have refracted through the interface, and then reflects from the underside (Figure 7.7). This far-offset raypath is likened to turning waves which are described as reflections from the underside of a reflector in a subsurface medium where the velocities are increasing rapidly with depth (Yilmaz, 2001). In seismic data, turning waves exhibit negative moveouts with offset in contrast to other regular reflections (Yilmaz, 2001). In addition, they will have low amplitudes, given that energy reduces with propagation distance (Figure 7.10).

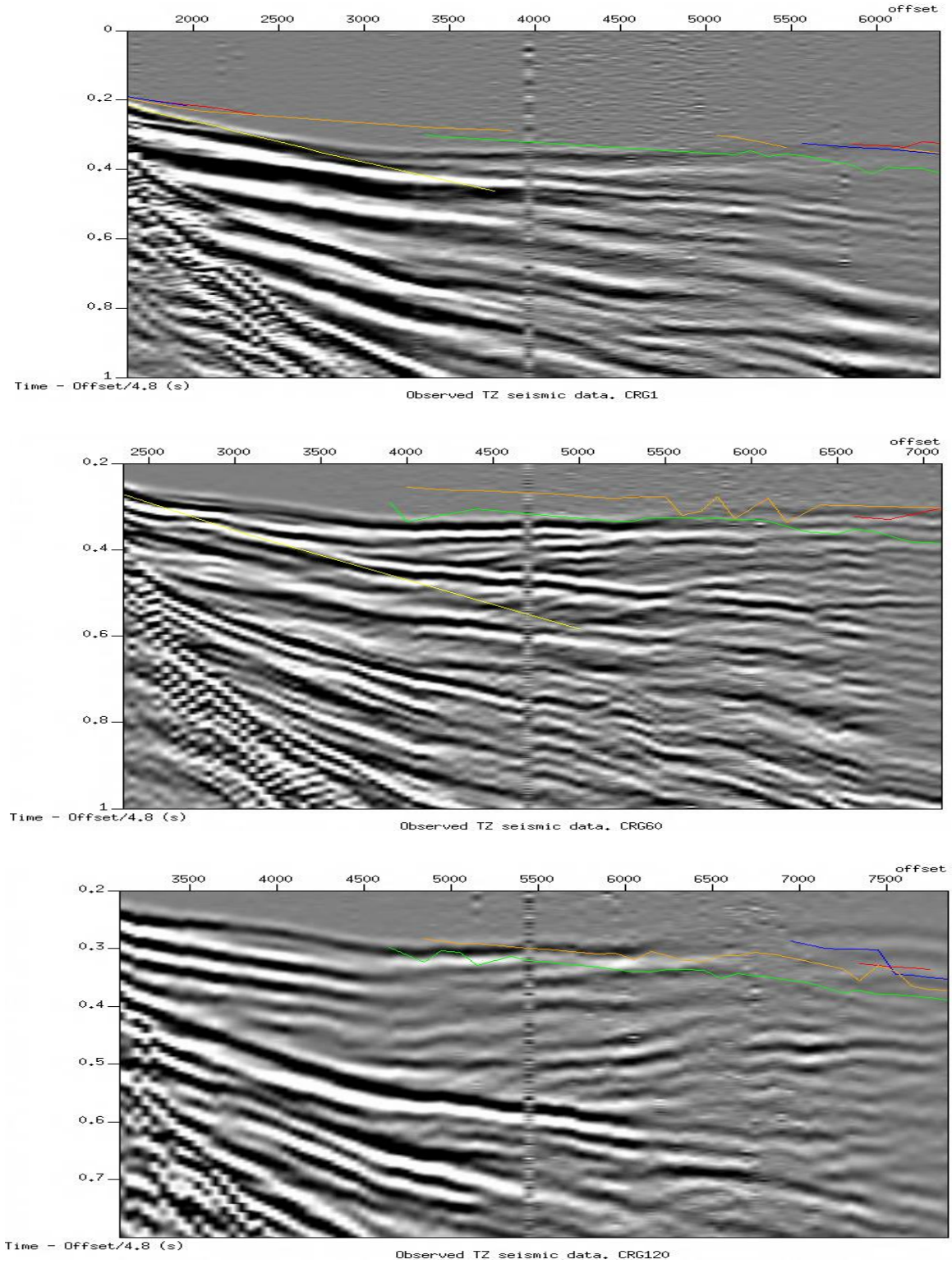

Figure 8.4: Primary P-wave reflection traveltimes superimposed on the TZ-seismic data with traveltimes reduced by 4.8 km/s. CRG1 (top), CRG60 (middle) and CRG120 (bottom) are shown here. The primary P-wave reflection traveltime curves are from top Basement (red), BCU (blue), base Barremian (orange), base Aptian (green) and base Quaternary (yellow). The jitters in the base Aptian curve are due to faults. No events were recorded for base Quaternary at receiver 120, and only one event was recorded for BCU at receiver 60 (not included here).

Some far-offset events were identified in the TZ-seismic data which appears to fit (approximately) with the moveout of the far-offset traveltime curves for base Aptian and base Barremian. These events are highlighted in CRG1 and CRG120 (Figure 8.5). The events may be related to reflections from base Aptian and base Barremian; however, one cannot state that with certainty.

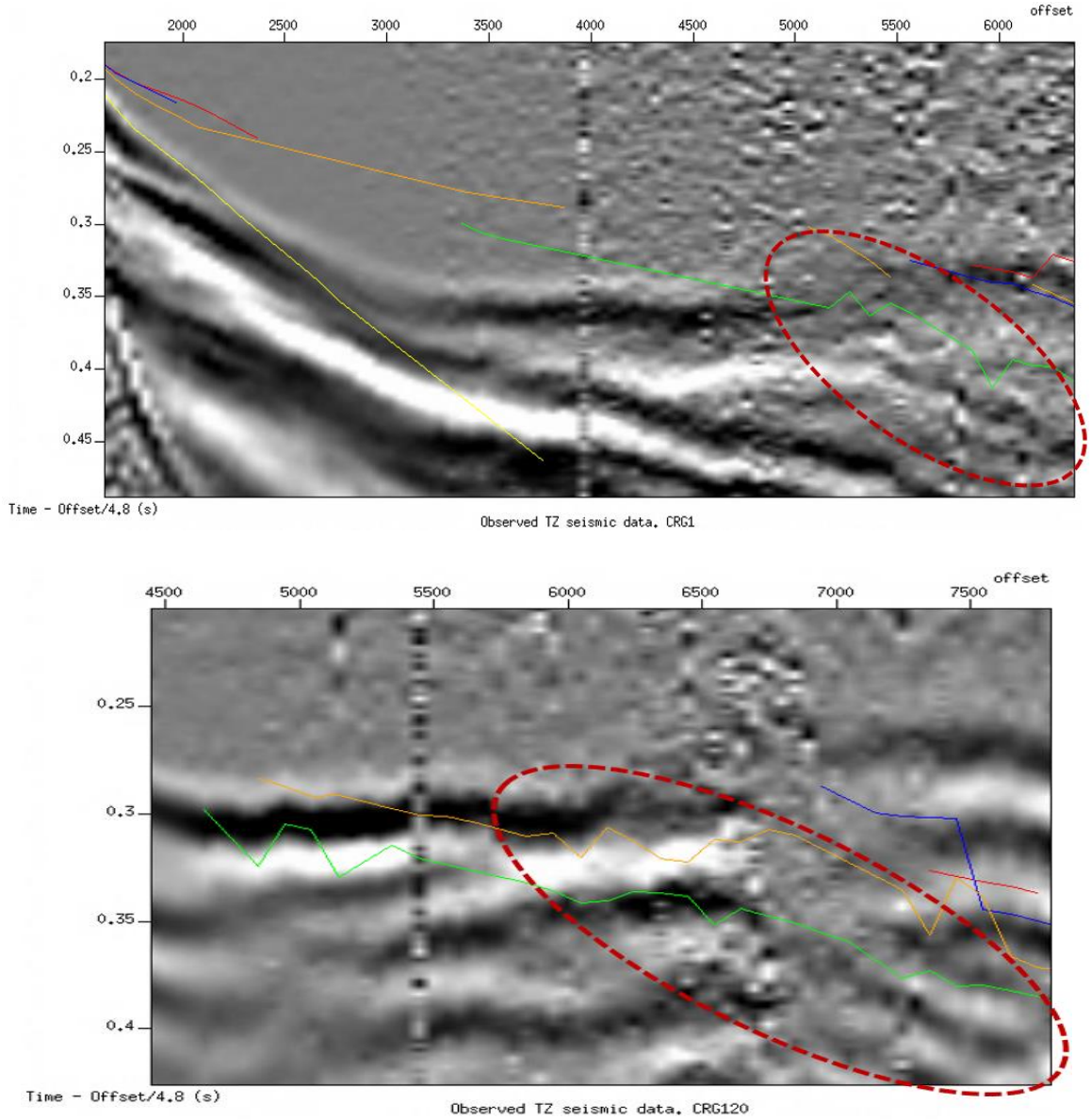

Figure 8.5: Magnified version of CRG1 (top) and CRG120 (bottom) with the P-wave primary reflection traveltime curves superimposed. The primary P-wave reflection traveltime curves are from top Basement (red), BCU (blue), base Barremian (orange), base Aptian (green) and base Quaternary (yellow). No events were recorded for base Quaternary at receiver 120, and only one event was recorded for BCU at receiver 60 (not included here). The highlighted area in red shows some dipping events which seems somewhat consistent with the traveltime curves for base Barremian (orange) and base Aptian (green).

8.4.2 Converted S-waves

The TZ-seismic data with respect to the modelled converted S-waves at the seabed is discussed in this section. Figure 8.6 displays the traveltime curves superimposed on the TZ-seismic data using CRG1, CRG60, and CRG120 as an example. The ray codes for the modelled converted S-waves are as follows:

- P-waves transmitted as S-waves at the seabed interface (red curve in Figure 8.6), named here as curve 1.
- Multiple: P-waves reflected at the seabed, and then the sea surface, and back to the seabed where it transmits as S-waves (green curve in Figure 8.6), named here as curve 2. See Figure 7.23 for raypath example.
- Multiple: P-waves reflected in the following order: seabed - sea surface – seabed – sea surface, and then returns to the seabed where it transmits as S-waves (yellow curve in Figure 8.6), named here as curve 3.

Curve 1 fits approximately with a strong event observed in the TZ-seismic data, especially in CRG1 where it follows the moveout of the event almost perfectly at near-offsets, and changes slightly with offset, following another event directly below.

Curve 2 also fits approximately with a strong event on the TZ-seismic data which can be seen more clearly in CRG1. The curve fits better with the event at mid-offsets but deviates from the event towards the near- and far-offsets. In CRG60 and CRG120, Curve 2 also seems to fit an event approximately, especially at near- to mid-offsets beyond which events seem to be discontinuous. Generally, the curve approximately follows the moveout of the identified events in the TZ-seismic data, even though they do not fit everywhere.

Curve 3 could not be tied to any particular event in the TZ-seismic data. Generally, however, the curve nearly follows the moveout of events at far-offsets.

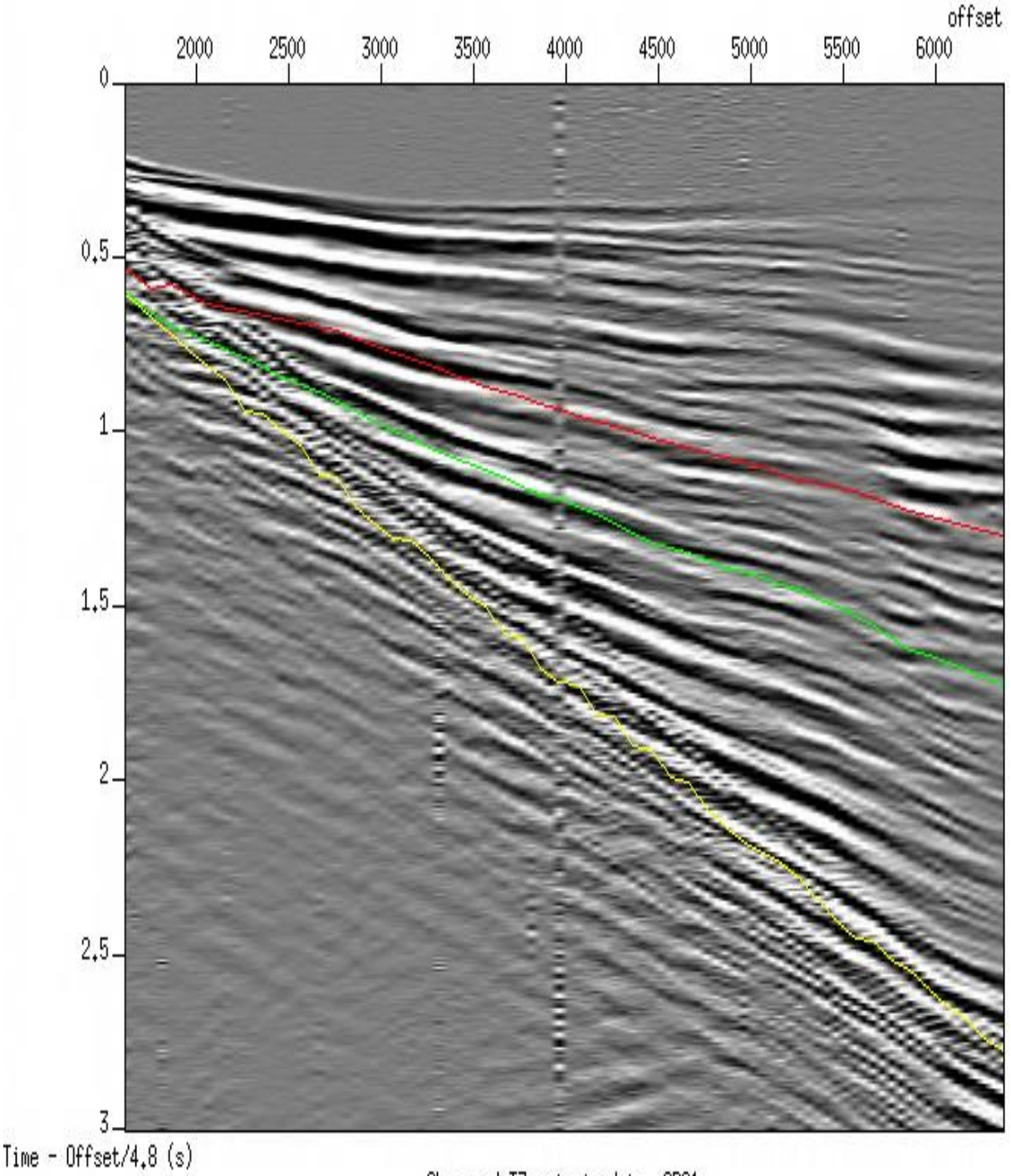

Observed TZ seismic data, CRG1

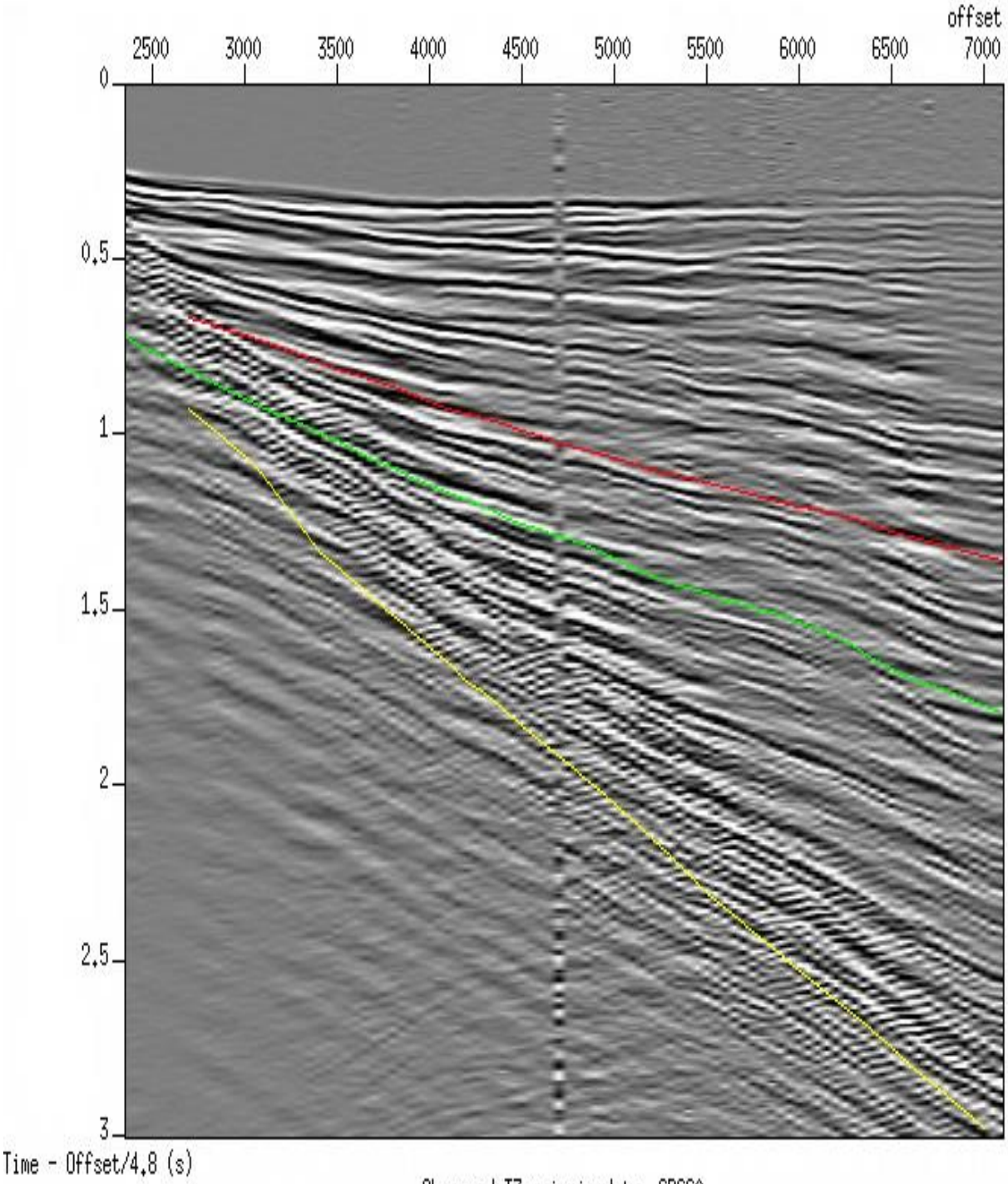

Observed TZ seismic data, CRG60

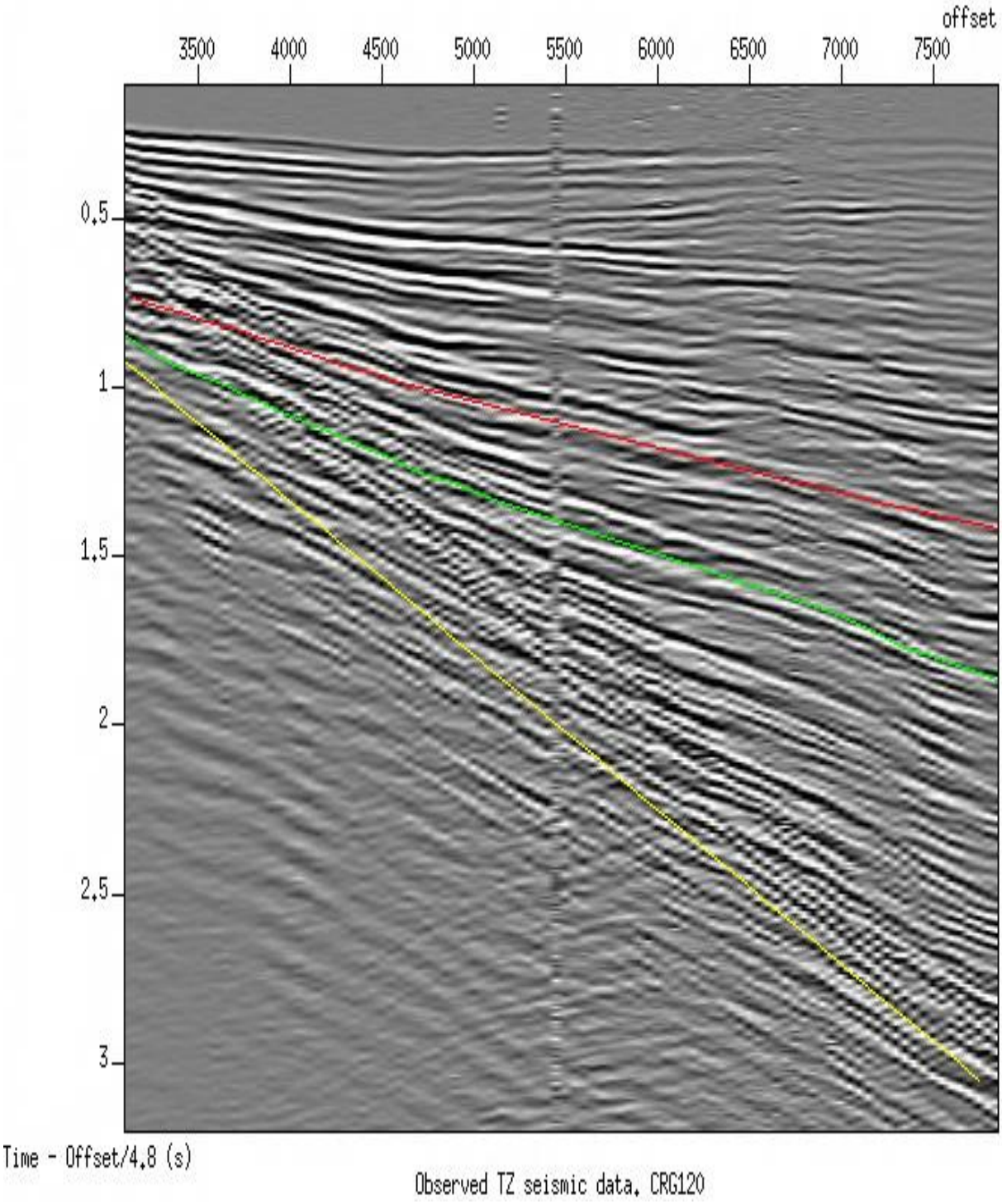

Figure 8.6: TZ-seismic data with modelled converted S-waves superimposed on CRG1 (top), CRG60 (middle), and CRG120 (bottom). The traveltime curves are: P-waves transmitted as S-waves at the seabed interface (red); P-waves reflected at the seabed, and then the sea surface, and back to the seabed where it transmits as S-waves (green); P-waves reflected in the following order: seabed - sea surface – seabed – sea surface, and then returns to the seabed where it transmits as S-waves (yellow).

8.4.3 Multiple P-wave reflections

The TZ-seismic data with respect to the modelled P-wave multiple reflections are discussed in this section. Figure 8.7 displays the traveltime curves superimposed on the TZ-seismic data using CRG1, CRG60, and CRG120 as an example. The ray codes are described below:

- Multiple P-wave reflections in the following order: seabed - sea surface – seabed (top red in Figure 8.7), named here as curve 4.
- Multiple P-wave reflections in the following order: seabed – sea surface – seabed – sea surface - seabed (bottom red in Figure 8.7), named here as curve 5.
- Multiple P-wave reflections in the following order: top Basement – seabed – top Basement (yellow in Figure 8.7), named here as curve 6.
- Multiple P-wave reflections in the following order: top Basement – seabed – top Basement – seabed – top Basement (blue in Figure 8.7), named here as curve 7.
- Multiple P-wave reflections in the following order: top Basement – sea surface – top Basement (green in Figure 8.7), named here as curve 8.
- Multiple P-wave reflections in the following order: top Basement – sea surface – top Basement – sea surface – top Basement (purple in Figure 8.7), named here as curve 9.

Curve 4 (first red curve) fits perfectly with a very strong event about 20 ms below the curve in CRG1. The event is continuous and characterized by a change in polarity which makes it most likely to be indeed the seabed multiple. In CRG60, curve 4 also follows an event much more closely until about 4700 m offset where the moveout changed but fits with another event slightly up to the farthest offset. In CRG120, curve 4 cannot be confidently tied to any particular event; however, there is a strong event about 40 ms below the curve at far-offset and about 20 ms below at mid-offset which seems to fit the curve, but not at far-offset.

Curve 5 (second red curve) fits perfectly with a strong event between 2100 m to 4800 m offset in CRG1, and follows the moveout of the same event about 40 ms below the curve between the nearest-offset to about 2100 m offset. The moveout of the curve differs with the events at far far-offsets for the three sets of receiver gathers. In CRG60, curve 5 also fits with an event almost perfectly except at far-offset. In CRG120, curve 5 fits perfectly with an event at near-offset and follows some discontinuous events from about 5500 m to 7000 m offset.

Curve 6 appears to follow a strong events at near-offset in CRG1 from about 2200 m offset, however the traveltime data are inadequate to determine if the event can be related to the curve or not. Curve 6 appears to be overlapping or very close to curve 8 in all the three

receiver gather sets. At far-offset in CRG1 and CRG120, the curves appear to fit with some weak events which cannot be confidently tied to the events, given the insufficient traveltime data.

Curve 7 partly fits a very strong event in CRG1 between 2500 m to 3500 m offset and between 3200 m to 4300 m in CRG60. However, this event cannot be confidently tied to the curve 7. At far-offsets, the curve fits with a very low energy event in CRG60 and CRG120.

Curve 8 is very close to curve 6 and both curves overlap each other in places. Hence, the event associated with curve 6 may also be related to curve 8, except in CRG1 at near-offset, where the event is much closer to a very strong event associated with curve 7.

Curve 9 is quite close to a very strong event directly above the curve between 2200 m and 2800 m offset in CRG1, and in CRG60, the curve appears to fit a relatively strong event between 2600 m and 3300 m. At far-offsets, the curve fits with an event quite well in CRG60; however, the traveltime data are inadequate to make a proper assessment of the event. There were no events recorded for CRG120.

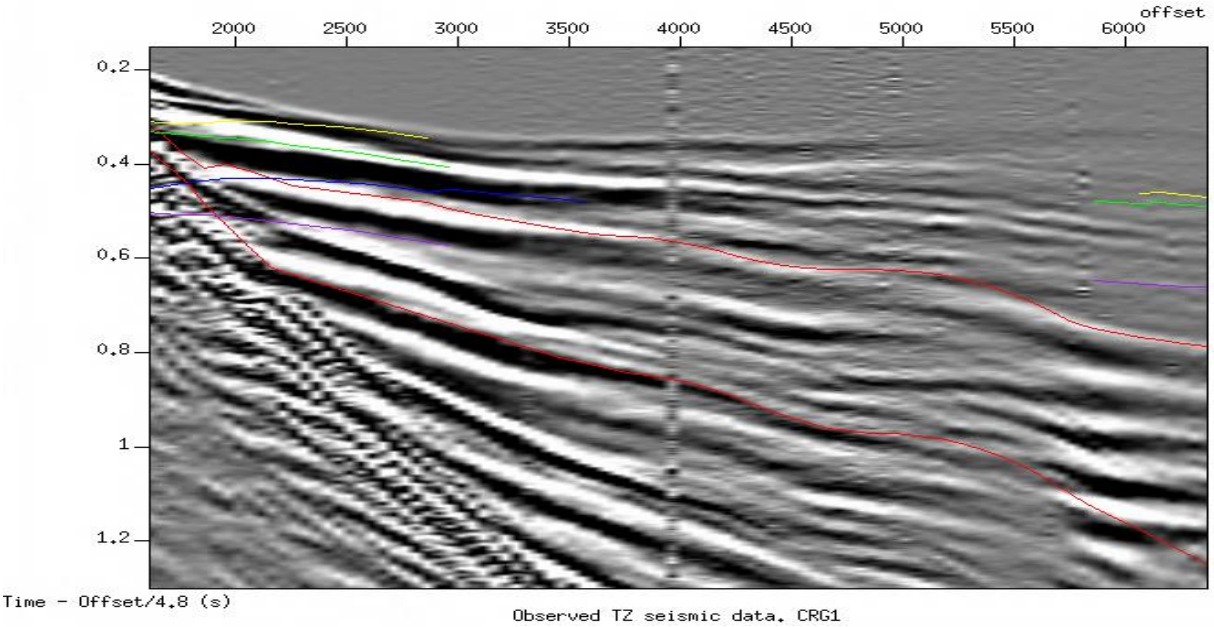

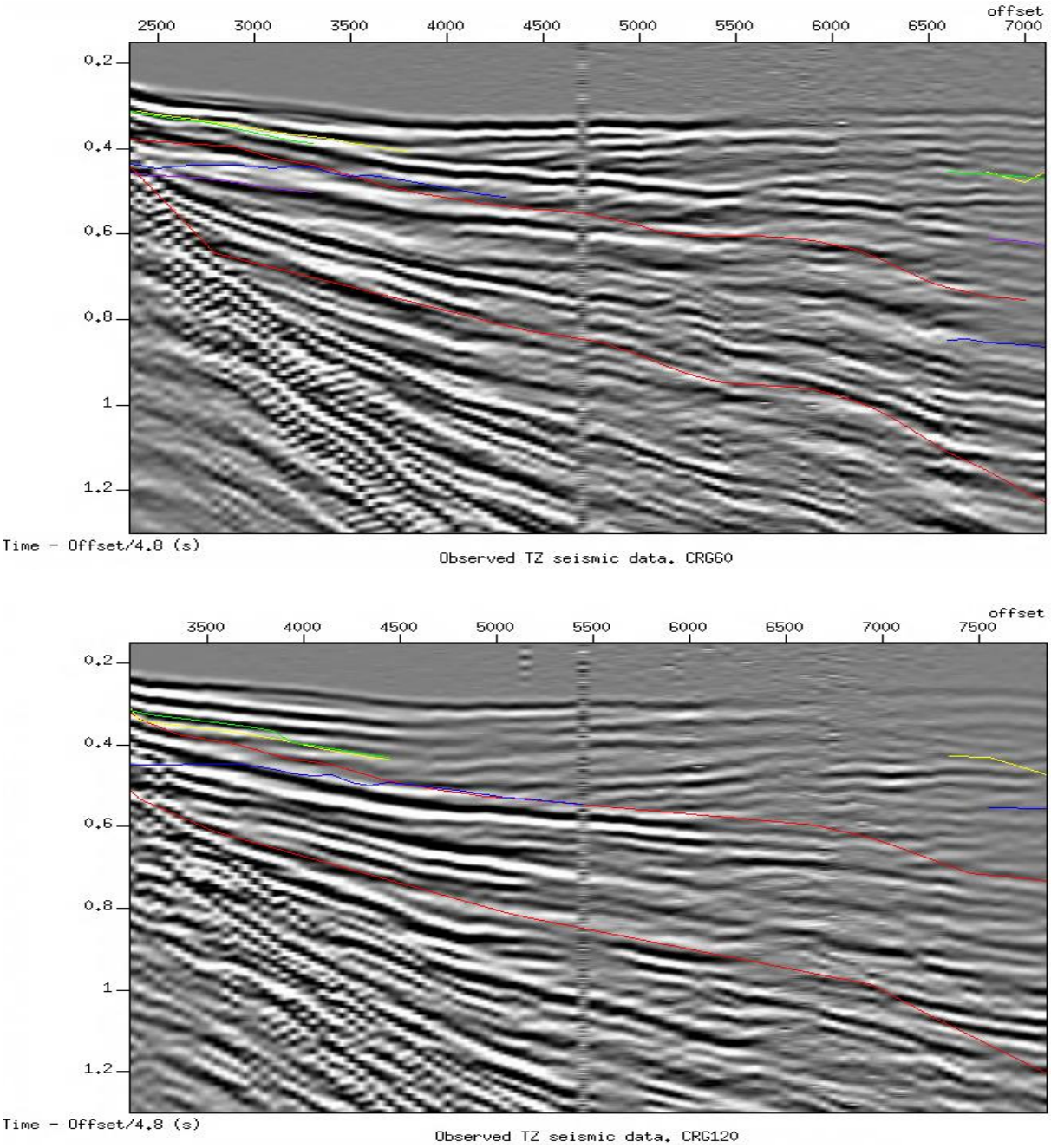

Figure 8.7: TZ-seismic data with modelled multiple P-wave reflection traveltimes superimposed on CRG1 (top), CRG60 (middle), and CRG120 (bottom). The traveltime curves are described according to the order and number of reflections per interface: seabed - sea surface – seabed (top red); seabed – sea surface – seabed – sea surface - seabed (bottom red); top Basement – seabed – top Basement (yellow); top Basement – seabed – top Basement – seabed – top Basement (blue); top Basement – sea surface – top Basement (green); top Basement – sea surface – top Basement – sea surface – top Basement (purple).

8.5 Limitations and uncertainties

The limitations and uncertainties associated with this study will be discussed in this section.

8.5.1 P-wave velocity models

As described in the previous chapter, P-wave velocity 3 (Table 7.1) is the result of an attempt to obtain an approximate version of P-wave velocity 2 (Table 7.1) which could not be used for RT due to the mismatch between the velocity contrast and interfaces defined in the model (Figure 7.3). To have interfaces properly placed where discontinuities in properties exist is a necessary requirement in RT modelling because they are used to represent changes in impedance contrast (Cerveny, 2001; Gjøystdal et al., 2002). P-wave velocities 2 and 3 fit each other better for the sedimentary unit, but less so for the basement. Therefore, P-wave velocity 3 which was used in the RT simulation is not an entirely good fit for P-wave velocity 2. Notwithstanding, the overall fit between the two models is reasonably satisfactory. Furthermore, P-wave velocity 2 which was derived via traveltime tomography may not be an accurate representation of the subsurface velocity structure in the study area. This is due to the fact that velocity models derived via traveltime tomography is non-unique; which implies that there are many other possible models that may fit the traveltimes used in the computation equally well (Rawlinson et. Al., 2010; Zelt, 2011; White, 2020). In addition, there is some level of uncertainty associated with the traveltimes of the first arrivals (at far-offsets) used in the traveltime computation. Basically, the accuracy of the synthetic data and traveltimes generated in this study depends on how close the velocity model (and density) fits the real subsurface elastic properties. Figure 6.8

8.5.2 Multiples

The reason for unidentifiable primary reflections in the TZ-seismic data is mostly due to multiples which dominate the data, especially strong seabed multiples owing to the high acoustic impedance contrast between the sea water and well-consolidated seabed.

8.5.3 Resolution and illumination effect

In addition to unwanted noise generated by multiples, significant vertical resolution issues may also exist which prevents most of the interfaces from being mapped as separate events in

the seismic data (section 4.2.5). This is due to how close the interfaces are to each other in relation to the dominant wavelength (see section 6.4). The modelled RT traveltimes confirms significantly close or overlapping traveltimes. The reflectors that seem to be affected mostly by this phenomenon known as tuning effect are top Basement, BCU, and base Barremian (Figure 7.24 and Figure 8.4). The consequence of overlapping reflectors is constructive / destructive interference which have most likely occurred in the real data. In addition, the generation of many arrivals from different type of waves (e.g., reflected waves, refracted waves, converted waves, multiples etc) will also lead to several other possibilities for constructive or destructive interference. In the TZ-seismic data, one can observe some brightened / dampened amplitudes (see CRG1 in Figure 8.7).

Illumination is also a concern. The presence of faults will generate back-scattered waves which will propagate back towards the source instead of the receiver.

8.5.4 Exclusion of head waves

RT-based modelling is very efficient in many applications. However, one of the drawbacks is that head waves (and surface waves) are not modelled (Gjøystdal et al., 2002). For this reason, the amount of RT-based data that were used to analyse the TZ-seismic data were limited to wide-angle reflection traveltimes and the traveltimes from far-offset reflections behaving like turning waves.

8.5.5 3-D effects

The limitation of modelling in 2-D is that potential 3-D effects which may be inherent in the subsurface area of interest are not taken into consideration. For example, the TZ-seismic data were acquired on a 3-D subsurface structure and the raypath for the various events recorded may not necessarily be along the ideal source – receiver plane, as rays can follow different raypaths to the receivers, some of which may deviate significantly from the source – receiver plane. Therefore, mismatch in traveltimes between the model and real data may also be related to 3D effects. The modelling performed in this study was restricted to 2-D due to time constraints and limitations associated with computational resources.

Chapter 9:

Conclusion and further work

9.1 Conclusions

The aim of this thesis was to use seismic modelling to analyse a TZ-seismic data for better understanding of the data, and to propose new acquisition strategies. This has been achieved by deriving an appropriate model and simulating various traveltimes for different wave modes which was used to analyse the TZ-seismic data. The main conclusions of the study are itemised below:

1. Multiples dominate the TZ-seismic data. The lack of identifiable reflections is mostly due to strong seabed multiples which were identified in the data using the RT-based traveltimes.

2. The data are marred by significant resolution effect, partly due to tuning effect and possibly also due to many ray types overlapping and causing constructive / destructive interference, in addition to those caused by tuning effect.

3. Turning waves may also exist in the TZ-seismic data, given the geometry and velocity structure of the study area, but further investigation is required.

4. By extending the receivers seawards, the reflection coverage along the TZ is greatly improved, and only a few shots may be required (Figure 7.32).

5. Most of the multiple reflections are concentrated around the TZ (Figure 7.22).

9.2 Recommendation for future work

The following recommendations are proposed:

- Inclusion of OBS in future surveys will allow the possibility of recording S-waves in addition to P-waves.

- In the future, it would be interesting to run the RT using methods known as eikonal solvers which is very well suited for refraction seismic (Lecomte et al., 2000). This method can automatically calculate a grid of traveltimes of the theoretical first arrivals; and based on this grid, corresponding raypaths can also be obtained.

- Multiple reflections which appear to be concentrated along the TZ may be exploited. Full waveform inversion methods may be considered for imaging the data.

References

Abdelmalak, M., Andersen, T. B., Planke, S., Faleide, J. I., Corfu, F., Tegner, C., Shephard, G. E., Zastrozhnov, D., & Myklebust, R. (2015). The ocean-continent transition in the mid-Norwegian margin; insight from seismic data and an onshore Caledonian field analogue. Geology (Boulder), 43(11), 1011–1014.

Alaei, B. (2012). Seismic Modelling of Complex Geological Structures. IntechOpen.

Aouad, A., Taylor, R., &Millar, N. (2012). Seismic on the edge – a 3D transition zone seismic survey from concept to final volume. ASEG Extended abstracts, 2012(1), 1–5.

Baranwal, V., Brönner, M., Rønning, J., Elvebakk, H., & Dalsegg, E. (2020). 3D interpretation of helicopter-borne frequency-domain electromagnetic (HEM) data from Ramså Basin and adjacent areas at Andøya, Norway. Earth, Planets, and Space, 72(1), 1-14.

Berenger, J. P. (1994). A perfectly matched layer for the absorption of electromagnetic waves. Journal of computational physics, 114(2), 185-200.

Bernth, H., & Chapman, C. (2011). A comparison of the dispersion relations for anisotropic elastodynamic finite-difference grids. Geophysics, 76(3), WA43-WA50.

Beydoun, W. B., & Keho, T. H. (1987). The paraxial ray method. *Geophysics*, *52*(12), 1639-1653.

Brönner, M., Bering, D., Dalsegg, E., Fabian, K., Fredin, O., Hendriks, B., ... & Øverland, J. A. (2010, June). On–and Offshore Deep Weathered Basement Rocks, Norway. In 72nd EAGE Conference and Exhibition incorporating SPE EUROPEC 2010 (pp. cp-161). European Association of Geoscientists & Engineers.

Brönner, M., Johansen, T.A., Baranwal, V., Crne, A., Davidsen, B., Elvebakk, H., Engvik, A., Torthun, T., Gellein, J., Henningsen, T., Lutro, O., Margreth, A., Midbøe, P., Ruud, B.O., Rueslåtten, H., Ryseth, A., Rønning, J.S., Schiellerup, H., Schönenberger, J., Smelror, M., Tveten, E. (2017) Ramså basin, northern Norway: an integrated study, NGU report 2017.027, pp. 290.

Bøe, R., Fossen, H., & Smelror, M. (2010). Mesozoic sediments and structures onshore Norway and in the coastal zone. Norges geologiske undersøkelse Bulletin, 450, 15-32.

Carcione, J. M., Herman, G. C., & Ten Kroode, A. P. E. (2002). Seismic modelling. Geophysics, 67(4), 1304-1325.

Cerveny, V., Molotkov, I. A., & Pšencik, I. (1977). Ray method in seismology: Univerzita Karlova. Prague, Czeckoslovakia.

Cerveny, V. (1985). The application of ray tracing to the numerical modeling of seismic wavefields in complex structures. Seismic shear waves 15: 1-124.

Cerveny, V. (2001). Seismic ray theory. Cambridge: Cambridge University Press.

Chowdhury, K.R. (2020). Deep seismic reflection and refraction profiling. In: H.K. Gupta, ed., Encyclopedia of Solid Earth Geophysics. Encyclopedia of Earth Sciences Series. Springer, pp. 103-118.

Collino, F., & Tsogka, C. (2001). Application of the perfectly matched absorbing layer model to the linear elastodynamic problem in anisotropic heterogeneous media. Geophysics, 66(1), 294-307.

Costain, J. K., & Çoruh, C. (2004). Basic Theory in Reflection Seismology: with MATHEMATICA Notebooks and Examples on CD-ROM. Elsevier.

Dai, N., Wu, W., & Liu, H. (2014). Solutions to numerical dispersion error of time FD in RTM. In SEG Technical Program Expanded Abstracts 2014 (pp. 4027-4031). Society of Exploration Geophysicists.

Dalland, A., Hansen, R. & Sellevoll, M. (1973). Geologiske og geofysiske undersøkelser av jura-krittfeltet på Andøya utført av Universitetet i Bergen 1969-1971 - foreløpig meddelelse. Upublisert Universitetet i Bergen rapport, 35s.

Dalland, A. (1975). The Mesozoic rocks of Andøy, northern Norway. Geological Survey of Norway 316, 271-287.

Dalland, A. (1981) Mesozoic sedimentary succession at Andøy, northern Norway and relation to structural development of the North Atlantic Area. Canadian Society of Petroleum Geologists Memoir, 7, 563–584.

Dentith, M., & Mudge, S. T. (2014). Geophysics for the mineral exploration geoscientist. Cambridge University Press.

Dragoset, B. (2000). Introduction to air guns and air-gun arrays. The Leading Edge, 306 August 2000.

Dypvik, H. (1979). Mineralogy and geochemistry of the Mesozoic sediments of Andøya, Northern Norway. Sedimentary Geology, 24(1), 45-67.

Etris, E. L., Crabtree, N. J., Dewar, J., & Pickford, S. (2001). True depth conversion: more than a pretty picture. CSEG recorder, 26(9), 11-22.

Friis, J.P. (1903). Andøens kulfelt. Norges Geologiske Undersøkelse 36, 1–40 (Aarbog for 1903).

Gadallah, M., & Fisher, R. (2009). Exploration Geophysics (1st ed. 2009). Springer Berlin Heidelberg : Imprint: Springer.

Gelius, L., & Johansen, T. (2010). Petroleum geophysics. Bergen: Unigeo.

Hauer, G., James, G. (2009). Transition zone acquisition: Operating in shallow water with land equipment. Petroleum Africa, November, pp. 49-51.

Gjoystdal, H., Iversen, E., Laurain, R., Lecomte, I., Vinje, & Astebol, K. (2002). Review of ray theory applications in modelling and imaging of seismic data. Studia Geophysica Et Geodaetica, 46(2), 113-164.

Gjøystdal, H., Iversen, E., Lecomte, I., Kaschwich, T., Drottning, A., & Mispel, J. (2007). Improved applicability of ray tracing in seismic acquisition, imaging, and interpretation. Geophysics, 72(5), SM261-SM271.

Helland, A. (1897). Lofoten og Vesteraalen (Vol. 23, Norges geologiske undersøkelse (trykt utg.)). Kristiania: I kommission hos Aschehoug.

Higgins, P., & Foley, A. (2014). The evolution of offshore wind power in the United Kingdom. Renewable & Sustainable Energy Reviews, 37, 599-612.

Johansen, T. A., Ruud, B. O., Henningsen, T., & Brönner, M. (2020). Seismic mapping of on-shore sediments at Andøya, Norway, deposited prior to the North Atlantic rifting. Interpretation, 8(4), SQ105-SQ114.

Keydar, S., Koren, Z., Kosloff, D., & Landa, E. (1989). Optimum time-to-depth conversion. Geophysics, 54(8), 1001-1005.

Kim, J., Oh, K., Kang, K., & Lee, J. (2013). Site selection of offshore wind farms around the Korean Peninsula through economic evaluation. Renewable Energy, 54, 189-195.

Korenaga, J., Holbrook, W., Kent, G., Kelemen, P., Detrick, R., Larsen, H., Hopper, J., Dahl-Jensen, T. (2000). Crustal structure of the southeast Greenland margin from joint refraction and reflection seismic tomography. *Journal of Geophysical Research, 105*(B9), 21591-21614.

Korenaga, J., & Sager, W. W. (2012). Seismic tomography of Shatsky Rise by adaptive importance sampling. Journal of Geophysical Research: Solid Earth, 117(B8).

Krebes, E. S. (2004). Seismic forward modelling. CSEG Recorder, 30, 28-39.

Larry, W., & Ahmad, K. (2013, October). Transition Zone Seismic Acquisition on the Alaska North Slope, Simpson Lagoon. Paper presented at the SPE Arctic and Extreme Environments Technical Conference and Exhibition, Moscow, Russia.

Komatitsch, D., & Tromp, J. (2003). A perfectly matched layer absorbing boundary condition for the second-order seismic wave equation. Geophysical Journal International, 154(1), 146-153.

Le Bégat, S., Chauris, H., Devaux, V., Nguyen, S., & Noble, M. (2004). Velocity model estimation for depth imaging: Comparison of three tomography methods on a 2D real data set. Geophysical prospecting, 52(5), 427-438.

Lecomte, I., Gjøystdal, H., Dahle, A., & Pedersen, O. C. (2000). Improving modelling and inversion in refraction seismics with a first-order Eikonal solver. Geophysical Prospecting, 48(3), 437-454).

Lecomte, I. (2006, October). Illumination, resolution, and incidence-angle in PSDM: a tutorial. In 2006 SEG Annual Meeting. OnePetro.

Lecomte, I. (2008). Resolution and illumination analyses in PSDM: A ray-based approach. The Leading Edge 27: 650-663.

Lecomte, I., and Gelius, L. (1998). Have a look at the resolution of prestack depth migration for any model, survey and wavefields: 68th Annual International Meeting, SEG, Expanded Abstracts, 1112–1115.

Lecomte, I., Gjøystdal, H., Drottning, A., Maao, F. A., Johansen, T. A., & Bakke, R. (2004). Efficient and flexible seismic modeling of reservoirs: A hybrid approach. The Leading Edge, 23(5), 432-437.

Lecomte, I., Lavadera, P., Anell, I., Buckley, S., Schmid, D., & Heeremans, M. (2015). Ray-based seismic modelling of geologic models; understanding and analyzing seismic images efficiently. Interpretation (Tulsa), 3(4), SAC71-SAC89.

Levander A.R. (1989). Finite-difference forward modeling in seismology. In: Geophysics. Encyclopedia of Earth Science. Springer, Boston, MA.

Levin, F. K. (1996). Anatomy of diving waves. *Geophysics*, *61*(5), 1417-1424.

Lindsey, J. (1989). The Fresnel zone and its interpretive significance. The Leading Edge., 8(10), 33-39.

Lines, L. R., & Newrick, R. T. (2004). Fundamentals of geophysical interpretation. Society of Exploration Geophysicists.

Liu, Hao, T., Lü, C., You, Q., Pan, J., Wang, F., Xu, Y., Zhao, C., & Zhang, J. (2015). Crustal structure of Bohai Sea and adjacent area (North China) from two onshore–offshore wide-angle seismic survey lines. Journal of Asian Earth Sciences., 98, 457–469.

Makris, J., Egloff, F., & Rihm, R. (1999). WARRP (Wide Aperture Reflection and Refraction Profiling): The principle of successful data acquisition where conventional seismic fails. In SEG Technical Program Expanded Abstracts 1999 (pp. 989-992). Society Of Exploration Geophysicists.

Masoli, C. A., Petronio, L., Gordini, E., Deponte, M., Boehm, G., Cotterle, D., ... & Baradello, L. (2020). Near-shore geophysical and geotechnical investigations in support of the Trieste Marine Terminal extension. Near Surface Geophysics, 18 (1-Quantitative Geophysical Characterisation of Marine Near-Surface), 73-89.

Midbøe, P. (2011). Geologisk introduksjon til Ramsåfeltet, Andøya og Sortlandsundetbassenget Vesterålen, fourth edition. Statoil report.

Mittet, R. (2002). Free-surface boundary conditions for elastic staggered-grid modeling schemes. Geophysics, 67(5), 1616-1623.

Mjelde, R., Sellevoll, M. A., Shimamura, H., Iwasaki, T., & Kanazawa, T. (1993). Crustal structure beneath Lofoten, N. Norway, from vertical incidence and wide-angle seismic data. Geophysical Journal International, 114(1), 116-126.

Moczo, P., Kristek, J., & Halada, L. (2004). The finite-difference method for seismologists. An Introduction, 161.

Moldoveanu, N., Kapoor, J., & Egan, M. (2008). Full-azimuth imaging using circular geometry acquisition. The Leading Edge., 27(7), 908-913.

Olesen O., Bering D., Brönner M., Dalsegg E., Fabian K., Fredin O., Gellein J., Husteli B., Magnus C., Rønning J.S., Solbakk T., Tønnesen J.F. &Øverland J.A. 2012. Tropical Weathering in Norway, TWIN Final Report, NGU Report 2012.005, pp.188.

Olesen, O., Kierulf, H., Bronner, M., Dalsegg, E., Fredin, O., & Solbakk, T. (2013). Deep weathering, neotectonics and strandflat formation in Nordland, northern Norway. Norwegian journal of geology, 93(3-4), 189-213.

Paasche, Ø., Strømsøe, J.R, Dahl, S.O. & Linge, H. (2006). Weathering characteristics of arctic islands in northern Norway. Geomorphology 82, 430–452.

Park, C. B., Miller, R. D., Steeples, D. W., & Black, R. A. (1996). Swept impact seismic technique (SIST). *Geophysics*, *61*(6), 1789-1803.

Petersen, H., Øverland, J., Solbakk, T., Bojesen-Koefoed, J., & Bjerager, M. (2013). Unusual resinite-rich coals found in northeastern Greenland and along the Norwegian coast: Petrographic and geochemical composition. International Journal of Coal Geology, 109-110, 58-76.

Pujol, J. (2003). Elastic wave propagation and generation in seismology (Vol. 227). Cambridge: Cambridge University Press.

Raum, T., Mjelde, R., Digranes, P., Shimamura, H., Shiobara, H., Kodaira, S., Haatvedt, N., Sørenes, N., & Thorbjørnsen, T. (2002). Crustal structure of the southern part of the Vøring Basin, mid-Norway margin, from wide-angle seismic and gravity data. Tectonophysics, 355(1-4), 99-126.

Rawlinson, N., Pozgay, S., & Fishwick, S. (2010). Seismic tomography: a window into deep Earth. Physics of the Earth and Planetary Interiors, 178(3-4), 101-135.

Riber, L., Dypvik, H., &Sørlie, R. (2015). Altered basement rocks on the Utsira High and its surroundings, Norwegian North Sea. Norwegian Journal of Geology, Norwegian Journal of Geology, 2015-08-20.

Roberts, D., & FitzPatrick, J. (2015, September). Planning and Operating a Transition and Land 2-D Seismic Survey Using a Combination of Integrated Source and Recording Equipment in a Remote Location, Lake Tanganyika—The East African Rift Valley. In International Conference and Exhibition, Melbourne, Australia 13-16 September 2015 (pp. 225-225). Society of Exploration Geophysicists and American Association of Petroleum Geologists.

Robinson, E. A., & Clark, D. (2017). Basic geophysics. Society of Exploration Geophysicists.

Ruiz, M., Díaz, J., Pedreira, D., Gallart, J., & Pulgar, J. A. (2017). Crustal structure of the North Iberian continental margin from seismic refraction/wide-angle reflection profiles. Tectonophysics, 717, 65-82.

Sayers, C., & Chopra, S. (2009). Introduction to this special section: Seismic modelling. The Leading Edge., 28(5), 528-529.

Sheriff, R. E., & Geldart, L. P. (1995). *Exploration seismology*. Cambridge university press.

Shulgin, A., Mjelde, R., Faleide, J., Høy, T., Flueh, E., & Thybo, H. (2018). The crustal structure in the transition zone between the western and eastern Barents Sea. Geophysical Journal International, 214(1), 315-330.

Stucchi, E., Mazzotti, A., & Baudo, S. (2003, June). High Resolution Seismic in the Area of the Great Ancona Landslide–Processing Results. In 65th EAGE Conference & Exhibition (pp. cp-6). European Association of Geoscientists & Engineers.

Sturt, B.A., Dalland, A. and Mitchell, J.L. (1979) The age of the sub Mid-Jurassic tropical weathering profile of Andøya, Northern Norway, and the implications for the Late Palaeozoic palaeogeography in the North Atlantic region. Geologische Rundshau, 68, 523–542.

Thirunavukarasu, A., Kumar, A., & Mitra, S. (2016). Lateral variation of seismic attenuation in Sikkim Himalaya. Geophysical Supplements to the Monthly Notices of the Royal Astronomical Society, 208(1), 257-268.

Vagiona, D. G., &Kamilakis, M. (2018). Sustainable site selection for offshore wind farms in the south Aegean—Greece. Sustainability, 10(3), 749. doi:http://dx.doi.org/10.3390/su10030749

Van Avendonk, H., Harding, A., Orcutt, J., & Holbrook, W. (2001). Hybrid shortest path and ray bending method for traveltime and raypath calculations. Geophysics: The Journal of the Society of Exploration Geophysicists, 66(2), 648-653.

Virieux, J. (1986). P-SV wave propagation in heterogeneous media: Velocity-stress finite-difference method. Geophysics : The Journal of the Society of Exploration Geophysicists, 51(4), 889-901.

Vogt. (1905). V. Om Andøens jurafelt, navnlig om landets langsomme nedsynken under juratiden og den senere hævning samt gravforkastning.

White, R.S. (2012). Chapter 11 - Wide-angle refraction and reflection. In: Roberts, D.G. and Bally, A.W., eds., Regional Geology & Tectonics: Principles of Geologic Analysis. Elsevier., pp. 310–328.

Wyman, L., & Ahmad, K. (2013). Transition Zone Seismic Acquisition on the Alaska North Slope, Simpson Lagoon. In SPE Arctic and Extreme Environments Technical Conference and Exhibition. OnePetro.

Yilmaz, O. (1987). Seismic data processing: Investigations in geophysics. Society of Exploration Geophysicists, 2, 526.

Yilmaz, O. (2001). Seismic data analysis: Processing, inversion, and interpretation of seismic data. Society of exploration geophysicists.

Zelt, C.A. (2011). Traveltime tomography using controlled-source seismic sata. In: Gupta, H.K. (eds) Encyclopedia of Solid Earth Geophysics. Encyclopedia of Earth Sciences Series. Springer, Dordrecht. https://doi.org/10.1007/978-90-481-8702-7_56

Zhou, H. W. (2014). Practical seismic data analysis. Cambridge University Press.

Zoeppritz, K. (1919). On the reflection and propagation of seismic waves. *Gottinger Nachrichten, 1*(5), 66-84.

Zwaan, B., Fareth, E. and Grogan, P.W. (1998) Trømsø, bedrock geological map, scale 1:250.000, Norges geologiske undersøkelse.

Appendix A

Comparisons between the TZ seismic data (middle) and modelled synthetics, model M3 (left) and model M2 (right) for nearest and farthest receivers (CRG1 and CRG120, respectively).

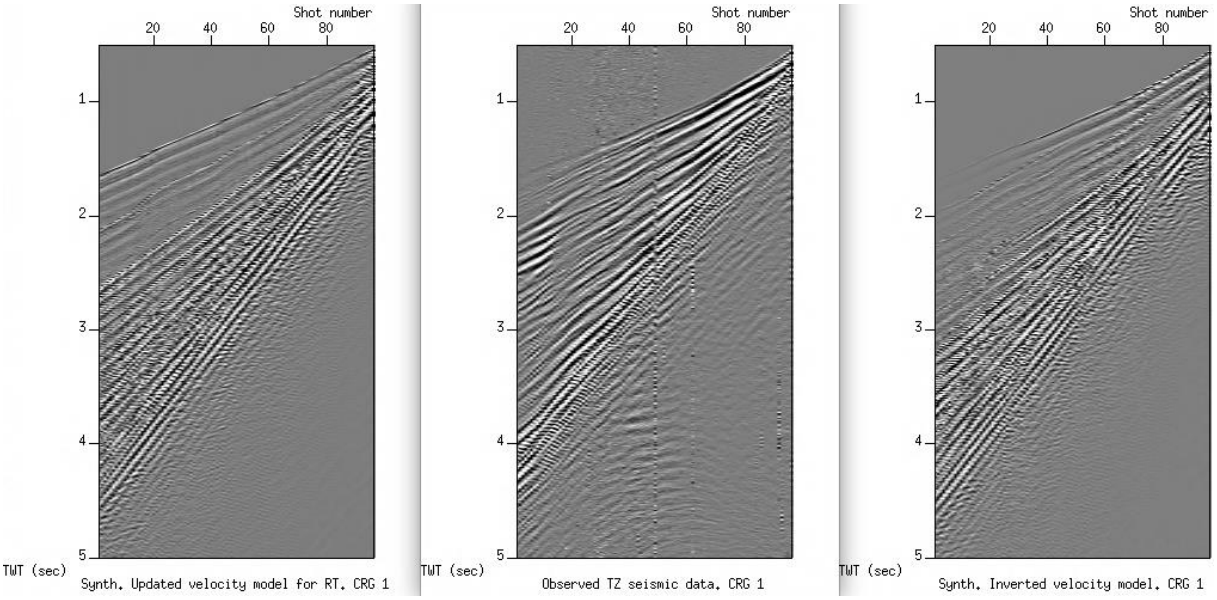

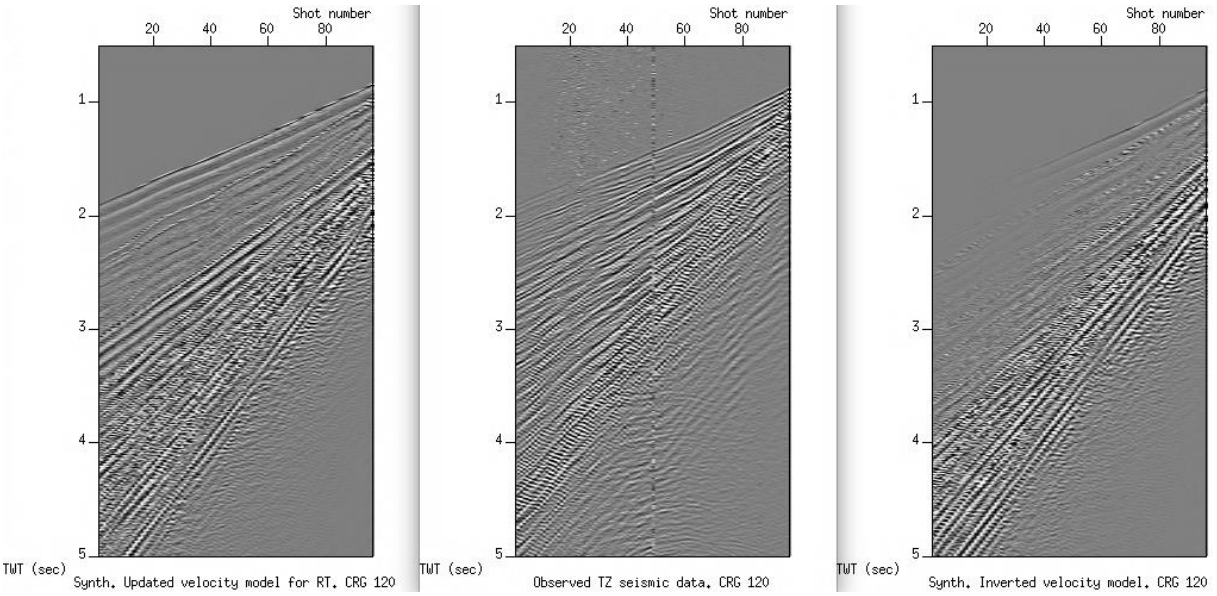

Appendix B

From top to bottom: Reflection coverage for base Quaternary, base Aptian, base Barremian, and BCU.